THE UNIVERSITY OF
SYDNEY

COPYRIGHT AND USE OF THIS THESIS

This thesis must be used in accordance with the provisions of the Copyright Act 1968.

Reproduction of material protected by copyright may be an infringement of copyright and copyright owners may be entitled to take legal action against persons who infringe their copyright.

Section 51 (2) of the Copyright Act permits an authorized officer of a university library or archives to provide a copy (by communication or otherwise) of an unpublished thesis kept in the library or archives, to a person who satisfies the authorized officer that he or she requires the reproduction for the purposes of research or study.

The Copyright Act grants the creator of a work a number of moral rights, specifically the right of attribution, the right against false attribution and the right of integrity.

You may infringe the author's moral rights if you:

- fail to acknowledge the author of this thesis if you quote sections from the work
- attribute this thesis to another author
- subject this thesis to derogatory treatment which may prejudice the author's reputation

For further information contact the University's Director of Copyright Services

sydney.edu.au/copyright

Numerical Modelling of Particle Transport in Reservoirs Due to Diurnal Temperature Variations

By

Shengyang CHEN

A thesis submitted in fulfilment of the
requirements for the degree of

Master of Philosophy

THE UNIVERSITY OF
SYDNEY

Faculty of Engineering and Information Technologies

The University of Sydney

2014

Acknowledgements

To begin with, I would like to express my deep thanks to my supervisors A/Prof Chengwang Lei, and Prof John C. Patterson for their supervision, encouragement, and guidance throughout my MPhil study. Their insightful knowledge and attentive attitude in research inspired me, and their critical comments and advice pushed me to improve my research skills. Furthermore the academic responsibility that they encouraged serves as a fine example for my future work.

My thanks also go to our group members Dr Yang Liu, Mr Yongling Zhao, and Mr Rakesh Khanal. Their assistance in getting me to familiarise myself with the research methodology and knowledge is greatly appreciated. I am particularly grateful to Dr Yang Liu and Mr Yongling Zhao. Dr Yang Liu shared much of his own research experience with me when I needed help, encouraged me when I met difficulties, and provided me with technical support while I was learning how to use the research tools. Mr Yongling Zhao also shared with me both his deep understanding of research topics in relevant fields and his perspective on problems in both his and my projects.

It is also my pleasure to thank Mr Michael Homsey, who helped me with software installation and maintained the computing clusters.

I would also like to express my deepest appreciation to all the staff in the School of Civil Engineering for creating a thoroughly comfortable place for me and others to conduct research. I am also grateful for the friendly atmosphere provided by all my office colleagues in Rooms 101 and 360 of the Civil Engineering Building.

The thoughtful editorial comments and the detailed corrections to my manuscripts and the current thesis given by my supervisors, which have helped to substantially improve the quality of these documents, are greatly appreciated.

The financial support provided by my supervisors is also gratefully acknowledged.

Last but not least, my deep thanks to my parents for their unconditional spiritual and financial support and understanding. Although they live far away from the place of my study, their spiritual support has accompanied me and enlightened me.

Abstract

This thesis is concerned with particle transport in a reservoir model subject to periodic thermal forcing at the water surface. A commercial Computational Fluid Dynamics (CFD) code coupled with a Discrete Phase Model (DPM) is adopted to examine particle motions under various conditions. The following investigations have been carried out:

Firstly, a previously reported concurrent Particle Image Thermometry and Particle Image Velocimetry (PIT/PIV) experiment has been numerically reproduced. Both qualitative and quantitative agreements in terms of temperature and velocity structures, horizontal volumetric flow rate, and the time lag of the flow response to the switch of the thermal forcing are achieved between the present numerical simulation and the experiment. A parametric study has also been carried out using the validated numerical model to determine the dependence of the flow response and its stability properties on the Grashof number. It is found that the Grashof number plays an important role in determining the onset time for the instability, the time duration of the unstable phase, and the time lag of the flow response to the switch of the thermal forcing.

Secondly, the numerical model is adopted to investigate particle dispersion in the reservoir in a pseudo real-life scenario in which pollutant or nutrient particles are injected from the sidearm of the reservoir. The dispersion and deposition rates and the concentration of the particles in various regions of the water body are examined. The study has confirmed the important transport mechanism associated with natural convection which contributes to the pollutant/nutrient deposition and dispersion in reservoirs. A case study based on a recent event of algal bloom with potentially severe effects on the water quality in Lake Burragorang near Sydney has been discussed.

Finally, the numerical model has been extended to include particle collision and augmentation, and a preliminary study has been carried out to examine the effect of particle collision on the transport of particles in the water body. Numerical results are presented in terms of the spectrum of particle sizes; and the dispersion and deposition behaviours. The results obtained with the inclusion of a particle collision model are compared with those obtained using a non-colliding particle model. It is revealed that, whilst the particle collision model may have a significant effect on the particle size distribution, depending on the initial particle concentration, its impact on the particle mass distribution is insignificant.

Table of Contents

List of Figures

List of Tables

List of Publications

- S. Chen, C. Lei, and J.C. Patterson, *Numerical modelling of a concurrent PIT/PIV experiment with TLC particles in a reservoir model subject to periodic thermal forcing,* Numerical Heat Transfer, Part A: Applications, 2013, *in press.*

- S. Chen, C. Lei, and J.C. Patterson, *Transport of pollutant particles in a reservoir due to diurnal temperature variation,* International Communications in Heat and Mass Transfer, 2013, *under review*.

Nomenclature

A	aspect ratio of the entire computational domain
b_c	critical impact parameter of particles
C_d, C_c	drag coefficient and Cunningham factor
C_{pt}, C_0	instantaneous and initial particle concentrations
$\bar{C}_{rel}$	relative velocity between fluid and particle
d_p	particle diameter
E_{coal}	coalescence efficiency
E_{trans}	translational energy
d_{ij}, d_{lk}, d_{kl}	deformation/strain tensors
$D_{T,p}$	coefficient of thermophoresis
F_a	additional minor forces acting on particles
F_D, F_g	drag force and gravitational force of particles
F_T, $\vec{F}$, F_b	thermophoresis force, lift force, and Brownian motion force
g	acceleration due to gravity
Gr	Grashof number
H	maximum water depth
k	wavenumber
$k_{f'}$	adjusted fluid thermal conductivity
k_p	particle thermal conductivity
K_B	Boltzmann constant

Kn	Knudsen number
L	total length of the computational domain
L_1	length of the region with a uniform depth
m_p	mass of particles
p	pressure
P	thermal forcing period
Pr	Prandtl number
q_H	instantaneous horizontal particle flux
Q_H, Q_V	horizontal and vertical exchange flow rates
r_1, r_2	radii of particles
$Rand$	random number
Re	Reynolds number
S	inclination of a sloped bottom
S_0	adjusted Gaussian white noise intensity
t	time
Δt	time-step size in numerical simulation
t_{all}, t_{tip}	mean residence time for particles in the entire domain and in the tip region
t_b, t_{dt}, t_{lag}	onset time of the instability, time duration of unstable phases, and time lag
t_f	thermal diffusion time of fluid
T, T_0	instantaneous and starting (reference) water temperatures
ΔT	maximum temperature variation
u_f, $\bar{u}_f$	instantaneous fluid velocities and average velocities of fluid molecules
u_p, u_{px}	instantaneous particle velocities and horizontal velocities of particles
u_x, u_y	horizontal and vertical components of the flow velocity
V_{cell}	volume of the numerical cell

We	Weber number
x, y	horizontal and vertical coordinates originating from the tip

Greek symbols

β	coefficient of thermal expansion
η_0	initial particle fraction
κ	thermal diffusivity
μ	dynamic viscosity
ν	kinematic viscosity
π	the ratio of a circle's circumference
ρ_0	fluid density at the reference temperature
ρ_p	particle density
σ	particle surface tension
τ, τ_1	particle relaxation time and adjusted particle relaxation time
ψ	mean free path of the fluid
φ	mean residence time

Superscript

*	normalised parameters

1. Introduction

1.1 Problem description

The inflow into reservoirs from sidearms may contain nutrient and/or pollutant particles, which are dispersed across water bodies by various transport and mixing processes including those driven by natural convection. According to the Australian Drinking Water Guidelines (ADWG, 2004), a precautionary strategy should be developed against variation of the water quality in reservoirs. To achieve this goal, understanding the particle transport in reservoirs is critical as it is directly relevant to the water quality in these water bodies. Accordingly, the understanding of the unsteady natural convection as one of the important transport mechanisms which drives particle motion in reservoirs is of great interest. This research involves an investigation of two major themes: natural convection and particle transport in reservoirs.

Natural convection in reservoirs is induced by the ambient thermal forcing including air temperature variation and solar radiation. The problem of natural convection in reservoir models has been studied extensively by many authors (e.g. Monismith et al. [1], Farrow and Patterson [2], Lei and Patterson [3, 4], Bednarz et al. [5, 6], and Mao et al. [7]). The effect of heating at the water surface may cause stratification of the whole water body, resulting in the establishment of two distinct layers – hypolimnion and epilimnion; whereas the effect of the surface cooling, which may cause a Rayleigh-Bernard type instability, is the main driving mechanism for the formation of plunging plumes within the water body [6]. The processes outlined above, which will be investigated in more detail in this thesis, can provide one of the most important driving mechanisms for contaminant dispersion in the water body in addition to other mechanisms such as wind forcing at the water surface, influent of reservoirs, or evaporation. In addition to the effect of thermal forcing, the geometry of reservoirs may also affect the flow in the natural water body. Of particular interest here is the geometry consisting of two distinct regions with a sloped bottom and a flat bottom respectively [2].

Particle transport in reservoirs involves several fluid dynamical processes. As mentioned above, an important process of interest is natural convection, manifesting as circulations between the littoral regions and central regions of reservoirs due to either heating or cooling, and their interaction with the particular geometry. This is the mechanism responsible for mixing substances of interest (e.g. pollutant/nutrient particles) between the epilimnion and hypolimnion in natural water bodies. Particle transport in fluids has been reported and discussed in many studies, such as the environmental perspective to understand contaminant dispersion in either air flows or water flows [8, 9], and coastal engineering to comprehend the sediment transport (e.g. scouring) [10]. It is reported in the literature (e.g. [11, 12]) that the numerical simulation of particle transport can accurately predict particle motion in fluids. Accordingly, CFD (Computation Fluid Dynamics) modelling of particle transport in reservoir models under natural convection is carried out in the present project. The purpose of this research is to develop deep insights into how pollutant particles are transported in natural water bodies under the effect of natural thermal forcing. This has implication for the occurrence of environmental hazards in certain circumstances.

The methodology of modelling dispersed particle transport in fluids can be generally classified into two different approaches – the Eulerian-Eulerian approach and the Eulerian-Lagrangian approach. These are both based on CFD codes. The fluid flows are solved using the Eulerian method, whereas particle motion can be solved by either the Eulerian or Lagrangian method. The coupling of the fluid flow and particle motion is essential to the numerical model. The motion of particles strongly depends on the result of the calculation from the continuum phase (i.e. the fluid flow). In one-way coupling of the two phases, particle motion has no influence on the fluid flow, whereas two-way coupling of the two phases also accounts for the effect of particle motion on the fluid flow.

1.2 Literature review

1.2.1 Unsteady natural convection in reservoirs

Natural convection is a heat transport mechanism that is driven by buoyancy, in which fluid flows are determined by the variation of density usually caused by temperature or concentration gradients. In general, the heated part of a fluid body is less dense and tends to travel up to the surface in the opposite direction of gravity; whereas the cooler part is denser and tends to flow downwards. As a consequence, a convective circulation forms. In the case of reservoirs, natural convection plays a significant role in promoting mixing and exchange across the water bodies, especially under relatively calm conditions (i.e. when the wind stress is weak). For instance, both the bottom heating associated with the residual solar radiation reaching the bottom and the surface cooling due to heat loss to the atmosphere may result in a Rayleigh-Bernard type instability, thereby promoting strong vertical mixing in the local water column.

The early research of natural convection in reservoirs was initially established by modelling the processes in a square enclosure. The square enclosure model can indicate the flow behaviour in the region of reservoirs having a uniform water depth. However, they have limitations in representing the flow patterns in real-life situations. Therefore, a reservoir model depicted by a triangular domain has been adopted in later research. In such a triangular model, a gently sloping bottom is included in the model to consider the changing water depth in field situations. This may result in a more complex flow structure. The triangular model has been adopted in [2-4, 13] to investigate the flow in the sidearm of reservoirs. Subsequently, a more realistic model has been established which includes a region with a sloped bottom adjacent to another region with a uniform depth [5, 6, 14, 15]. The sloped bottom emerges as an unstable factor for the large-scale convective circulations because of the establishment of temperature gradients along the sloped bottom. Many studies have demonstrated that the sloped bottom plays an important role in horizontal convection within the domain (e.g. [4, 13]).

In the literature, the exchange and mixing in reservoirs under different thermal forcing conditions has been investigated experimentally, numerically and analytically [3-6, 15, 16]. For numerical and analytical modelling, mainly laminar natural convection models have been developed and implemented. Similarly, the present project adopts a laminar natural convection model.

The effect of different thermal forcing on flow patterns

The convective flow in reservoirs induced by the effect of diurnal heating and cooling is important for the transport of particulate matters across the reservoirs. In a typical diurnal cycle, the thermal conditions of interest involve daytime heating and night-time cooling. These types of thermal forcing may result in complex flow patterns in the reservoirs. The resultant flows may include large-scale circulations across the entire water bodies (i.e. the primary circulations) superimposed by small-scale local convective circulations (i.e. the secondary circulations), causing the transport of substances such as pollutants and nutrients across the natural water bodies.

The studies of the daytime heating process have been carried out extensively (e.g. [3, 17, 18]). In the reservoir model, the daytime unequal capture of radiation as the result of changing water depth is a significant mechanism for particle exchange and mixing in reservoirs. The absorption of solar radiation entering through the water surface results in relatively warm shallow regions and a stable stratification in deep regions. In shallow waters, the average temperature increases with decreasing depth along the slope, resulting in a horizontal temperature gradient. The lateral temperature gradient in the shallow region in turn drives a convective flow up along the slope and out of the tip region along the surface. In addition, if the water depth is less than the penetration depth of solar radiation (this is the case for at least part of the shallow region with a sloped bottom), a fraction of the radiation reaches the bottom, which will be absorbed by the bottom and the absorbed energy is then re-emitted as a heat flux from the bottom. The bottom heating will result in a Rayleigh-Benard type instability, and thus a secondary convection will form in the local water column. These large and small-scale convective flows act together to form complex flow structures in the reservoir. It is worth noting that the sloped bottom in this case provides a driving mechanism for the large-scale convective flow.

The above-described radiation heating process has been investigated experimentally, numerically, and analytically by many researchers such as Lei et al. [3, 4, 13, 17, 19], Monismith et al. [1], and Mao et al. [18]. Among the experimental investigations, the study reported in [17] used the shadowgraph technique to visualise the development of the flow in the sidearm. The solar radiation in the experiment [17] was simulated by a theatre spot lamp. The results clearly indicated simultaneous growth of thermal boundary layers from both the top and bottom of the water body. The instability associated with the bottom heating mechanism was observed in the subsequent development of the flow. This experiment provided, for the first time, a physical evidence of radiation heating at the bottom causing the vertical mixing within the water body of the reservoir. In addition to the experimental study, the numerical studies were also reported extensively (e.g. [3, 4, 19]). The setup of these numerical models was mainly based on the experimental model of [17]. The numerical study of this process emphasized the bottom heating effect since it was the positive heat flux from the bottom that initiated the plumes in local water columns [3].

The numerical model was slightly simplified by considering a constant flux thermal forcing condition along the sloped bottom. A direct stability analysis was also carried out based on the same numerical reservoir model (e.g. [19]). Several dimensionless parameters including the Prandtl number, the Grashof or Rayleigh number, and the aspect ratio of the geometry were identified as the control parameters characterising the flow behaviour in various flow regimes.

The night-time cooling effects have also been investigated extensively (e.g. [5, 7, 20]). Cooling can be specified as a surface heat loss, such as a constant heat flux out of the surface (iso-flux) or a constant surface temperature (isothermal) that is lower than the water body temperature. To a certain extent the cooling process is similar to the daytime radiation heating, in which the shallow region with a sloping bottom plays an important role. Because of the unequal cooling rate due to the depth variation in the shallow region, a horizontal temperature gradient is developed in a form similar to the situation discussed for the heating process. The result of this cooling is a cold water undercurrent proceeding toward the deeper region along the slope. In the meantime, cooling at the water surface results in a vertically adverse temperature gradient, which may cause the Rayleigh-Benard type instability in the form of plunging plumes issuing from the thermal boundary layer underneath the surface.

The surface cooling process was also investigated using various methods including experiments, simulations, and analyses [5, 7, 15, 20]. One experimental study was carried out by Bednarz et al. [5] using the Particle Image Thermometry (PIT) technique. Their experiment adopted a reservoir model consisting of a region with a sloped bottom and another adjacent region with a uniform depth, and used thermo-chromic liquid crystals (TLCs) as tracers in fluids. The fluid temperature was measured from the colour of the TLC particles through calibration. Their experiment confirmed the general behaviour of the flow development during the night time cooling phase. The overall flow development was classified into three stages – namely initial growth, transitional, and quasi-steady stages. However, the limitation of the experiment reported in [5] is worth noting. On one hand, the temperature in the experiment was constrained in a very small range by the property of the TLCs. On the other hand, a rigid wall was placed at the water surface in order to achieve surface cooling. A corresponding numerical study of the flow in the same model was also conducted by the same authors in [15]. This study considered the cooling effect at the free surface of the water body. A constant heat flux going out of the surface was specified with a small perturbation. Their simulation clearly showed the instability of the flow development from the initial stage to the transitional one. The numerical results were validated against a previous scaling analysis. The scaling analysis of the cooling process by Mao et al. [7] has quantified the flow properties in various regions from nearshore to offshore. Three distinct flow regimes – referred to as conductive regime, stable convective regime, and unstable convective regime, along the sloped bottom were identified and discussed in detail. These three regimes are determined by the global Rayleigh number, a critical Rayleigh number for the Rayleigh-Benard type instability, and the slope of the bottom. The scaling relationships derived in [7] were validated against corresponding simulations.

The diurnal thermal cycle includes both the heating and cooling processes described above, and a much more complicated flow is expected over the diurnal cycle as a result of the switch of the thermal forcing between heating and cooling. The diurnal process has also been investigated by many researchers (e.g. [1, 2, 6, 14, 16]). Among these investigations, Bednarz et al. [6] carried out a concurrent PIT and PIV (Particle Image Velocimetry) experiment; Lei and Patterson [14] performed a numerical simulation with a periodic isoflux condition at the surface; and Bednarz et al. [16] studied numerically the diurnal flow response to a periodic temperature variation at the surface. All these studies have revealed that a distinct flow instability occurs during the cooling phase under periodic thermal forcing regardless of the type of thermal forcing (i.e. isoflux, isothermal, or radiation heating). In addition to the thermal forcing specified at the water surface, the study reported in [14] has also considered the re-emission of heat from the residual radiation absorbed by the bottom during radiation heating and has showed that instability also occurs during the heating phase because of an adverse temperature gradient in the bottom layer. Most of the studies of the flow response to diurnal thermal forcing [1, 2, 6, 14, 16] have consistently confirmed a time lag in the overall flow response to the switch of the thermal forcing. Despite all these studies have shown a similar flow behaviour, no direct comparison has been made among them.

1.2.2 Particle transport in fluid flows

1.2.2.1 Particle transport theory

Particle motion in fluids is governed by the following momentum equation [12] (based on unit mass).

$$\frac{du_P}{dt} = \frac{u_f - u_p}{\tau} + \left(1 - \frac{\rho_0}{\rho_p}\right) g + F_a \tag{1}$$

The particle motion is driven by three groups of forces, which are respectively represented by the three terms on the right-hand side of Equation (1): the first term is the drag force; and the second term is the gravitational forces including buoyancy force emanating from the fluid. The last term consists of all additional minor forces that may need to be considered, including the thermophoretic force, lift force, and etc.

The most common forces involved in the theory of particle dynamics will be discussed individually below.

$Drag\ force$

The drag force always presents whenever there is a relative motion between the particle and the fluid, provided that the particles are not chemically reactive with the fluid. This is a resistant force, which enables the particle to catch up with the changing velocities of the surrounding fluid [11]. Therefore, it is determined by the relative velocity between the local flow velocity u_f and the particle velocity u_p. The general expression of the drag force per unit mass of particles is given by:

$$F_D = \frac{u_f - u_p}{\tau_1} \tag{2}$$

The denominator τ_1 in equation (2) is corrected from the particle relaxation time τ in Stokes drag regime (see below), where τ is given by:

$$\tau = \rho_p d_p^2 / 18\mu \tag{3}$$

The relaxation time describes the time required for a particle to reach a state with a terminal velocity in a vertical glass tube experiment due to its gravitational force, in which both the fluid and particle are initially stationary. It also represents the characteristic response time of the particle when it is surrounded by moving fluids.

However, it is necessary to correct this relaxation time to account for the slip velocity and rarefied gas effect. This has been done by incorporating a drag coefficient C_d and the Reynolds number as well as the Cunningham factor C_C that characterises the rarefied gas effect. The corrected particle relaxation time is given by:

$$\tau_1 = \tau \frac{2}{ReC_d} C_c \tag{4}$$

where the Cunningham factor C_C is given by,

$$C_C = 1 + Kn(a + be^{\frac{-c}{Kn}}) \tag{5}$$

where a, b, and c are given the constant values of 2.51, 0.80, and 0.55 respectively in [21]; Kn is the Knudsen number determined by the particle diameter and the mean free path of the fluid: $Kn = 2\psi/d_p$; ψ is a mean free path of the fluid given by the ratio of the kinematic viscosity ν to the average velocity of the fluid molecules $\bar{u}_f$ in the domain as follows [22]:

$$\psi = 2\nu/\bar{u}_f \tag{6}$$

In equation (4), C_c is equal to 1 when the fluid is liquid instead of gas phase; Re is the slip Reynolds number (dimensionless), which is defined as:

$$Re = d_p|u_f - u_p|/\nu \tag{7}$$

The drag coefficient C_d is a function of Re, which is given by Morsi & Alexander [23] as

$$C_d = a_1 + a_2/Re + a_3/Re^2 \tag{8}$$

where a_1, a_2, a_3 are constants and can be found in Table 1. This correlation of drag coefficient is generally valid for particles of spherical shape.

Table 1 Drag coefficient parameters summary according to Reynolds number [23]

Reynolds number	a_1	a_2	a_3
Re<0.1	0	24	0
0.1<Re<1.0	3.69	22.73	0.0903
1.0<Re<10.0	1.222	29.1667	-3.8889
10.0<Re<100.0	0.6167	46.5	-116.67
100.0<Re<1000.0	0.3644	98.33	-2778
1000.0<Re<5000.0	0.357	148.62	-4.75×10^4
5000.0<Re<1.0×10^4	0.46	-490.546	57.87×10^4
1.0×10^4<Re<5.0×10^4	0.5191	-1662.5	5.4167

The drag force is one of the most important driving forces in particle transport, and thus is included in every particle transport model. In the present project we assume that particles are of spherical shape and thus the above correlation for drag coefficient is adopted.

Gravitational force

The gravitational field is always present in natural water bodies. As an important driving force for natural convection, the gravitational force also plays an important role in particle motion. When submerged in a fluid, a particle experiences gravity and a buoyancy force. The gravity drives the particle downwards to settle, whereas the buoyancy force tends to lift the particle up to the surface of the fluid. The combined effect of the gravity and buoyancy on the particle is quantified by (per unit mass):

$$F_g = \left(1 - \frac{\rho_0}{\rho_p}\right) g \tag{9}$$

If the density of the particle is higher than that of the fluid, it will result in a settling acceleration, which in turn influences the overall motion of the particle.

Thermophoretic force

A particle suspended in a gas field with a temperature gradient will experience a temperature gradient induced force in the direction that is opposite to the direction of the temperature gradient. This is the so-called thermophoretic force. The thermophoretic force is only emanated in the case when particles travel in the gas having a temperature gradient. Although the thermophoretic force is not relevant when particles are surrounded by liquids, it is still worth addressing here as it is a common force for particle transport in fluids. The thermophoretic force can be expressed as (presented in force per unit mass):

$$F_T = -D_{T,p} \frac{1}{m_p T} \frac{\partial T}{\partial x} \tag{10}$$

In the above equation, m_p is the mass of the particle; the coefficient of thermophoresis $D_{T,p}$ (in Nm) can be determined either as a constant, or a polynomial of the properties of the fluid and particle, or in other functional forms. However, one of the most widely adopted ones is the equation given by Talbot et al [24]:

$$D_{T,p} = \frac{6\pi d_p \mu^2 C_s (K + C_t Kn)}{\rho_0 (1 + 3C_m Kn)(1 + 2K + 2C_t Kn)} \tag{11}$$

where Kn is the Knudsen number defined in Equation (6); the parameter K can be determined by the adjusted fluid thermal conductivity over the particle thermal conductivity $K = \frac{k_{f'}}{k_p}$. The adjusted fluid thermal conductivity is only based on translational energy given as $k_{f'} = (\frac{15}{4})\mu E_{trans}$, where the translational energy is given by $E_{trans} = \frac{1}{2} m_p u_p{}^2$. $C_s, C_t,$ and C_m are three constants with values of 1.17, 2.18 and 1.14 respectively.

Lift force

The lift force is discussed in [11] and it may also have an influence on the particle's motion. The lift force is perpendicular to the flow direction. The effect of this force can be seen in the free body diagram below (Figure 1).

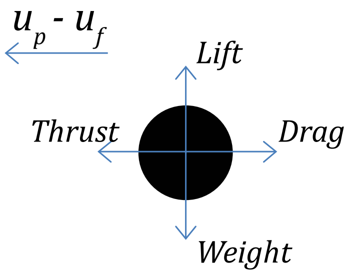

Figure 1 The important forces of particle motion.

In the diagram above, the thrust is a reaction force that expels or accelerates mass in one direction, which requires an external or internal power to drive the particle, and thus is not relevant for the motion of the inert type of particles considered in this project.

The lift force for particles in fluids is associated with the particle's Reynolds number. The lift force induced by shear in the flow field that was introduced by Saffman [25] will be considered in this model. It is also known as Saffman's lift force. Li and Ahmadi [26] have provided the following generalised equation of the lift force due to shear:

$$\vec{F} = \frac{2\zeta \nu^{\frac{1}{2}} \rho d_{ij}}{\rho_p d_p (d_{lk} d_{kl})^{\frac{1}{4}}} (\vec{u}_f - \vec{u}_p) \tag{12}$$

In the equation above, ζ is a constant (=2.594). The deformation tensors or strain tensors (d_{ij}, d_{lk}, and d_{kl}) can be obtained from $d_{ij} = \frac{1}{2}(\frac{\delta u_{fi}}{\delta x_j} + \frac{\delta u_{fj}}{\delta x_i})$, where the subscripts are the different directions of the tensors. The shear induced lift force is significant for submicron particles, and it may enhance settling velocity of the particle.

Brownian dispersion

The effect of Brownian dispersion motion can be generally applied to submicron particles as well. The Brownian motion may be observed in a real-life scenario, in which small particles appear to drift randomly in fluids. As a result, the Brownian motion in the numerical model is often calculated based on a probabilistic distribution. One of the applicable approaches to resolving the Brownian motion of particles is the application of the Gaussian white noise process which was proposed by Li and Ahmadi [26]. The equation of particle Brownian motion and its trajectory can be evaluated by solving Newton's second law of motion. The force of the Brownian motion is given by:

$$F_{b_i} = Rand_i \sqrt{\frac{\pi S_0}{\Delta t}} \tag{13}$$

In this equation, the random number $Rand_i$ has a zero-mean property, and is based on Gaussian random numbers; the subscript i represents the pointer to the individual particle; Δt stands for the time-step size in each calculation; S_0 is derived from the Gaussian white noise process with the spectral intensity discussed in [26]. The expression of S_0 is given as follows:

$$S_0 = \frac{C_e \nu K_B T}{\pi^2 \rho_0 d_p^5 ({}^{\rho_p}/_{\rho_0})^2 C_c} \tag{14}$$

where C_e is an empirical constant $(= 216)$ and the Cunningham factor C_c is given in Equation (5). The Boltzmann constant K_B is equal to$1.38 \times 10^{-23}\, J/K$.

As shown in the above equations, the Brownian force is evaluated based on the time step and the temperature. The energy equation must be solved in order to evaluate the Brownian force on particles. The validation of the model was also demonstrated by Li and Ahmadi [26].

Particle collision models

Collision of particles may have an additional impact on particle transport. A particle collision model is needed to resolve particle collision in numerical models. The particle collision model usually provides a stochastic estimation of particle collision in a continuous-phase. In the literature [27], one of the most commonly adopted algorithms for the collision model is based on probabilistic analysis of particle collision, which is adopted to reduce computational cost. Two efficiencies – the collision efficiency and the coalescence efficiency are adopted to describe particle collision. The collision efficiency is directly derived from the probability model, which is explained below. Two particles that may be involved in collision form a collision pair. It is worth noting that particles with the same velocities will not collide with each other so that the concept of 'parcel of particles' is adopted to simulate a group of particles with the same velocity in order to avoid them from colliding in the probability model. Furthermore, the concept of 'collision volume' is introduced here. The collision volume is determined by the particle diameters, time-step

(Δt) of the transient calculation, and the relative velocity ($\bar{C}_{rel}$) of the collision pair, as shown in Figure 2. It is the space that a particle will cover relative to the other particle of the collision pair within one time-step (Δt) and is given by $\pi(r_1+r_2)^2\bar{C}_{rel}\Delta t$. The collision efficiency is then calculated as the ratio of the collision volume to the volume of the numerical cell (V_{cell}), i.e. $\pi(r_1+r_2)^2\bar{C}_{rel}\Delta t/V_{cell}$, where the volume of numerical cell here is the area of the computational grid element in which the collision pair is located.

Following the collision, there is a probability of coalescence for the particle pair, which is measured by the coalescence efficiency E_{coal} [27]. The coalescence efficiency is mainly dependent on the pair's radii (r_1, r_2), the collisional Weber number (We) that is relevant to the relative velocity of the pair, i.e. $We=\rho_p\bar{C}_{rel}^{\ 2}d_p/\sigma$, and collision impact parameter b. The coalescence efficiency can be derived following the principle described below (see [27] for more details): If the rotational energy of the two colliding particles is smaller than the energy required to reform the surface of a coalesced pair of particles (deformation energy), the two particles will coalesce. In contrast, if the rotational energy of the colliding particles is bigger than the deformation energy, the two particles will be grazing and fly apart. The coalescence efficiency E_{coal} is associated with the two above-mentioned energy equations (rotational energy vs. deformation energy). Equating the two energy terms will result in an equation to determine the critical value of the impact parameter (b_c), which has a maximum 1 and a minimum 0. The coalescence efficiency E_{coal} is determined by the probability having $b \le b_c$. Agreements between the above-described particle collision model and the experiments [28] are achieved [27].

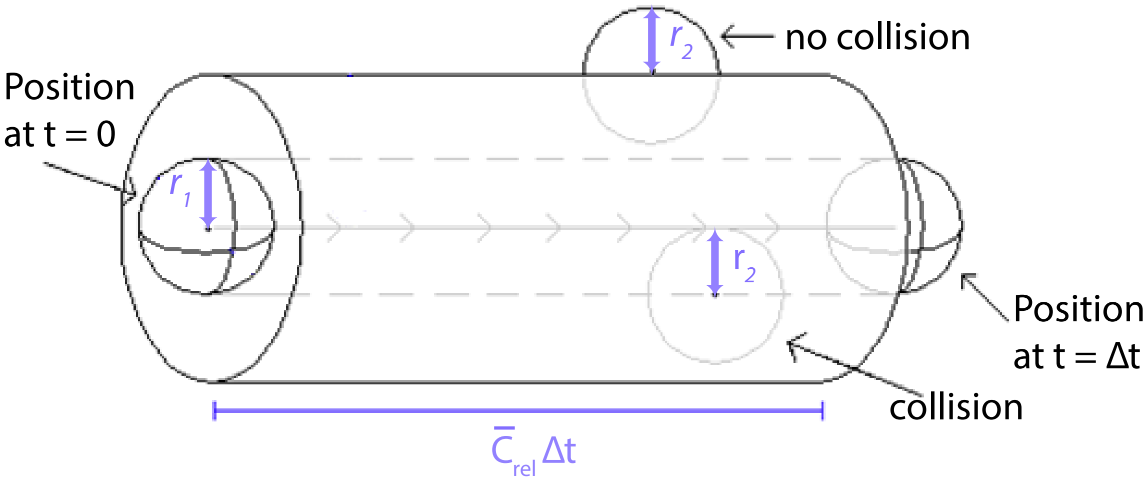

Figure 2 The collision volume (modified based on [29]).

The limitations of the above-described particle collision model have a direct impact on the accuracy of the numerical results. Firstly, two particles may collide only if they are within the same grid element. This assumption curbs particles that are located very close to each other but not in the same grid cell from colliding while allowing particles that are far away from each other but within the same grid cell to collide. Secondly, because of the above assumption, the collision model is very sensitive to the grid resolution. However, this can be overcome by using a properly refined mesh and having more particles injected into the domain.

To further improve O'Rourke's collision model, Li et al [30] have extensively investigated the O'Rourke's algorithm and proposed a new model based on smoothed particle hydrodynamics. Their study mainly focuses on refining the existing collision model and comparing the data between the refined and existing models. The new model which they proposed, to a certain extent, has overcome the limitation of O'Rourke's collision model by improving the algorithm to locate the collision pairs.

1.2.2.2 Numerical approaches for particle tracking

As mentioned above, particle transport models can be applied to investigate the pollutant dispersion in natural water bodies. Although the investigation in the present project is based upon the natural convection model for reservoirs which has been studied by many researchers (e.g. [2-7, 13, 15, 16, 18, 20, 31, 32]), none of them has investigated the case with the inclusion of a particle transport model. The studies concerning particle transport in various types of fluids are briefly reviewed below. The physical processes of particle transport have been discussed by numerous researchers using different methods including physical experiments (e.g. [33, 34]), numerical simulations (e.g. [35]), or the combination of both (e.g. [36]). The numerical study is the focus of the present review. Of all the numerical studies, the theory behind modelling particle transport driven by fluids has been reviewed by Guha [11]. The numerical particle transport models have been applied to multiple disciplines, such as chemical engineering (chemical aerosols [37]), medical science and engineering (respiratory tract [11, 38, 39]), environmental science (indoor air pollution [40-42]), mechanical engineering (heat transfer equipment [43]), and many other fields. The following section discusses the different approaches commonly applied in the numerical models, covering the studies of both laminar and turbulent flows.

Eulerian-Eulerian approach vs. Eulerian-Lagrangian approach

Existing studies of two-phase problems generally involve two different approaches, i.e. the Eulerian-Eulerian and Eulerian-Lagrangian approaches. Since the fluid phase is usually solved in the Eulerian framework, the major distinction between the two approaches is in the treatment of particle motion, which may be solved using either the Eulerian or Lagrangian approach.

In the Eulerian framework, particle trajectories are calculated in the same way as the calculation for a continuum. The calculation is from the macroscopic point of view for the whole system. It is typically useful when the volume fraction of particles is very large compared to the volume of fluid. The Eulerian approach has been adopted by many authors in recent years (e.g. Pilou [9], Guha [11], and Yan et al [44]). In this approach, the particle trajectory is treated as a continuum based on the conservation of momentum and energy. Several new models are available in the contemporary research in this field, among which the Volume of Fluid (VoF) model is one of the most widely adopted models.

In the Lagrangian framework, the individual particle is tracked by solving Newton's second law of motion. Details concerning the various forces can be found in the previous section of particle transport theory. The Lagrangian approach has been widely used for particle tracking with a relatively small volume fraction of particles in a continuum phase. As this approach attempts to track individual particle's motion within the fluid field, the required computing resource is very high when the number of particles within the flow domain is large. Many investigations reported in the literature have adopted this approach. In the laminar flow regime, the Lagrangian framework of the particle modelling method has been applied to predict the particle motion in a square cavity (e.g. [12]), whereas in the turbulent flow regime, this approach has been adopted by many authors, such as Dehbi and Martin [35] and Xu and Yu [45] to simulate particle motion.

Both of the two approaches for particle tracking have distinct traits when they are adopted in different scenarios. Guha has discussed and compared both of them in various numerical scenarios [11]. It is reported that both approaches can provide results with a high degree of consistency in numerical simulations; so the choice depends on considerations such as the physics of the flow and/or the volume fraction of the particles. In the present project, the Lagrangian framework is employed to track particles with a very small volume fraction of particles in the reservoir model. Typically, the value of the volume fraction of the discrete phase is limited to approximately 10% in commercial CFD codes using the Lagrangian framework.

One-way coupling vs. two-way coupling

The particle motion in fluids can be treated as either one-way coupling or two-way coupling. For the one-way coupling the particle motion has no impact on the continuous phase calculation, whereas for the two-way coupling the impact of the particle motion on the continuum will be considered.

The one-way coupling approach has been widely adopted in the literature (e.g. Akbar [12]). The flow regime is often assumed to be laminar in the numerical simulation using this approach. This is appropriate if the volume fraction of particles is small and the momentum loading due to the presence of particles is insignificant. Therefore, the interaction between the discrete phase and the continuum phase would not change the result significantly and thus could be neglected. The calculation with one-way coupling involves two separate steps: firstly, the flow field (the continuum phase) is solved; and secondly, the particle motion is resolved based on the result of the first step.

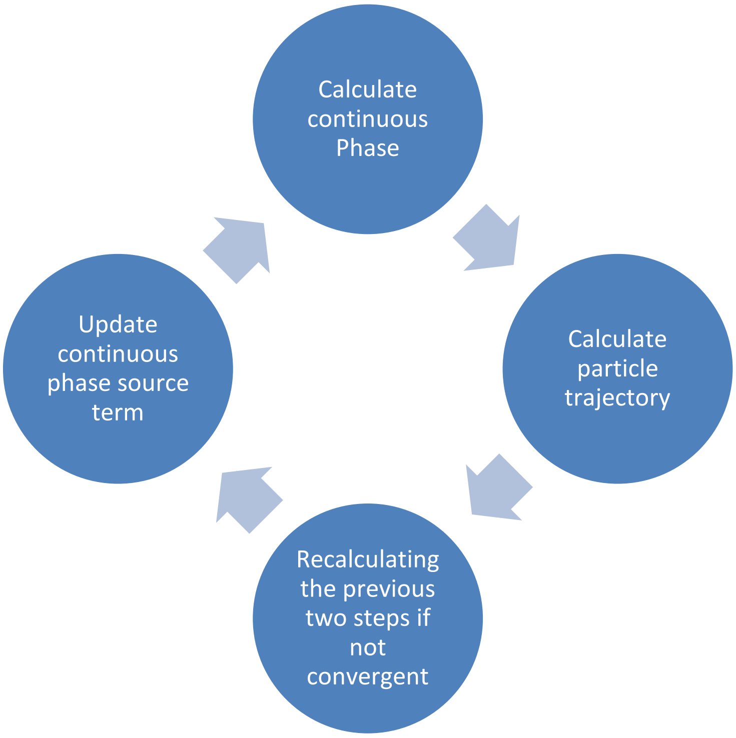

Figure 3 Coupled discrete phase calculations.

The two-way coupling approach is popular in turbulent flow models, and has been employed by many authors (e.g. Kondaraju et al [46], Xu and Yu [45], Dehbi et al [35, 47] among many others). In this approach, the solver conducts the calculation between the continuous phase and the discrete phase; and all the equations involved in these two phases are solved simultaneously (see Figure 3). Although this approach significantly increases the demand of computing resources, the outcome is more accurate result, especially if the volume fraction of particles is high.

Both the one-way coupling and two-way coupling have a place in the numerical modelling of particle transport. Generally, one-way coupling is adopted when the fluid flow is slow and comparably stable in the case with a low volume fraction of particles. On the other hand, the two-way coupling is often adopted for more intensive and unstable flows (i.e. turbulent flows) for better accuracy.

1.2.2.3 Particle transport in different flow regimes

Particle transport in laminar flows

To the best knowledge of the author of this thesis, few studies have been published on particle transport in natural stored waters with a laminar flow regime under natural convection. Most existing studies of particle transport have considered air flows in cavities (e.g. [12]). Here, the studies of particle motion in laminar flows are discussed.

Pratsinis et al [48] carried out a study of particle diffusion, thermophoresis, and coagulation in a laminar tube flow of gases. The relationship between coagulation and deposition of particles in a specific tube was demonstrated by the authors. The particle collision model adopted in their investigation was based on the above-described probabilistic model. Their study indicated that the process of coagulation tended to lower the particle deposition efficiency. This may be due to, as noted by the authors, the increase of the particle size enabling the thermophoresis to be a dominant mechanism for particle transport. As a consequence, the process of thermophoresis can be viewed as a resistant force for deposition in the gas flow.

Tsai and Liang [49] determined a correlation for thermophoretic force in evaluating the effect of the particle (aerosol) deposition in a laminar flow under the Eulerian – Lagrangian framework. They analysed the deposition rate of particles using correlated deposition fluxes. However, their estimation was limited to a certain range of Reynolds number, and the effect of natural convection was neglected.

In order to investigate particle motion under the effects of the flows and different particle properties in natural convection, Akbar et al. [12] compared the results obtained under various scenarios which account for certain forces such as drag, lift, thermophoresis, and Brownian dispersion respectively in a square domain. Their simulation was based on the Eulerian – Lagrangian approach. Their result indicated the importance of considering the submicron forces for particles of submicron scales. The result was found to be consistent with the investigation reported in [11] which showed that the Brownian diffusion decreased with the increase of the particle size. In [12], when the particles were smaller than 1 micron, Brownian diffusion dominated their behaviour, and the particle deposition rate was reduced. However, there was no direct comparison with any experiments and/or analytical results, and the verification of grid independence of the simulation was not discussed by the authors either.

Guha [11] studied the fractional deposition of particles in human's respiratory tract in the laminar flow regime based on the Eulerian – Eulerian approach. The effect of the particle size was considered and compared. The critical Reynolds number which separates the laminar and turbulent flow regimes was determined. They classified the dominant particle deposition mechanisms according to different ranges of the particle size.

Particle transport in turbulent flows

Numerous studies have focused on particle transport in turbulent flows. These include in-door air pollution models [9, 40, 41, 50], respiratory tract and lung models [39, 40], coolant systems models in a nuclear plant [35], and bubble in liquid flow models [51-57]. They consist of both numerical and experimental works. The numerical models are based on either Eulerian-Eulerian frameworks or Eulerian-Lagrangian frameworks for the fluid and particle coupling. These studies generally aim to understand the fate of particles in terms of deposition and diffusion rates. In the turbulent flow models, the information of particles is mainly derived employing a stochastic method based on a probabilistic model since it can significantly reduce computational time. Many turbulent flow models have been verified and validated (e.g. [44, 51]).

Guha [11] and Nerisson et al. [58] investigated the relationship between the deposition velocity and the particle relaxation time. Both these studies theoretically compared the diffusion and deposition of particles based on the two Eulerian-Eulerian and Eulerian-Lagrangian frameworks. Furthermore they characterised the particle deposition in turbulent flows in multiple regimes including the turbulent diffusion regime, the impaction regime, and the particle inertia regime. Guha [11] also detailed the driving mechanisms for the particle deposition, where the focus was on comparing the two approaches, and the numerical results were compared with the existing data. On the other hand, Nerisson et al [58] improved the boundary conditions for particles in the turbulent flow model. A new boundary condition at smooth walls was developed. Their study was validated against the experiments reported in [59, 60].

The recent study by Pallares and Grau [61] investigated the relationship between the normalised particle deposition velocities, the particle relaxation times, and Archimedes number (defined as the ratio of gravitational forces to viscous forces of fluids) for air channel flow induced by natural convection. It was found that an increase of the particle relaxation time results in the growth of the particle deposition rate within a specific range of the particle relaxation times. It was also revealed in their study that gravitational acceleration in this case would produce higher deposition velocities compared to the conditions without gravity. However, their study was constrained by a simple force model since the lift force, Brownian force, and thermophoretic force have been neglected.

Friedlander and Johnstone [62] conducted an experiment and analysis of the particle deposition mechanisms a few decades ago. The behaviour of particles depositing at a wall and the mechanism of their transport were addressed. Their study identified the importance of the inertia effect of eddies contributing to the particle motion in a turbulent gas flow. The relationship between the deposition rate and the distance between the entrance and the settling place of particles was analysed. The experimental data and their analysis showed the feasibility of predicting the rate of particle transfer based on the Reynolds analogy, which states that the heat transfer in a turbulent system is analogous to the turbulent momentum transfer [63]. However, the Reynolds analogy is only valid when the drag in fluids is insignificant.

Further, Xu and Yu [45] investigated the inter-particle interaction by including a particle collision model. The simulation was based on CFD coupled with a discrete phase model (DPM) under the Eulerian-Lagrangian framework. Their study focused on individual particle trajectories in a gas-solid fluidized bed model, and demonstrated the behaviour of particles subject to collision.

In general, particle transport in turbulent models mainly adopts stochastic tracking of particles in order to detect a correlation between the particle properties and the particle deposition rates. The turbulent models may be a better representation of the real-life situation than the laminar models. However, there are still many unsolved issues related to the turbulent models requiring further investigation.

1.2.3 Summary

As described above, the studies of laminar natural convection in reservoir models have been reported by many authors using various research methods including physical experiment (e.g. [5, 6, 15]), numerical simulation (e.g. [15]), and theoretical analysis (e.g. [19]). The establishment of exchange and mixing in the reservoir models under different types of thermal forcing have been demonstrated and quantified. Collectively, these studies have produced convincing and consistent results regarding the basic flow mechanisms under the effect of natural convection, which are the basis for further investigations, especially those concerning the transport of particular matters across natural water bodies.

The numerical modelling of particle transport reviewed above covers a wide range of applications in various fields. Some of these studies involve particle transport under the effect of natural convection, which is the interest of the present project. Many of these studies have employed turbulence models (e.g. [11]) and demonstrated the accuracy of the numerical results (e.g. [44, 51, 53, 64]).

The above literature survey has also demonstrated that none of the existing studies in the literature has investigated particle transport under natural convection in reservoirs and lakes. However, the numerical simulation of the transport of pollutant particles in natural water bodies is worth pursuing as it may produce more reliable and more detailed data than the pure statistical model (e.g. [65]) currently applied in environmental engineering fields.

1.3 Aims of the thesis

The aim of this project is to understand and quantify particles transport in a reservoir model under the influence of natural thermal forcing. Through this research the behaviour of suspending particles in water within the reservoir model is examined under various scenarios and it is expected that the results will have implications to the water quality management for reservoirs.

This project has the following three specific components:

1. Numerically modelling a previously reported concurrent particle image thermometry and velocimetry experiment in a reservoir model and investigating the dependence of the flow response on thermal forcing using the information extracted from passive particles;
2. Understanding the importance of natural convection in determining particle deposition and dispersion behaviours in reservoirs in a pseudo real-life scenario;
3. Preliminarily investigating the effect of a particle collision model on the spectrum of particle sizes as well as the deposition and dispersion of particles in comparison with the above model without particle collision.

1.4 Outline of thesis

The organisation of this thesis is as follows:

Chapter 1 provides a background for the research topic and a survey of the existing literature on natural convection in reservoirs and particle transport in fluids.

Chapter 2 discusses the numerical methods adopted in this project.

Chapter 3 reproduces a previously reported concurrent PIT/PIV experiment using a CFD code coupled with a DPM. Both qualitative and quantitative results obtained from the numerical simulation are discussed and compared with the previously reported experiment. A parametric study is also carried out using the numerical model to determine the dependence of the flow response and its stability properties on the Grashof number.

Chapter 4 deals with the motion of pollutant particles injected from the sidearm of the reservoir model. In addition to providing a qualitative comparison of the results of particle motion obtained with different particle properties and fluid flows, the study also attempts to quantify the effect of the Grashof number on particle deposition and dispersion behaviours in the reservoir model. A case study of a recent event with potentially severe effects to the quality of supply water is also discussed.

Chapter 5 is concerned with the particle motion in the reservoir model with the inclusion of a particle collision model. The extended numerical model is investigated based on the same scenario as that discussed in Chapter 4. Numerical results are presented in terms of particle size distribution and dispersion and deposition rates. These are compared with the results obtained using a non-colliding particle model.

Finally, Chapter 6 summarises the major results of the thesis and makes certain recommendations for future work.

2. Numerical methodology

The numerical methodology adopted in this thesis project is described in this chapter. In addition to providing the details of the numerical model formulation, which includes the fluid flow model and the particle transport model, this chapter also describes the normalisation and the numerical schemes adopted in subsequent simulations to be presented in the following chapters.

2.1 Fluid flow model

2.1.1 Geometry

A two-dimensional (2D) reservoir model is considered, which includes a region with a sloped bottom and the other adjacent deep region of a uniform depth, as shown in Figure 4. Here, L and L_1 are the horizontal lengths of the reservoir model as shown in the figure, H the maximum water depth, and S the inclination of the sloped bottom. The numerical model is based on a laboratory-scaled reservoir model (i.e. [6]). In order to avoid singularity at the tip in the numerical simulation, the region with the sloped bottom is cut off following the scale reported in [20], and an extra adiabatic and no-slip wall is assumed there (refer to Figure 4).

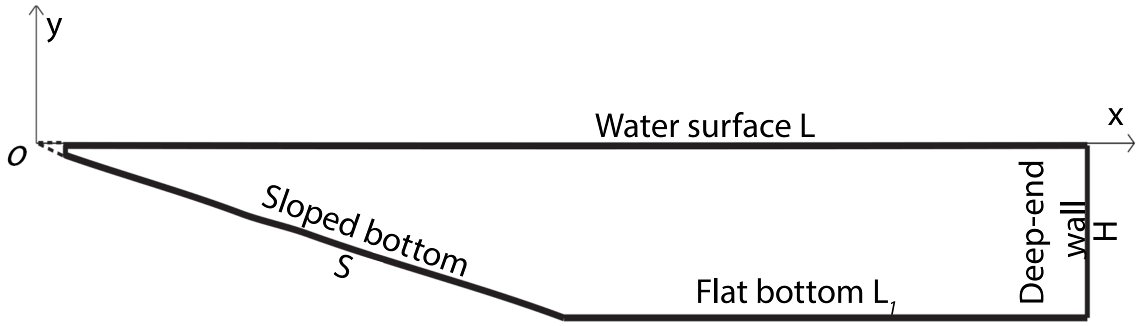

Figure 4 Schematic of the numerical model (not to scale).

2.1.2 Boundary conditions

In the fluid flow model, the rigid no-slip boundary condition is assumed for all the boundaries except for the water surface, the boundary condition of which depends on the case being investigated and will be specified separately. With reference to the thermal boundary conditions, a standard sinusoidal function of temperature is prescribed at the water surface in the numerical model:

$$T_t = T_0 + \frac{\Delta T}{2}\sin(2\pi\, t/P) \quad (\text{at } y = 0) \tag{15}$$

Apart from the water surface which has a prescribed temperature variation, all the sidewalls and bottoms are assumed to be adiabatic. The flow is initially stationary with a uniform temperature T_0.

2.1.3 Governing equations

The fluid flow motion and temperature change within the reservoir model are governed by the usual Navier-Stokes and energy equations with Boussinesq assumption [66]:

$$\frac{\partial u_x}{\partial x} + \frac{\partial u_y}{\partial y} = 0 \tag{16-1}$$

$$\frac{\partial u_x}{\partial t} + u_x\frac{\partial u_x}{\partial x} + u_y\frac{\partial u_x}{\partial y} = -\frac{1}{\rho_0}\frac{\partial p}{\partial x} + \nu\left(\frac{\partial^2 u_x}{\partial x^2} + \frac{\partial^2 u_x}{\partial y^2}\right) \tag{16-2}$$

$$\frac{\partial u_y}{\partial t} + u_x\frac{\partial u_y}{\partial x} + u_y\frac{\partial u_y}{\partial y} = -\frac{1}{\rho_0}\frac{\partial p}{\partial y} + \nu\left(\frac{\partial^2 u_y}{\partial x^2} + \frac{\partial^2 u_y}{\partial y^2}\right) + g\beta(T - T_0) \tag{16-3}$$

$$\frac{\partial T}{\partial t} + u_x\frac{\partial T}{\partial x} + u_y\frac{\partial T}{\partial y} = \kappa\left(\frac{\partial^2 T}{\partial x^2} + \frac{\partial^2 T}{\partial y^2}\right) \tag{16-4}$$

2.2 Particle transport model

2.2.1 Particle injection

The particle transport model is built upon the fluid flow model with particles injected into the computational domain. The injection of particles takes place within the working fluid. The initial locations of the injected particles as well as the time of the particle injection vary from case to case, and will be specified in each of the studies described in the following chapters. In general, the injection of particles is done using a purposely generated file, which specifies particle positions, properties, and initial velocities. In each investigation carried out in this thesis, all the injected particles have identical properties, including the same initial temperature, density, diameter, and a zero initial velocity. The particles are assumed to be insoluble and chemically non-reactive in the numerical model, and take on the temperature of the surrounding fluid at each location.

2.2.2 Boundary conditions

In the DPM, ‘reflect’ and ‘trap’ wall boundary conditions for particles are adopted in the numerical simulations, depending on the setup of the individual problems. For the ‘reflect’ wall boundary condition, any particle reaching the wall will be bounced back. The restitution coefficient, which measures the ratio of the particle speed after an impact to its speed before the impact, is used to calculate the velocity of the particle in the numerical model after bouncing. The restitution coefficient has been reported to be in the range between 0.8 – 1 depending on the fluid properties [34, 67, 68]. In a particular particle-wall collision experiment reported in [34], it was found that the restitution coefficient was 0.8 when a glass particle impacted a wall submerged in water. This is believed to be similar to the situation with the inert particles impacting the wall here. Accordingly, the restitution coefficient is set to 0.8 for the ‘reflect’ wall boundary condition. The standard reflection rules are followed to determine the direction of the particle motion after colliding with the walls. The re-bouncing process is assumed to have no influence on any internal property of the particles in the numerical model. For the ‘trap’ wall boundary condition, any particle reaching the wall will be deposited and removed from the flow domain, and consequently will not be involved in subsequent calculations.

2.2.3 Governing equations

The numerical simulation of particle motion depends on the fluid flow. Particle tracking is based on the Lagrangian framework and adopts Newton’s second law of motion in the DPM. The governing equation for particle motion is given by Equation (1) in Chapter 1.

2.3 Normalisation and numerical procedures

The governing equations of the fluid flow are normalised using the following scales: Length $(x, y) \sim H$; velocity $(u_x, u_y) \sim \kappa/H$; time $(t, P, \tau) \sim H^2/\kappa\ (= t_f)$; temperature difference $(T - T_0) \sim \Delta T$; pressure gradient $(\frac{\partial p}{\partial x}, \frac{\partial p}{\partial y}) \sim \rho_0 g\beta\Delta T$. The normalised governing equations are rewritten as:

$$\frac{\partial u_x^*}{\partial x^*} + \frac{\partial u_y^*}{\partial y^*} = 0 \tag{17-1}$$

$$\frac{\partial u_x^*}{\partial t^*} + u_x^* \frac{\partial u_x^*}{\partial x^*} + u_y^* \frac{\partial u_x^*}{\partial y^*} = -Pr^2 Gr \frac{\partial p^*}{\partial x^*} + Pr\left(\frac{\partial^2 u_x^*}{\partial x^{*2}} + \frac{\partial^2 u_x^*}{\partial y^{*2}}\right) \tag{17-2}$$

$$\frac{\partial u_y^*}{\partial t^*} + u_x^* \frac{\partial u_y^*}{\partial x^*} + u_y^* \frac{\partial u_y^*}{\partial y^*} = -Pr^2 Gr \frac{\partial p^*}{\partial y^*} + Pr\left(\frac{\partial^2 u_y^*}{\partial x^{*2}} + \frac{\partial^2 u_y^*}{\partial y^{*2}}\right) + Pr^2 Gr T^* \tag{17-3}$$

$$\frac{\partial T^*}{\partial t^*} + u_x^* \frac{\partial T^*}{\partial x^*} + u_y^* \frac{\partial T^*}{\partial y^*} = \frac{\partial^2 T^*}{\partial x^{*2}} + \frac{\partial^2 T^*}{\partial y^{*2}} \tag{17-4}$$

In the above equations, the asterisked symbols denote the normalised quantities of the corresponding dimensional ones. The Prandtl number (Pr) and Grashof number (Gr) along with other dimensionless parameters characterising the geometry of the model and the time period of the cyclic thermal forcing are defined as follows:

$$Pr = \frac{\nu}{\kappa} \qquad Gr = \frac{g\beta\Delta T H^3}{\nu^2} \qquad A = \frac{H}{L} \qquad S = \frac{H}{L - L_1} \qquad P^* = \frac{P\kappa}{H^2} \tag{18}$$

The governing equations along with the above described boundary and initial conditions are solved using the commercial CFD package FLUENT 13 which is a finite-volume-based solver. A second-order time-accurate formulation is employed for temporal discretisation, and the SIMPLE scheme is adopted for the pressure-velocity coupling. The discretisation of all the convective terms is by a second-order upwind scheme, whereas that of the diffusion terms is by a second-order central-differencing scheme.

A non-uniform grid is constructed for all the cases described in this thesis with finer grids distributed in the vicinity of all the wall boundaries, close to the tip region and around the centre of the computational domain where the slope finishes. The particle motion is solved by integrating the equation of Newton's second law of motion (i.e. Equation (1)) with the calculated flow field following the Eulerian-Lagrangian approach. A one-way coupling method is adopted in the numerical model, which means that the motion of particles does not affect the flow. All results reported here are obtained using a double precision solver.

3. Numerical modelling of a concurrent PIT/PIV experiment with TLC particles

3.1 Introduction

Inflows into reservoirs from sidearms under the effect of natural thermal forcing may carry nutrient and/or pollutant particles. An understanding of the transport processes of these particles is important for predicting the dynamic quality of the water body in reservoirs and lakes so that a precautionary strategy can be set up to prevent the deterioration of the water quality. A particular transport process of interest is the one induced by periodic day-time heating and night-time cooling. The process is significant for the near shore transport of contaminants in field situations.

Over a typical diurnal cycle, the intensity of the thermal forcing changes with time, which results in switch between heating and cooling at the water surface. Therefore, the overall diurnal cycle includes two distinct phases: a day-time heating phase and a night-time cooling phase. The typical flow structures under such changing thermal forcing conditions are reported in [14]. The investigation is based on a model that consists of two distinct regions including a region with a sloped bottom and the other with a uniform depth. During the day, when both the shallow and deep regions are exposed to uniform heating from the water surface, the shallow region heats up relatively more quickly than the deeper region. As a consequence, the average temperature over the local water depth increases with the decreasing depth from the deeper region towards the littoral region, resulting in a horizontal temperature gradient. The lateral temperature gradient in turn initiates a convective flow up along the slope and out of the tip region along the surface. The convective flow resulting from the day-time unequal heating is an important mechanism for pollutant/nutrient exchange and mixing in reservoirs. Further, in shallow waters under the presence of solar radiation, if the water depth is less than the penetration depth of solar radiation, a fraction of the solar radiation reaches the bottom and is absorbed and then re-emitted by the bottom. As a consequence, the bottom heating may cause a Rayleigh-Benard type instability, resulting in a secondary convection in the form of rising plumes. These two types of convective flows can act together to form a complex convective flow across both the shallow and deep regions during the day. The bottom heating resulting from solar radiation, however, does not happen in a cloudy day because of the shading effect; therefore, the secondary convection does not occur in this situation.

Similarly, in the night-time cooling phase, the heat loss from the surface is approximately uniform across the surface, and again, the changing water depth results in a decrease of the average temperature in the shallow region relative to the deeper region, and a horizontal temperature gradient is also established. The result of this cooling effect is a cold water undercurrent proceeding towards the deeper region along the slope. In the meantime, cooling at the water surface may cause a Rayleigh-Benard type instability in the form of plunging plumes issuing from the thermal boundary layer underneath the surface. The resultant convective flow is a large-scale circulation across the whole domain superimposed by the secondary convective circulations.

Natural convection in reservoir models has been studied by many authors using various methods, including numerical simulations (e.g. [3, 4, 14-16, 69]), laboratory experiments (e.g. [5, 6, 17]), and theoretical analyses (e.g. [2, 7, 13, 18-20]). The thermal forcing conditions considered in these studies include constant day-time heating, constant night-time cooling, and periodic diurnal thermal forcing etc. In the case with diurnal thermal forcing, Lei and Patterson [14] performed a numerical simulation with a periodic isoflux condition at the surface; in contrast, Bednarz et al. [16] considered the diurnal flow response to a periodic temperature variation at the surface in their numerical model. These studies (e.g. [14, 16]) have revealed that distinct flow instability occurs during the cooling phase under periodic thermal forcing regardless of the type of thermal forcing (i.e. isoflux, isothermal, or radiation heating). In addition to the periodic heating and cooling at the surface, the study reported in [14] also considered re-emission of residual radiation by the bottom under radiation heating and showed that instability also occurred during the heating phase because of an adverse temperature gradient in the bottom layer. Most of the studies of the flow response to diurnal thermal forcing (e.g. [1, 2, 14, 16]) have confirmed a time lag in the overall flow response to the switch of the thermal forcing. Despite that all these studies have showed similar flow behaviour, no direct comparison was made among them.

In the concurrent Particle Image Thermometry and Particle Image Velocimetry experiment reported in [6], a cycling temperature was applied to the water surface. Thermo-chromic liquid crystal particles were used as both temperature indicators and tracers for the PIV measurements, allowing for simultaneous mapping of the temperature and velocity fields. The experiment revealed both the temperature and velocity structures at different thermal forcing stages of the cycling temperature. As well as providing qualitative data such as contour plots of the temperature and velocity, the experimental investigation has also quantified some important flow parameters such as the horizontal exchange flow rate and the time lag of the flow response to the switch of the thermal forcing.

In this chapter, the concurrent PIT/PIV experiment described in [6] is numerically reproduced using a finite volume CFD solver coupled with a Discrete Phase Model. Visualisations and measurements of the temperature and velocity fields are carried out based on the information derived from discrete particles, the processes of which are similar to those adopted in the concurrent PIT/PIV experiment [6]. The numerical model is first verified in terms of the numerical accuracy and validated against the reported experiment. Subsequently, a parametric study using the validated numerical model is carried out to investigate the dependence of various flow and stability properties on the Grashof number under the periodic thermal forcing conditions.

The organisation of the rest of this chapter is as follows:

In Section 3.2, a two-dimensional reservoir model is formulated following the description in Chapter 2 with specific modification relevant to the present problem.

In Section 3.3, three numerical tests are conducted to verify the accuracy of the numerical model. Firstly, grid and time-step dependency tests are conducted to identify an optimum grid system. Secondly, the passiveness of particles is tested to confirm the properties of the particles in order to best reproduce the particle motion reported in the TLC experiment [6]. Finally, the effects of particle numbers and minor forces on the particle transport model are tested to identify the optimal numerical settings in the DPM.

In Section 3.4, validation of the numerical model is carried out by comparing the results of the particle temperature contours (isotherms) and flow velocities between the simulation and the experiment [6]. Subsequently, quantitative comparisons between the experiment and simulation are made in terms of the horizontal exchange flow rate and the time lag of the flow response to the switch of the thermal forcing.

In Section 3.5, the results of a parametric study are presented to illustrate the dependence of the flow and its stability properties on the Grashof number. The role of the Grashof number is examined in terms of the onset time for the instability, the time duration of the unstable phase, and the time lag of the flow response to the switch of the thermal forcing.

The chapter closes with Section 3.6 in which the overall results are summarised and the outcome of this study is briefly discussed.

3.2 Model formulation

Fluid flow model

The two-dimensional reservoir model described in Chapter 2 is adopted in this chapter. The dimensions of the numerical model are the same as those of the laboratory reservoir model adopted in the concurrent PIT/PIV experiment [6], as shown in Figure 5. It is worth noting that the orientation of the reservoir model shown in Figure 5 is different from that shown in Figure 4 in Chapter 2. This is to facilitate the comparisons with the experimentally generated images. In order to avoid singularity at the tip in the numerical simulation, the region with a sloped bottom is cut off at 2.4 mm from the tip end [20], and an extra adiabatic and no-slip wall is assumed there (refer to Figure 5).

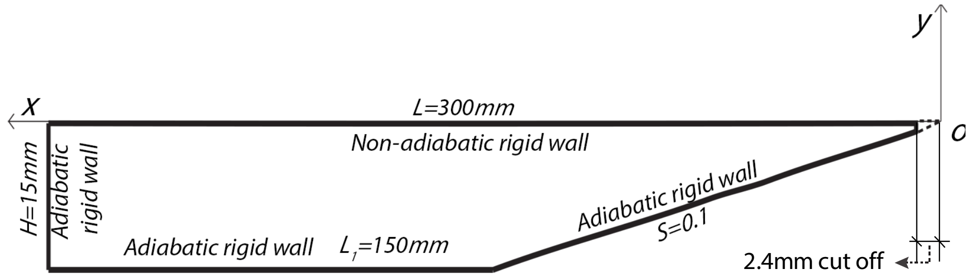

Figure 5 Schematic of the numerical model (not to scale).

In the PIT/PIV experiment [6], the thermal forcing was imposed at the surface through a water bath with a rigid bottom made from a copper sheet, which was in direct contact with the water surface. The temperature of the water bath was cycled in a periodic fashion (refer to Figure 6) by circulating water at controlled temperatures through it. Accordingly in the numerical model, a rigid no-slip boundary condition is assumed at the surface. In order to reproduce the experimental temperature condition at the surface, a standard sinusoidal function of temperature is prescribed at the water surface in the numerical model (refer to Equation (15) in Chapter 2 and the red curve in Figure 6 with comparison to the experimental temperature condition – the grey curve).

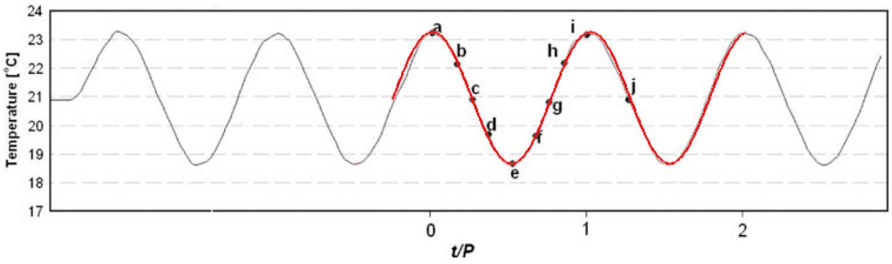

Figure 6 Experimental time series of the temperature at the water surface [6] (the grey line) compared with the numerical boundary condition of the surface temperature (the red line).

Here the annotations {a}-{f} in Figure 6 indicate the different time instants over the two thermal forcing cycles when flow is quasi-steady. The discussion of flow evolution at these time instants will be referred to later in Section 3.4.1.

The initial conditions for the numerical model are determined according to the experimental conditions, i.e. the water within the model is initially stationary with a uniform temperature of $T_0 = 20.9$°C.

Particle transport model

Since one of the purposes of this investigation is to reproduce the concurrent PIT/PIV experiment described in [6], the role of the particles in the numerical simulation is thus to indicate the fluid temperature and the flow motion, and the particles in the numerical model are injected into the flow in accordance with the experimental condition. In the experiment, the TLC particles were well mixed in water prior to starting the experiment, and the water seeded with TLC particles was in a stationary state at the start of the experiment. Accordingly in the numerical model, particles are randomly distributed throughout the computational domain at the initial time. All the injected particles have identical properties, including the same initial temperature, density, diameter, and a zero initial velocity. This is a slight simplification of the experimental condition as the size of the TLC particles used in the experiment was likely to vary over a certain range. Since the particle properties may affect their suspension ability and the specific detail of the TLC particles adopted in [6] is not readily available, they need to be determined with care. Accordingly, a numerical test will be carried out in Section 3.3 to determine the appropriate properties of the TLC particles for the numerical model.

In the present DPM, the ‘reflect’ wall boundary condition for particles is assumed on all the rigid walls including the water surface.

The non-dimensional parameters of Pr, A, S and P^* are determined from the PIT/PIV experiment [6] and fixed at 6.82, 0.05, 0.1 and 0.54 respectively. Gr will be varied over the range from 5.53×10^3 to 3.52×10^4. Unless specified otherwise, all the results presented below are derived from the temperature and velocity information of suspending particles.

3.3 Numerical tests

3.3.1 Grid and time-step dependency tests

Mesh and time-step dependency tests are carried out to ensure the accuracy of the numerical solution. Three different meshes with three corresponding time-steps are tested, which are 1722×102 mesh with a dimensionless time-step 7.29×10^{-7}, 861×51 mesh with a time-step 1.46×10^{-6}, and 430×26 mesh with a time-step 2.91×10^{-6}, respectively. The size of the mesh and the corresponding time-step are chosen so that the Courant-Friedrichs-Lewy (CFL) number [70] remains roughly the same for all of the three meshes. The test is carried out based on a case under constant temperature cooling at the water surface at a much higher Grashof number (i.e. $Gr = 10^6$) rather than the periodic heating and cooling cases described above. The Prandtl number is set to $Pr = 7$ for the test case. It is expected that the adopted test case is more unstable and thus more sensitive to the grid and time-step resolutions than the diurnal cases to be investigated in this chapter. Therefore, a suitable mesh with a corresponding time-step determined for the test case is deemed appropriate for all the diurnal cases to be calculated here. For the particle model in this test case only, particles of 1-μm in diameter and 10^3 - $\mathrm{kg/m^3}$ in density with a volume fraction of 1.40×10^{-4} are injected into the water body underneath the surface (at $y^* = -0.02$) along the region with a sloped bottom.

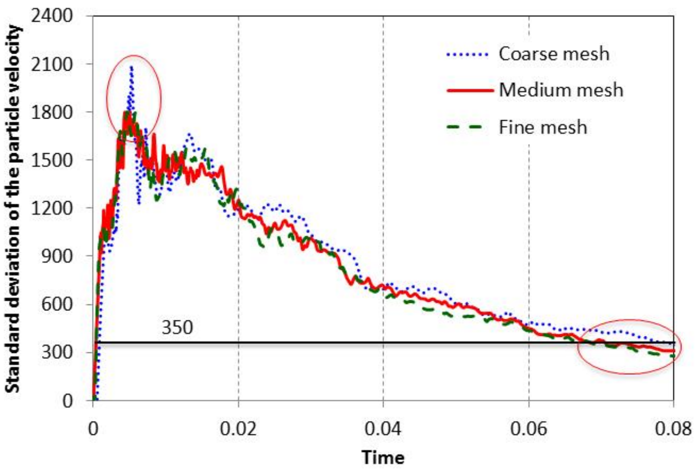

Figure 7 Time histories of the standard deviation of the particle velocity obtained with the three meshes.

The mesh and time-step dependence is examined based on quantitative data extracted from particle motions across the entire flow domain. The time series of the standard deviation of the velocity magnitude of all the suspending particles in the computational domain obtained with the three meshes are shown in Figure 7. It can be seen in this figure that the results obtained with the different meshes are very similar. Three distinct stages of the flow development can be identified in Figure 7, which include an initial stage with the standard deviation of the particle velocity increasing rapidly, an unstable transitional stage with strong flow instability and consequent fluctuation of the standard deviation of the particle velocity, and a relatively stable transitional stage with the standard deviation of the particle velocity decreasing steadily with time. Since a constant temperature is applied at the water surface and all other boundaries are adiabatic, the difference between the surface temperature and the average temperature of the water body diminishes with time. As a consequence, the flow becomes weaker and weaker and eventually dies out, so does the particle motion.

Based on the behaviour of the standard deviation of the particle velocity shown in Figure 7, we define a time lapse as the time difference between the time when the standard deviation of the particle velocity peaks (referred to as ‘Peak time’) and the time when the standard deviation drops to a low value of 350 (this value is arbitrary; the corresponding time is referred to as ‘Settling time’), and we calculate the time lapses for all the three cases with different meshes. The peak and settling time instants are indicated in Figure 7 (marked by the ellipses). The results are compared in Table 2, which demonstrates the convergence of the numerical results as the mesh and time-step are refined.

The above mesh and time-step dependence test shows that there is a significant improvement in the numerical accuracy when the medium mesh is employed in comparison with the coarse mesh. However, the variation of the numerical results between the medium and fine meshes is very small. Therefore, for a compromise between the numerical accuracy and the computational time, the medium mesh (861×51) and the corresponding time-step (1.46×10^{-6}) are chosen for the subsequent calculations.

Table 2 Comparison of the time lapses obtained with different meshes

Mesh resolution	1722×102	861×51	430×26
Peak time	0.0049	0.0050	0.0053
Settling time	0.0734	0.0746	0.0810
Time lapse	0.0686	0.0696	0.0757
Variation	-	1.46%	10.35%

3.3.2 Passiveness of particles

Before the particle transport model is applied in the present numerical study, the passiveness of the TLC particles in fluid flow needs to be tested. In the concurrent PIT/PIV experiment [6], the TLCs were assumed to behave fully passively in the flow. In this case the particles have a good suspension capacity in the flow and strictly follow the fluid stream; therefore, their motion is stable to the flow and can accurately reflect the fluid motion [71]. The passiveness of particles in fluid is characterised by the particle relaxation time (τ) [11]. Generally, a lower particle relaxation time means the particles behave more passively in fluid [72]. The particle relaxation time is defined as [11]:

$$\tau = \frac{d_p^2 \rho_p}{18\mu} \tag{19}$$

It is seen from Equation (19) that the passiveness of particles depends on both the diameter and density of the particles and is more sensitive to the diameter than to the density. Unfortunately, the exact values of the diameter and density of the TLC particles adopted in the experiment [6] are not available. Alternative information about TLC particle properties from other sources, including information from TLC suppliers (e.g. [73, 74]) and relevant publications (e.g. [75, 76]) suggests that the average diameter of TLC particles can vary from about several microns to over a hundred microns depending on the application. The density of TLC particles is usually very close to the density of water. Accordingly in this study, the optimum properties of the particles are determined numerically in order to properly reproduce the experimentally observed particle motion.

A numerical experiment is carried out by testing particle sizes from 50 microns down to 1 micron while keeping the density of the particles the same as water (at 20℃). The tested model corresponds to Case 1 listed in Table 3. Figure 8 shows the results obtained with three different particle diameters in the numerical simulation. Plotted in this figure is the particle distribution with the colour of the particles indicating the temperature of the surrounding water (referred to as particle temperature contours hereinafter). The black spots within the computational domain represent the region where no suspending particles are present. The time instant shown in Figure 8 is at $t/P = 3$ when the flow has become quasi-steady. It can be seen in Figure 8 that, for the particle diameter of 50 μm, a clear settling behaviour of particles occurs near the tip region of the model. The sedimentation of the numerical particles becomes more significant in later cycles. However, no noticeable settling of TLC particles was observed in the experiment [6]. As the diameter of the numerical particles is reduced to 10 μm, the settling of the particles becomes less significant, and when the diameter of the particle is reduced to 1 μm, the particles are seen to be sufficiently passive (see Figure 8). As will be further demonstrated below, the particle model with the smallest particle size can properly reproduce the TLC experiment described in [6]. Based upon this test, the smallest particle size (1 μm) is adopted for all subsequent numerical investigations.

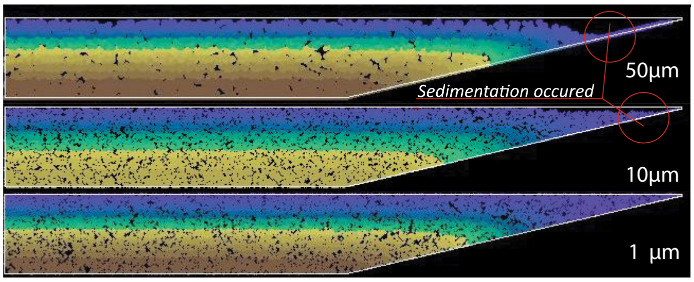

Figure 8 Particle temperature contours obtained for Case 1 (see Table 3) at $t/P = 3$ with different particle diameters.

3.3.3 Effect of particle numbers and minor forces in the particle model

Further tests are carried out to determine the effects of the quantity of the injected particles and the Brownian and lift forces on the numerical results. The quantity of the injected particles is measured by the ratio of the total volume of particles to the total volume of the surrounding flow domain (referred to as particle volume fraction). Three cases are calculated for this purpose, and the details of the three cases are given in Table 3 below.

Table 3 Parameters and settings of three test cases

Number of case	Particle volume fraction	Brownian force	Lift force	Grashof number
Case 1	1.12×10^{-3}	NO	NO	3.52×10^4
Case 2	1.12×10^{-3}	YES	YES	3.52×10^4
Case 3	2.24×10^{-3}	NO	NO	3.52×10^4

For quantitative comparison purpose, the exchange flow rate across the computational domain is evaluated from the particle motion. First a local horizontal exchange flow rate $Q_H(x)$ at a specific horizontal location x in the 2D domain is defined as follows (refer to [14, 20]):

$$Q_H(x) = \begin{cases} \dfrac{1}{2}\displaystyle\int_{-Sx}^{0} |u_{px}| dy & x < 0.15 \text{ m} \\ \\ \dfrac{1}{2}\displaystyle\int_{-H}^{0} |u_{px}| dy & x \geq 0.15 \text{ m} \end{cases} \tag{20}$$

where S is the inclination of the sloped bottom, and u_{px} is the horizontal component of the particle velocity.

Next the average horizontal exchange flow rate Q_H is calculated by integrating the local flow rate over the full length of the computational domain as follow:

$$Q_H = \frac{1}{L}\int_{0}^{L} Q_H(x) dx \tag{21}$$

Similarly, the vertical exchange flow rate is calculated as follows:

$$Q_V(y) = \frac{1}{2}\int_{-y/S}^{L} \left|u_{Py}\right| dx \tag{22}$$

$$Q_V = \frac{1}{H}\int_{-H}^{0} Q_V(y)dy \tag{23}$$

The average exchange flow rates calculated from above will represent the actual exchange flow rates in the reservoir model if:

1) The particles are evenly distributed within the computational domain;
2) The particles are fully passive; and
3) The particle volume fraction is sufficiently large.

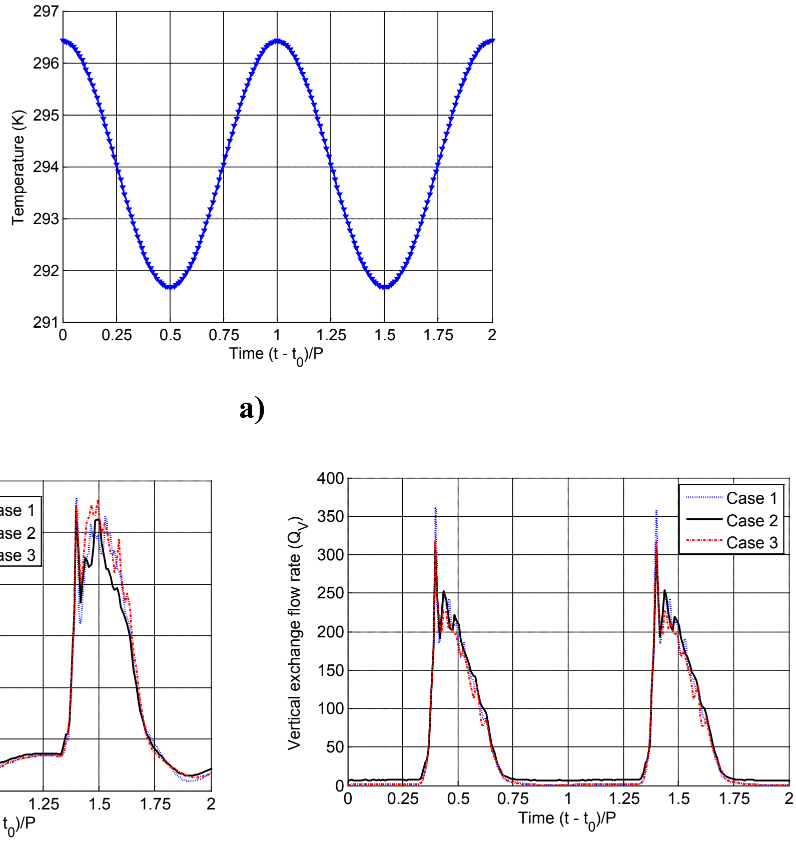

a)

b)

c)

Figure 9 Time series of a) the specified surface temperature for Cases 1-3; b) the calculated horizontal exchange flow rate; and c) the calculated vertical exchange flow rate.

The first two requirements have been discussed and tested above. The last requirement is tested below by comparing the cases with different particle volume fractions (Cases 1 and

3). The calculated horizontal and vertical exchange flow rates for all the three numerical cases are compared in Figure 9b and Figure 9c respectively. Here the two-dimensional exchange flow rates are normalised by the thermal diffusivity (κ), and the time is normalised by the period of the cycling thermal forcing. The initial time starts from $t_0/P = 3$ (i.e. after three full thermal cycles) when the overall flow has become quasi-steady.

As is seen in Figure 9, in general the three calculated cases show very similar behaviour in terms of the exchange flow rates. More specifically, the exchange flow rates calculated from Case 2 with the Brownian motion and lift force included are generally close to those calculated from Case 1. The comparison of the results obtained with different particle volume fractions (Cases 1 and 3) also shows a similar pattern. This observation suggests that the particle volume fraction is deemed to have no significant effect on the results.

However, minor variation between Case 1 and Case 2 can be observed in Figure 9. The flow intensity obtained from Case 2 is slightly higher than that obtained from Case 1 during the stable phase (approximately at normalised time of 0 – 0.3 and 0.8 – 1.25). This is because during the stable phase, the flow motion is very weak. In this case, the Brownian motion and the effect of the lift force become more significant. Discussion of the Brownian motion and lift force exerting on small particles can be found in the literature (e.g. [26, 77]).

As there is no significant difference in the overall results obtained from the three numerical cases, Case 1 will be adopted for further investigations. For all other cases with different Grashof numbers, the settings in the discrete phase model are the same as those for Case 1. That is, the particle volume fraction is 1.12×10^{-3}, and neither the Brownian force nor the lift force is considered.

3.4 Numerical results and comparison with the experiment

The TLC experiment with a Grashof number of $Gr = 3.52 \times 10^4$ described in [6] is numerically simulated with the aforementioned numerical model. The numerical result is compared with the experiment. Subsequently, a parametric study over a range of Grashof numbers will be carried out using the same numerical model. For all the numerical cases presented in this section, a periodic thermal forcing, similar to that shown in Figure 6, is applied at the top surface. In order to avoid the start-up effect and to focus on the behaviour of the flow and particles at the quasi-steady state, only the data obtained after the third thermal forcing cycle ($t/P > 3$, refer to Figure 6) are analysed and presented here.

In Section 3.4.1 below, the particle temperature contours (isotherms) and flow velocities obtained from the particles in the numerical simulation are compared with those in the experiment. In Section 3.4.2, quantitative comparisons between the experiment and simulation are made in terms of the horizontal exchange flow rate and the time lag of the flow response to the switch of the thermal forcing. In Section 3.4.3, the results of the parametric study are presented to illustrate the dependence of the flow and its stability properties on the Grashof number.

3.4.1 Transient flow response to periodic temperature variation

The transient flow responses to the periodic temperature variation are discussed and compared between the experiment and simulation in this section. The flow responses observed in the experiment and simulation are generally very similar. Both the experimental and numerical results reveal that the development of the flow and particle motion within each thermal forcing cycle can be classified into two distinct stages, a *stable stage* and an *unstable stage.* The distinct features of the flow structures at each of the two stages are illustrated below.

Stable stage

Heat transfer at the stable stage is dominated by conduction and a stable convection. A representative feature of the stable stage flow is a large-scale circulation within the domain (see Figure 10a) resulting from the lateral temperature gradient along the slope. This stage covers the time instants {a}, {b}, {c}, {i} and {j} (refer to Figure 6). At this stage, the overall effect of the thermal forcing on the water body is heating, though the surface temperature may be decreasing at some time instants (e.g. at {b} and {c}).

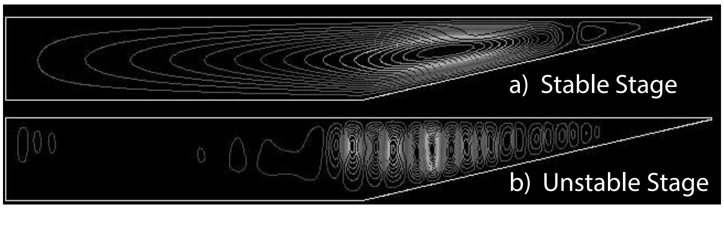

Figure 10 Contours of the stream function that represent the stable and unstable stages of the fluid flow: a) stable flow at the time instant {c}; b) unstable flow at the time instant {d}.

The cycle to be described below starts at the time instant {a} when the surface temperature has peaked and is about to decrease. At this time, the interior water has been heated up continuously during the second half of the previous cycle. As a consequence, the interior is stably stratified; and this can be seen from both the numerical contours and the PIT image in Figure 11a.

With the passage of time, the cooling effect initiates from the water surface although the overall effect of the thermal forcing on the water body remains to be heating (see Figure 11b and Figure 11c) since the surface temperature is still higher than the average temperature of the water body. At the time instant {b}, the temperature contours from the experiment and simulation are very similar, but a small variation between the experiment and simulation can be observed from the contours of the horizontal velocity component of the particles plotted in Figure 12a. The variation may be attributed to non-ideal adiabatic wall conditions in the experiment, which was discussed in [6]. At the time instant {c}, the temperature profile of the entire water body becomes almost uniform as shown in Figure 11c. At this time, the effect of the thermal forcing is about to switch to cooling.

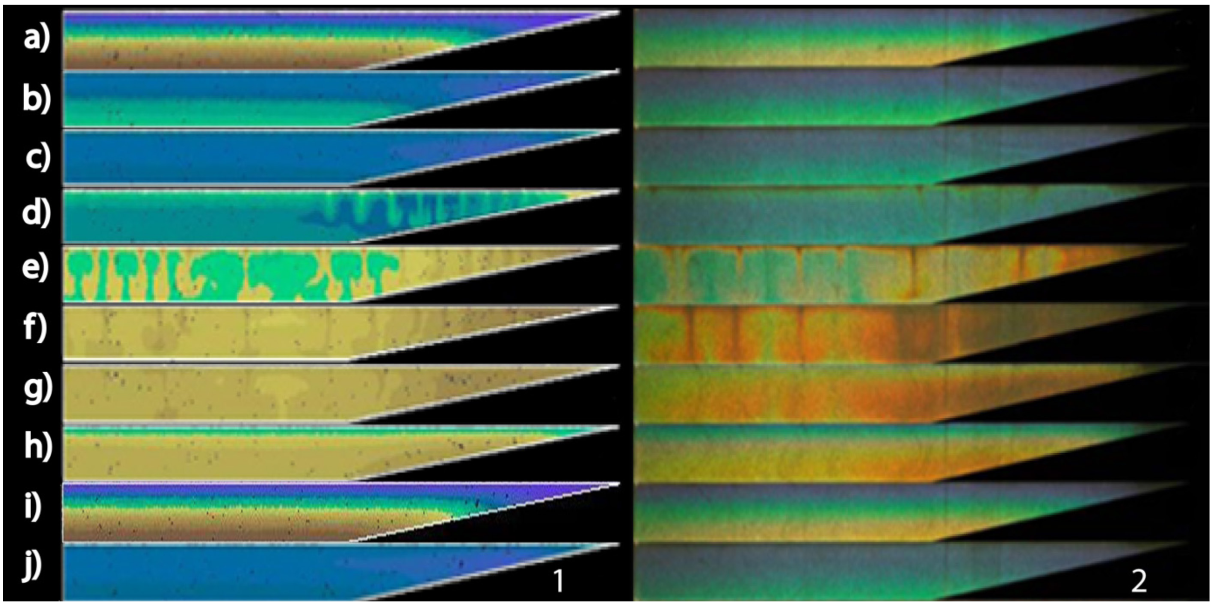

Figure 11 Temperature structures for *Pr* = 6.82 and *Gr* = 3.52 × 10^4. Left: particle temperature contours plotted from the particle temperatures in the numerical simulation (Case 1); Right: raw photographs of TLC particles taken from the experiment [6].

Subsequently the evolution of the flow response enters into an unstable stage (to be described below). For comparison purposes, the particle temperature contours at the time instant {i} (corresponding to {a}) and {j} (corresponding to {c}) in the following thermal forcing cycle are plotted in Figure 11. It is seen in this figure that the same temperature structures are repeated in the following cycle.

Unstable stage

Heat transfer at this stage is dominated by unstable convection. A distinct feature of the flow structures resulting from the presence of plunging plumes is demonstrated in Figure 10b. The unstable stage includes the time instants {d}, {e}, {f}, {g} and {h} when the overall effect of the thermal forcing on the water body is cooling, as shown in Figure 6.

At the time instant {d}, the distinct cold thermal boundary layer as well as relatively weak plunging thermals can be observed on the particle temperature contours obtained from both the numerical simulation and experiment (refer to Figure 11d). At this time, the local Rayleigh number in the surface layer has just reached a critical value [7], and thus the instability has not been fully developed. The direct observation of the particle temperature contours suggests that the general flow features are the same between the simulation and experiment at this time instant. However, a noticeable variation between the experiment and simulation can be seen in Figure 11d, in which the numerical flow is more unstable than the experimental flow. This may be attributed to the heat loss and non-ideal thermal boundary conditions in the experiment, which result in a lower effective Grashof number than the nominal value.

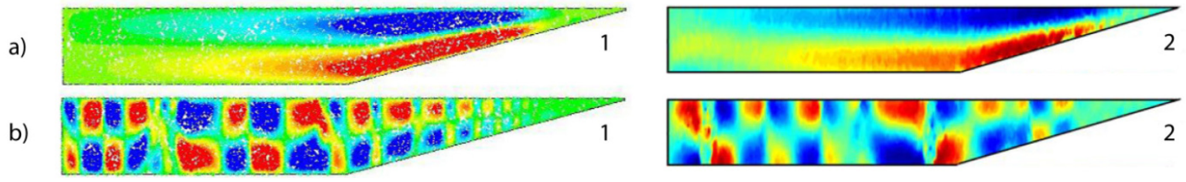

Figure 12 Contours of the horizontal velocity magnitude obtained for *Pr* = 6.82 and *Gr* = 3.52 × 10^4. Left: Numerical contours plotted from the particle velocity (Case 1); Right: contours of the particle velocity obtained from the PIV experiment [6].

As the surface cooling continues, the Rayleigh-Benard type instability is intensifying. At the time instant {e}, the surface temperature has reached its minimum and distinct plumes can be clearly seen across the entire cavity, as shown in Figure 11e. As a consequence, a cellular flow structure is formed in the cavity (see Figure 12b). Both Figure 11e and Figure 12b show very similar feature of the flow between the experiment and simulation. Further quantitative comparison between the experiment and simulation is carried out here. Figure 13a plots the horizontal velocity profile extracted along a horizontal line underneath the surface ($x^* \in [10,20]$, $y^* = -0.01$), and Figure 13b shows the corresponding spectrum of the velocity profile, from which a dominant wavenumber of $k = 25.99\ \mathrm{m}^{-1}$ can be identified. Given the length of the uniform-depth region of $L_1 = 0.15$ m, the number of pairs of the convection cells is obtained as follows:

$$n = kL_1 = 3.89 \tag{24}$$

In the experiment [6], the number of pairs of the convection cells at the same time instant can be approximately determined from the horizontal velocity contours shown in Figure 12b, which gives an approximate value of 4 over the region with a uniform depth. This is very close to the numerically predicted value of 3.89.

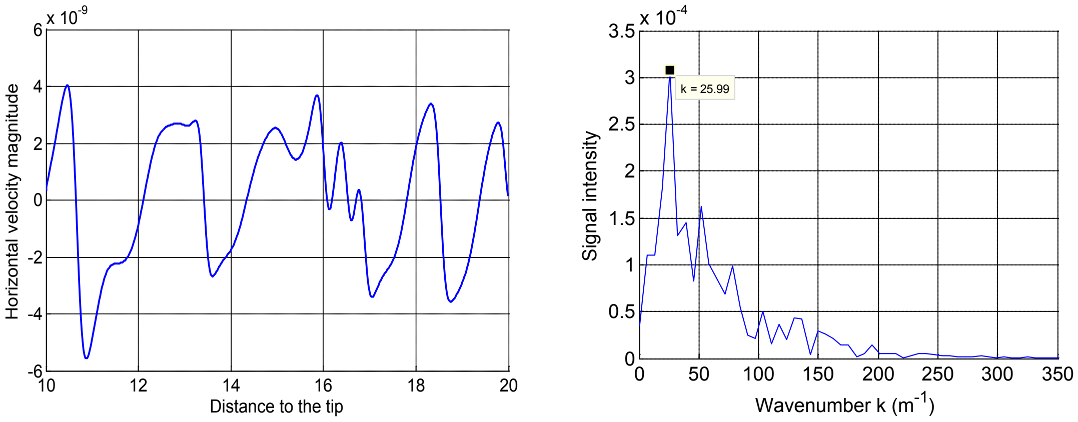

a) **b)**

Figure 13 a) Horizontal velocity profile along a horizontal line below the water surface obtained at the time instant {e}. b) The corresponding power spectrum of the horizontal velocity profile plotted in a).

The unstable flow associated with surface cooling remains distinct until the time instant {g}, although the surface temperature is increasing with time. This flow feature indicates a time lag of the flow response to the switch of the thermal forcing [6], which will be examined further in Section 3.4.2 below. By the time instant {h}, the flow has been stabilised and the overall temperature structure is a stable stratification expected under the surface heating condition. From the time instant {i} onwards, the above-described temperature evolution is repeated.

3.4.2 Horizontal exchange flow rate and time lag

3.4.2.1 Horizontal exchange flow rate

The horizontal exchange flow rate calculated using Equation (21) for the numerical case is plotted in Figure 14b and compared with the experimentally obtained exchange flow rate reported in [6]. The corresponding surface temperature variation is shown in Figure 14a. It is seen in Figure 14b that the results obtained from the simulation and the experiment are again very similar. However, the variation between the numerical and experimental results is also noticeable. Firstly, it is seen in Figure 14b that the numerically calculated maximum horizontal exchange flow rate is consistently higher than the experimental one. This may be attributed to the non-ideal adiabatic wall boundary conditions and the presence of a conductive surface in the experiment. Secondly, multiple peaks of the exchange flow rate appear in the numerical results during the cooling dominated phase, whereas they are not present in the experiment. The multiple peaks are indicative of high frequency fluctuations associated with the flow instability during the surface cooling phase. This variation between the experiment and simulation may be attributed to the significantly lower time resolution in the experiment (approximately 9.5×10^{-2} non-dimensional time) compared with the time resolution of 2.4×10^{-3} in the simulation. Similar behaviour of the exchange flow rate has been reported in the previous studies under periodic thermal forcing [14, 16].

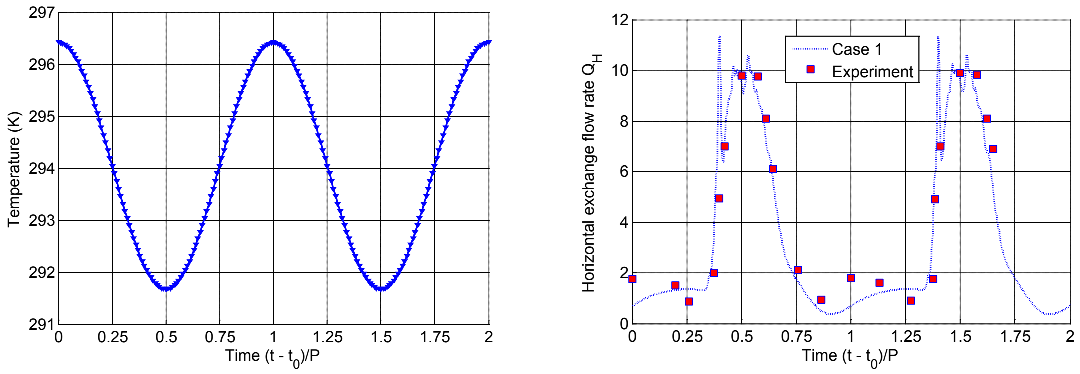

a) **b)**

Figure 14 a) Time series of the surface temperature for *Gr* = 3.52×10^4. b) Corresponding time histories of the horizontal volumetric exchange flow rates obtained from the simulation and experiment [6].

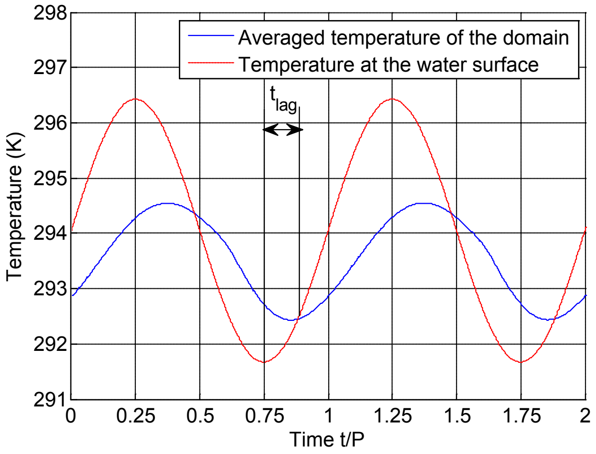

Figure 15 Time histories of the temperature at the water surface (red dashed line) and the averaged particle temperature across the domain (blue continuous line) for Case 1.

3.4.2.2 Time lag of the flow response to thermal forcing

The time lag of the flow response to the switch of the thermal forcing from heating to cooling or vice versa, which is an important feature under the effect of the cycling temperature [2, 6, 14, 16], is quantitatively compared between the experiment and simulation. In the experiment [6], the time lag of the flow response to the switch of the thermal forcing is reported to be around 11% of the thermal forcing period for the case corresponding to Case 1. The time lag (Δt) from the simulation is determined in Figure 15, which compares the time history of the average temperature in the cavity against that of the prescribed surface temperature. The time lag for Case 1 is calculated as 10.6% in Figure 15, which agrees very well with that reported in the experiment.

3.5 Effect of the Grashof number

In this section, the above described and validated numerical model is applied to examine the dependence of the flow response and its stability properties on the Grashof number. Altogether four Grashof numbers are investigated, and the detail of the calculated cases are given in Table 4. It is worth noting that the data presented below is extracted from the particle information after the flow has reached a quasi-steady state.

3.5.1 Onset time of instability over each thermal forcing cycle

As described above, flow instability in the form of plunging thermals occurs during the cooling phase of each thermal forcing cycle. The time when the instability starts to manifest, i.e. the onset time of the instability, is of interest. Since the instability originates from the cooling layer under the surface, the standard deviation of the particle velocity obtained from the surface thermal boundary layer is indicative of the presence of the instability, and thus may be used to predict the onset time of the instability. The time series of the standard deviation of the particle velocity calculated across a rectangular region in the surface layer (from the surface extending downwards to 0.01 below the surface) for all the four Grashof numbers are shown in Figure 16b, in which the onset time for each Grashof number is indicated by a vertical dashed line. It is clear in this figure that the onset time decreases with increasing Grashof number, confirming that the flow is more unstable at higher Grashof numbers.

Table 4 Detail of the computed numerical cases

Number of case	Grashof number	Prandtl number	Particle model
Case 1	3.52×10^4	6.82	Refer to Table 3
Case 4	2.66×10^4	6.82	The same as Case 1
Case 5	1.98×10^4	6.82	The same as Case 1
Case 6	5.53×10^3	6.82	The same as Case 1

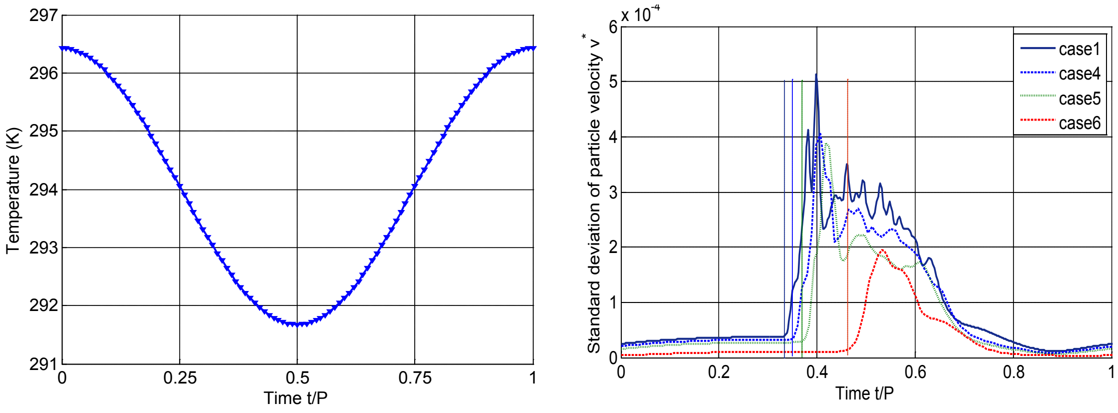

a) b)

Figure 16 a) A representative temperature variation at the water surface; b) The time series of the standard deviation of the particle velocity extracted across a rectangular region in the surface layer (from the surface extending downwards to 0.01 below the surface).

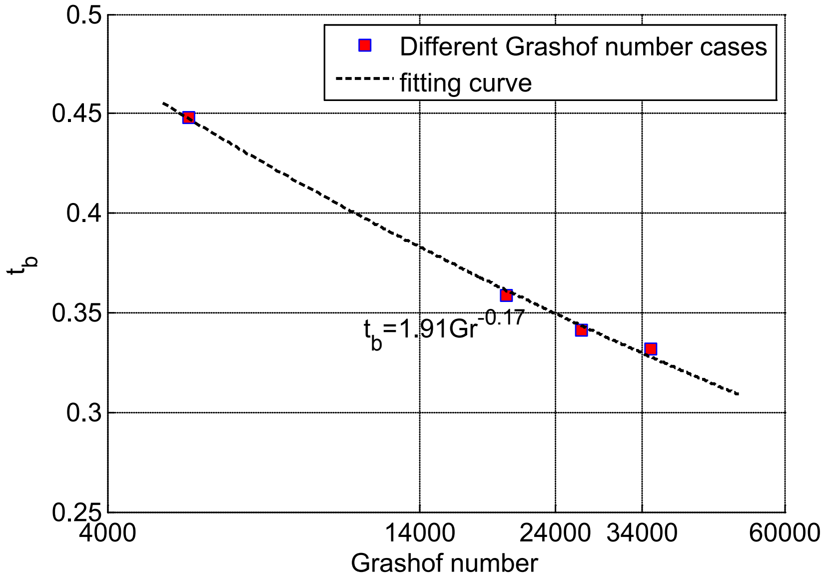

Figure 17 Dependence of the onset time of the instability on the Grashof number.

The dependence of the onset time of the instability on the Grashof number is shown in Figure 17. The correlation is given by (with an adjusted R-square of 0.99):

$$t_b = 1.91\,Gr^{-0.17} \tag{25}$$

Here the adjusted R-square instead of the standard R-square is quoted as it is considered to be a better indicator of the quality of curve fitting [78].

3.5.2 Wavenumbers resulting from the instability

As described above, a cellular flow structure forms when the instability occurs. Associated with the cellular structure, there is a dominant wavenumber, which is indicative of the number of cells forming in the domain and can be determined following the process described in Figure 13. The time histories of the dominant wavenumber over two thermal forcing cycles at the quasi-steady stage for all the four Grashof numbers are plotted in Figure 18b. Here, a non-zero wavenumber indicates the presence of flow instability, whereas a zero wavenumber means the flow is stable. It is seen in Figure 18b that, in general, the maximum wavenumber increases with the Grashof number.

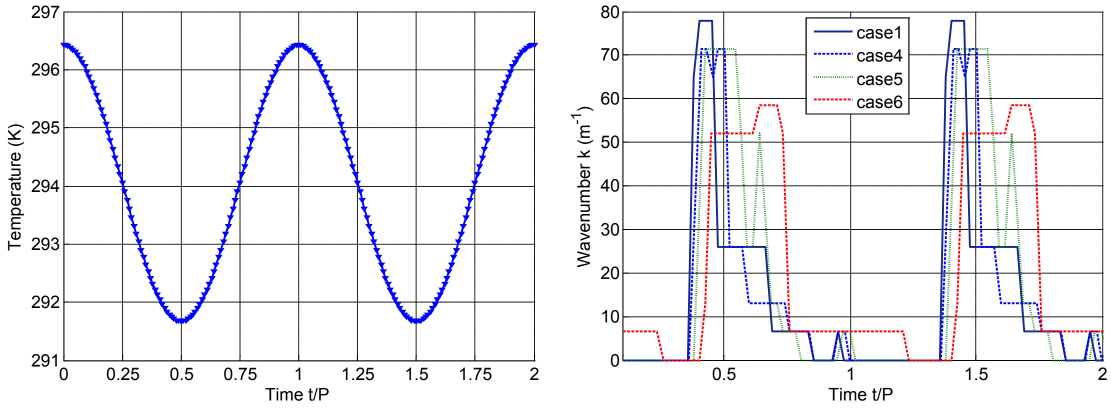

a) **b)**

Figure 18 a) A representative temperature variation at the water surface; b) The time series of the dominant wavenumber obtained for various Grashof numbers.

It is also seen in Figure 18b that the flow switches between stable and unstable phases over each thermal forcing cycle. The time duration of the unstable phase can be determined from Figure 18b, and the results are plotted in Figure 19. The empirical correlation between the time duration and the Grashof number is represented by Equation (26) below, with an adjusted R-square of 0.97:

$$t_{dt} = 216\, Gr^{-0.77} \tag{26}$$

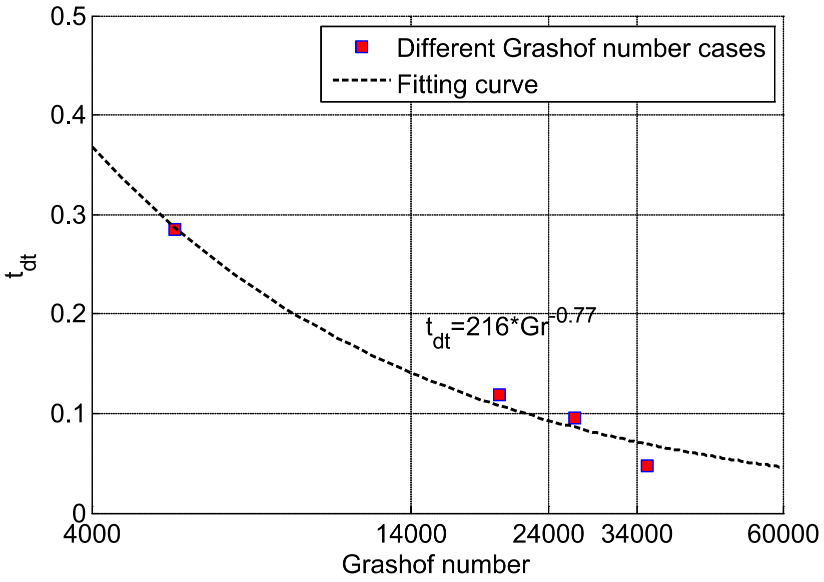

Figure 19 Variation of the time duration of the unstable phase (with the presence of instability) with the Grashof number.

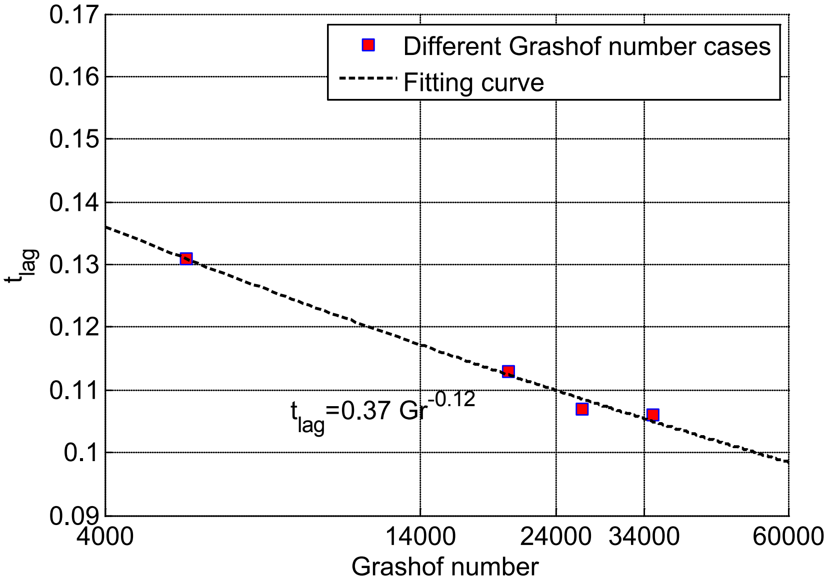

Figure 20 Time lag of the flow response versus the Grashof number.

3.5.3 Time lag of the flow response to the switch of the thermal forcing

As demonstrated in Section 3.4.2, the flow response in the reservoir model is not in phase with the thermal forcing at the surface, and there is a clear time lag between the flow response and the switch of the thermal forcing between heating and cooling. The dependence of the time lag on the Grashof number is plotted in Figure 20. Clearly the time lag decreases with the increase of the Grashof number, which means the flow responds to the switch of thermal forcing more quickly at higher Grashof numbers. The correlation between the time lag of the flow response and the Grashof number is obtained from Figure 20 as (with an adjusted R-square of 0.99):

$$t_{lag} = 0.37\ Gr^{-0.12} \tag{27}$$

3.6 Conclusions

In this study, a finite-volume based flow solver coupled with a Discrete Phase Model has been adopted to reproduce the concurrent PIT/PIV experiment of the flow response in a reservoir model to periodic thermal forcing [6]. Both qualitative and quantitative data have shown good agreement between the numerical simulation and the previous experiment. The validated numerical model is used to extend the investigation over a range of Grashof numbers. The focus of the investigation is on the dependence of the flow and its stability properties on the Grashof number. It is found that all of the onset time of the flow instability, the time duration of the unstable phase, and the time lag of the flow response to the switch of the thermal forcing decrease with the increase of the Grashof number, suggesting that the flow is more unstable and responsive at high Grashof numbers.

The study presented in this chapter involves visualising and measuring the temperature and velocity fields of the thermal flow using the particle information. This is similar to the processes adopted in the concurrent PIT/PIV experiment using TLC particles [6]. The results from the numerical simulation is validated against the TLC experiment in terms of the temperature and velocity structures, the horizontal exchange flow rate, and the time lag of the flow response to the switch of the thermal forcing. The good agreement between the simulation and experiment demonstrates the feasibility of numerically tracking particles within fluids under the effect of unsteady thermal forcing.

4. Transport of pollutant particles in a reservoir due to diurnal temperature variation

4.1 Introduction

In this chapter, a numerical study is carried out to examine particle transport in the reservoir in a pseudo real-life scenario, in which pollutant or nutrient particles are injected into the sidearm of the reservoir.

The presence of pollutants or nutrients in reservoirs or lakes can have a negative impact on the quality of the stored water. One of the potential severe consequences is the blooming of cyanobacteria in the storages. Not only does the blooming disrupt the normal ecosystem of the water body, but also the microcystin released from the cyanobacteria is a threat to public health and raises concerns in the management of drinking water supply systems. A high concentration of nutrients is usually associated with this hazard. Understanding the deposition and dispersion behaviour of pollutant or nutrient particles is essential for developing an understanding of the causes of the hazard.

In general particles suspending in a fluid are transported by the flow, either passively, in which case the particles simply follow the flow and have no other interaction, or actively, in which case the particles may have a degree of self-determination, for example their buoyancy, and may interact with the flow. One such flow is natural convection, driven by buoyancy forces resulting from temperature gradients (e.g. [2, 6, 14]).

In natural water bodies these particles are usually introduced in the near-shore region, either from local runoff or stream inflow. Previous studies have demonstrated that the specific flow patterns induced by natural convection under the effect of different types of diurnal thermal forcing (e.g. [2, 6, 14, 16]) are an important transport mechanism in the near-shore region of reservoirs. Lei and Patterson [14] performed a numerical simulation, which considered both the radiation flux through the surface and the excess radiation re-emitted from the bottom. Bednarz et al [6, 16] examined the diurnal flow response to a periodic surface temperature. In all of the studies of the diurnal thermal forcing cases (e.g. [2, 6, 14, 16]), a distinct instability in the form of plunging plumes from the surface occurs during the cooling phase. During the radiation heating phase, the re-emission of residual radiation from the bottom generates rising plumes from the bottom. In addition, in the near-shore region, the presence of the sloping bottom results in a lateral temperature gradient with warmer water in the shallow part during the heating phase, and cooler water in the shallow part during the cooling phase. This generates a circulation out along the surface during heating, or a plunging flow along the slope during cooling [2, 7, 20].

Numerical studies of particle transport in fluids have been reported extensively. Among these, Guha [11] reviewed the particle transport mechanisms in laminar and turbulent flow regimes respectively under both the Eulerian-Eulerian and Eulerian-Lagrangian frameworks in CFD models, and confirmed the importance of the fluid and particle properties that characterise the particle transport model. Studies of particle motion induced by natural convection have also been reported. For example, Akbar et al. [12] numerically examined particle deposition and dispersion behaviour in fluids within a square cavity under natural convection. Puragliesi et al. [79] and Pallares and Grau [61] discussed the effect of particle properties on particle motion in fluid flows in either a square cavity or an infinite channel subject to differential heating. Direct comparisons of the particle deposition rates under various types of thermal forcing imposed on the boundaries were carried out using different relaxation times which characterise the particle sizes and densities [61, 79]. Although most of the existing studies have addressed the extent to which both the fluid flows and the particle properties affect the particle transport in fluids, few studies have quantified the dependence of particle deposition and dispersion on the induced fluid flows under natural convection.

In the present study, the particle transport in a reservoir model under a cycling temperature imposed at the water surface is numerically simulated using the finite volume CFD code ANSYS FLUENT 13 coupled with a built-in Discrete Phase Model under the Eulerian-Lagrangian framework. The purpose of the study is to quantify the dependence of the particle transport, including their deposition and dispersion behaviour, on particle properties and the diurnal thermal forcing.

The organisation of the rest of this chapter is as follows:

In Section 4.2, a two-dimensional reservoir model is formulated. The specific numerical parameters for the fluid flow and particle motion relevant to the present investigation are discussed.

In Section 4.3, the grid and time-step dependency tests are described.

In Section 4.4, the numerical results are described in terms of the temporal evolution of the particle motion, the effect of the particles' properties and fluid flow on the particle motion, and the dependence of the particle deposition and dispersion behaviour on the Grashof number.

In Section 4.5, a case study based on a recent environmental event of algal blooming in Lake Burragorang near Sydney is discussed in relation to the present numerical results.

The chapter ends with Section 4.6 which summaries the major results of the present investigation.

4.2 Numerical details

Fluid flow model formulation

A two-dimensional (2D) reservoir model described in Chapter 2 is considered here (refer to Figure 21). The dimensions shown in Figure 21 are all normalised by the maximum water depth. The tip of the model is cut off at $x = 0.16$ in order to avoid a singularity in the numerical simulation, and an extra vertical wall is added at that location.

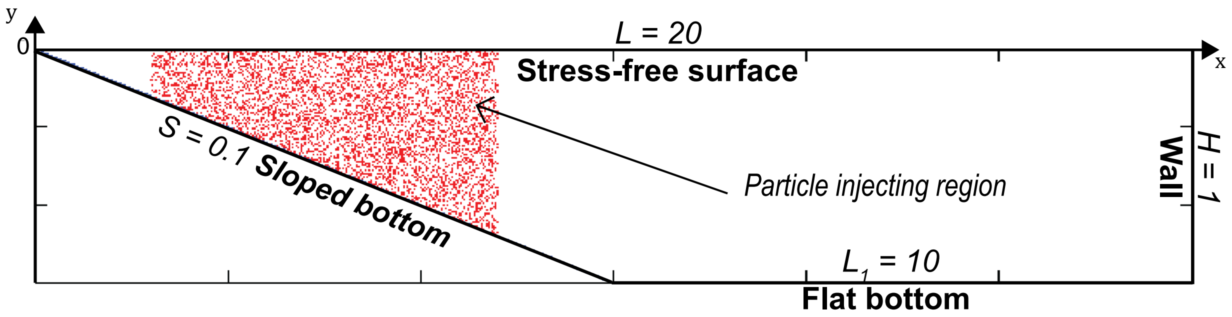

Figure 21 Schematic of the numerical model (not to scale).

In a real-life reservoir, pollutant or nutrient particles usually enter into reservoirs through sidearms (corresponding to the sloped bottom region) and are carried around within the water bodies by various processes. In this study, particle dispersion by natural convection in the near-shore region, which is known as an important mechanism in the absence of wind and stream inflow effects, is investigated. In the numerical model, the surface is assumed to be stress-free and all the endwalls and bottoms are assumed to be rigid and no-slip. In order to simulate the effect of the diurnal temperature variation, a standard sinusoidal function of the temperature (refer to Equation (15)) is specified at the water surface. Here, the forcing excludes heating by solar radiation, so is relevant to periods of low solar insolation. Apart from the water surface which has a prescribed temperature variation, all the other boundaries are adiabatic, as is described in Chapter 2. The water body within the computational domain is assumed to be initially stationary with a uniform temperature T_0.

The flow in the reservoir model is assumed to be laminar and two-dimensional within the parameter ranges considered here. The fluid flow motion and temperature change within the reservoir model are governed by the usual Navier-Stokes and energy equations with Boussinesq assumption [66] (refer to Equations (16) in Chapter 2).

Particle model formulation

Particles are injected at the specific location of interest within the tip region, as shown in Figure 21. The quantity of the injected particles is measured by the volume fraction, which is the ratio of the total volume of the particles to the total volume of the surrounding flow domain (referred to as volume fraction of particles hereinafter). The close vicinity of the tip region is excluded from the particle injection because particles injected at that location are unlikely to be carried around by the flow due to the extremely weak flow associated with the dominance of heat conduction in that region [7, 18]. Any particles injected into this region will mainly be affected by gravitational settling and therefore are of little interest. To avoid the start-up effect of the diurnal flow, the particles are injected at the beginning of the third diurnal cycle after the fluid flow has reached a quasi-steady state. The injection of particles is once only and the specific locations of each injected particle are subject to a random distribution. The initial particle distribution is shown in Figure 21, which appears to be approximately uniform but is randomly distributed across the region of injection.

In the present DPM, the ‘reflect’ wall boundary condition for particles is only assumed at the water surface. It is assumed that the fluid surface tension is sufficiently large for the bouncing process to occur (e.g. in [80]). The detail of the ‘reflect’ wall boundary condition can be found in Chapter 2. Apart from the water surface which has a ‘reflect’ wall boundary condition, all the endwalls and bottoms of the model have a ‘trap’ wall boundary condition, which has been discussed in Chapter 2.

The governing equations of particle motion are determined by the motion of fluid flows, buoyancy and other minor forces applicable to the particles, as discussed in Equation (1) of Chapter 1. In the numerical simulations here, two additional minor forces, i.e. Brownian dispersion and lift forces, will be included.

Since the present study is relevant to reservoirs with water as the fluid medium, the Prandtl number is fixed at 6.82. The numerical simulations are based on a laboratory scaled model which was adopted in [6]. Accordingly, the geometry parameters are fixed at $A = 0.05$ and $S = 0.1$ respectively; and the normalised thermal forcing period is set to $P^* = 0.54$. Two particle relaxation times characterising the particle properties, including their density and size are considered in this study, with normalised values of 3.63×10^{-9} and 1.45×10^{-8} corresponding to $10\ \mu\mathrm{m}$ and $20\ \mu\mathrm{m}$ particle diameters respectively with particle density fixed at $1.0 \times 10^{3}\ \mathrm{kg/m^{3}}$ (very close to the density of water). The maximum volume fraction of the particles at the time of injection is 3.49×10^{-4}, which is sufficiently small to justify the adoption of the Euler-Lagrangian approach. The Grashof number Gr, which characterises the maximum temperature variation, is varied from 5.53×10^{3} to 1.77×10^{5} in this study, and laminar flow is expected over this Grashof number range (refer to [18]).

4.3 Grid and time-step dependency tests

No specific grid and time-step dependency test is conducted for the present investigation as the problem to be investigated here is very similar to that described in the previous chapter with only minor variations. Therefore, the selection of the mesh and time-step follows the dependency tests described in Section 3.3.1. Based on those tests, the medium grid system (with 861×51 mesh and the corresponding time-step 1.46×10^{-6}) is adopted for the subsequent simulations.

4.4 Results

In this section, the particle transport under the effect of the periodic thermal forcing is simulated based on the model described in Section 4.2 above. Several cases with different Grashof numbers and different particle properties, as shown in Table 5, are calculated. In what follows, the temporal evolution of particle motion under the diurnal thermal forcing will be described based on the result from Case 3a. Then the results from Cases 3a, 3b and 4 will be examined to demonstrate the effects of both the particle properties and the fluid flow on particle motion. Finally, the particle deposition and dispersion behaviour over a wide range of Grashof numbers will be examined.

4.4.1 Temporal evolution of particle motion

4.4.1.1 Particle concentration contours

The particle motion and flow development under the prescribed diurnal thermal forcing is described based on the particle concentration contours overlaid by the contours of stream functions (referred to as particle concentration contours hereinafter). A typical case (Case 3a in Table 5) with a medium Grashof number is chosen for this purpose, and the results are shown in Figure 22. Other cases are found to show similar evolution of the fluid flow and particle motion. In this and all subsequent figures, the time t = 0 corresponds to the time when the particles are injected into the domain.

Table 5 Parameters of the numerical cases

Cases	Maximum volume fraction of particles	Normalized particle relaxation time	Prandtl number	Grashof number
1	3.49×10^{-4}	3.63×10^{-9}	6.82	5.53×10^{3}
2	3.49×10^{-4}	3.63×10^{-9}	6.82	7.38×10^{3}
3a	3.49×10^{-4}	3.63×10^{-9}	6.82	4.43×10^{4}
3b	3.49×10^{-4}	1.45×10^{-8}	6.82	4.43×10^{4}
4	3.49×10^{-4}	3.63×10^{-9}	6.82	8.85×10^{4}
5	3.49×10^{-4}	3.63×10^{-9}	6.82	1.18×10^{5}
6	3.49×10^{-4}	3.63×10^{-9}	6.82	1.77×10^{5}

For all the cases considered in this study, particles are injected randomly over the full local depth and over the horizontal range $2 \leq x^* \leq 8$. The contours of the fluid flow are shown in Figure 22, together with the contours of the particle concentration, the level of which is indicated by the colourmap underneath the contour plots (the particle concentration is measured by the particle number per unit area). The purpose of the overlayed contours of stream functions is to indicate the flow patterns at different stages of the transient flow, and thus the actual values of the stream functions are not shown here. At $t = 0$ (Figure 22a), the heating phase has just commenced, and the streamlines show a dual cell pattern, with a clockwise weak circulation in the tip region resulting from the commencement of heating, and a larger scale anticlockwise circulation in the body of the reservoir, which is the residual circulation from the previous cooling phase. The particle concentration is uniform over the specified region. At $t = P/4$, (Figure 22b) the heating is at its peak; the residual cooling phase circulation has vanished and the clockwise circulation due to heating is distinct. The distribution of the particles has distorted as the flow carries the particles along the surface, and back up the slope. Note that the particle boundary at the tip end is undistorted, as there is little or no flow at that location. The heating cycle ends at $t = P/2$ (Figure 22c) and two features are immediately evident. First, during the later part of the heating cycle, although still under heating, the applied surface temperature has become less than the actual temperature at the water surface, so relative cooling occurs, resulting in the formation of plunging plumes at the shallow end. These are manifested as small scale circulations, and some weak distortion of the boundary of the particle-occupied region. However the main clockwise circulation persists, and particles continue to be carried out along the surface. Second, particle free fluid has also been carried up the slope by the return flow, overlaying some residual particles close to the bottom. At $t = 3P/4$ (Figure 22d) cooling is at the peak, and flow is dominated by multiple sinking plumes over the full domain. An anticlockwise circulation is only weakly present in the shelving region. The particle distribution reflects the active mixing inherent in the presence of the plumes, with patchiness present in the deeper regions. The distortion of the particle distribution is however still minor in the tip region. After a full thermal forcing cycle at $t = P$ (Figure 22e), the cooling period has ended, and a weak positive circulation has begun in the tip region. The primary circulation is still anticlockwise from the surface cooling, but no plunging plumes are present. The flow is the same as that at $t = 0$ since the flow is now quasi steady. The patchiness in the deeper part of the domain remains, but again there has been little effect on the tip boundary of the particle distribution.

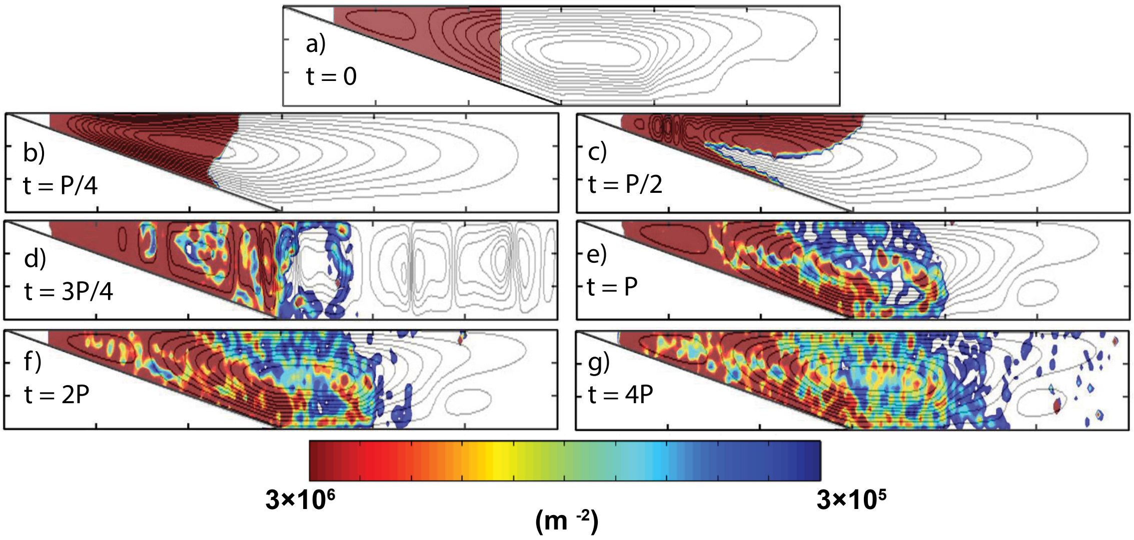

Figure 22 Temporal evolution of the particle concentration contours overlayed by the contours of stream functions. The results are shown for Case 3a.

This pattern persists over further cycles. For example, at $t = 2P$ (Figure 22f) and $t = 4P$ (Figure 22g), the flow is identical and the particle distributions are little changed. Again, the distribution of particles at the tip end is virtually unchanged. The same result is evident after many cycles.

This sequence of images demonstrates that although the flow is quasi-steady, the particle distribution becomes extremely patchy in the deeper part after a single cycle of cooling, as the result of the mixing by the plunging surface plumes. However, the region near the tip is still virtually unchanged since the flow in this region is not significant.

4.4.1.2 Particle source distribution contours

As noted above, it is evident that the particles near the tip do not move significantly over several cycles, due to the weak flow present there. To confirm this, the initial distribution of particles is coded by colour in four bands according to their source locations, moving from the tip out towards the main body of the reservoir. The initial distribution is shown in Figure 23a below. The particles retain their initial colours in the subsequent motion, and the colour in the contours then demonstrates their subsequent positions. A sequence of times through the first cycle (Figure 23b-e) again demonstrates the mixing that occurs, with the deeper region comprising components of all colours after the first cycle, except those at the very tip end. Figure 23e demonstrates that the particles at the tip end are largely unmoved, consistent with the observations above. Even after 5 cycles (Figure 23f) there are still remnants of the original particles in the tip region. These particles require a very long timescale to be incorporated into the main body of the reservoir.

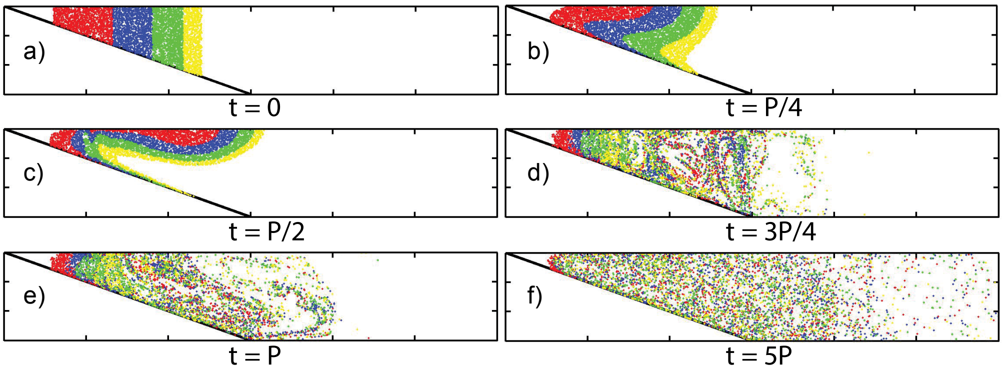

Figure 23 Temporal evolution of the contours of the particle source distribution. The results are shown for Case 3a.

4.4.2 Effect of particle properties and fluid flow on particle motion

The effects of the particle properties and fluid flow on particle motion are investigated using the cases with different particle relaxation times and different Grashof numbers (i.e. Cases 3a-b and 4). The focus here is on the detail of the particle motion in various regions of the reservoir model. Some analytical and statistical data relevant to the particle transport are presented and discussed below.

4.4.2.1 Particle flux

The horizontal particle flux between the sloped-bottom region and the uniform-depth region indicates the particle dispersion rate within the domain and the transport of particles from the shallow to deep region under the effect of the thermal forcing, and may have implications for water quality. The particle flux across the vertical line of the domain where the sloped-bottom region joins the uniform-depth region is calculated as:

$$q_H = \int_{-H}^{0} u_{px} \frac{\partial C_{pt}}{\partial x} dy \tag{28}$$

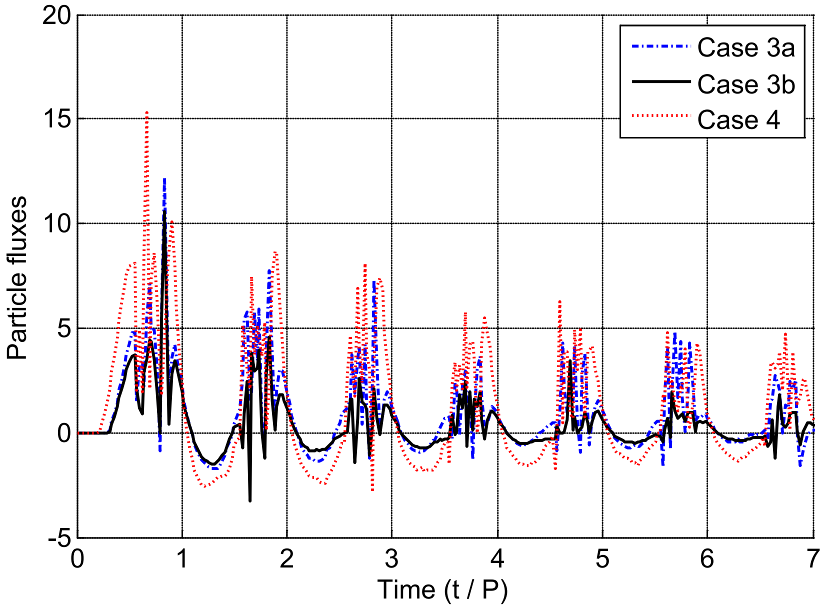

Figure 24 Time series of the horizontal particle flux obtained from the middle of the domain where the sloped bottom joint to the flat bottom.

Figure 24 shows the time series of the horizontal particle fluxes for the three cases under consideration (Case 3a-b and 4). Here, the flux of the particles is normalised by $\sim C_0 \kappa / H$.

It is worth noting that in Figure 24 the calculated horizontal particle flux fluctuates strongly when it is positive, corresponding to the cooling phase of the thermal forcing cycle. The fluctuation is a result of the thermal instability during the cooling phase and is consistent with the observed fluctuation of the exchange flow rate between the two regions as reported in [6, 14, 81]. Further, it is clear from the figure that in the initial few cycles there is a net transport from the sloped-bottom region to the uniform-depth region, and that the net flux is gradually reducing over time. Since the particles are getting more evenly distributed across the two distinct regions as discussed above, after a sufficiently long time the net horizontal particle flux over a cycle is expected to be close to zero.

It is also clear in Figure 24 that the horizontal particle flux in the case with the higher Grashof number (Case 4) is greater than that for the other two cases, whereas the horizontal fluxes for the two cases with the same Grashof number but different particle relaxation times (i.e. Cases 3a and 3b) show a similar behaviour. This indicates that the Grashof number plays a dominant role in determining the particle dispersing motion. The effect of the Grashof number on particle transport will be further examined in Section 4.4.3 below.

4.4.2.2 Particle distribution in the deep region

The time evolution of the particle distribution in the uniform-depth region is shown in Figure 25 and Figure 26 for Cases 3a, 3b and 4. Here the uniform-depth region is equally subdivided into multiple horizontal layers (refer to Figure 25a) or vertical sections (refer to Figure 26a), and the time series of the particle fraction in each layer or section are plotted.

In Figure 25b, a typical time series of the fraction of the remaining particles in Layer 1 (refer to Figure 25a) relative to the total injected particle number is shown for Case 3a. It is seen in this figure that initially the particle fraction is zero, indicating that there are no particles in this layer, which is expected. Over the 12 cycles from the injection of the particles, the particle fraction increases gradually with time and approaches a relatively constant level after about 10 cycles. Furthermore, both large-scale and small-scale fluctuations of the calculated particle fraction are evident in Figure 25b. The large-scale fluctuation is associated with the switch of the thermal forcing between heating and cooling, which causes the large-scale circulation within the flow domain to reverse. The small-scale fluctuation is associated with the thermal instability in the form of plunging thermals during the cooling phase. The result shown in Figure 25b is consistent with the observations described above. The time series of the particle fractions in other layers and sections all show similar features to that of Layer 1 plotted in Figure 25b. For the convenience of comparing the relative particle fractions in different layers, a moving averaged particle fraction over three thermal cycles is calculated to smooth the time series. The effect of the moving average is illustrated in Figure 25b, which compares the moving averaged particle fraction against the raw data. Since the moving average is calculated over three thermal cycles, the data is plotted from $t/P = 3$ only (i.e. three cycles after the injection of particles). In what follows, the moving averaged particle fractions in different layers are compared for the three different cases considered here.

Figure 25c-e shows the time series of the particle fraction in each horizontal layer for Cases 3a, 3b and 4 respectively. For all the three cases shown in these figures, it is clear that initially more particles tend to stay in the lower layers of the uniform-depth region. This is attributed to the stronger anticlockwise circulation along the sloped bottom as well as the gravitational settling of the particles. The particles are carried around from the tip region in the direction of the slope, entering towards the deeper layers of the uniform-depth region by the stronger anticlockwise circulation during cooling, which is indicated by the net horizontal particle flux shown in Figure 24. The effect of the gravity also tends to drive the particles downward to the lower layers of the region. With increasing time, the variations of the particle fraction among the different layers diminish as a result of both the particle mixing in the local water column due to the flow instability described above and the particle deposition because of gravitational settling across the domain. These two processes increase the vertical transfer rate of the particles between the different layers, and the settling process also reduces the overall quantity of the particles remaining in water. As a consequence, the particle distribution becomes more uniform across the deep region.

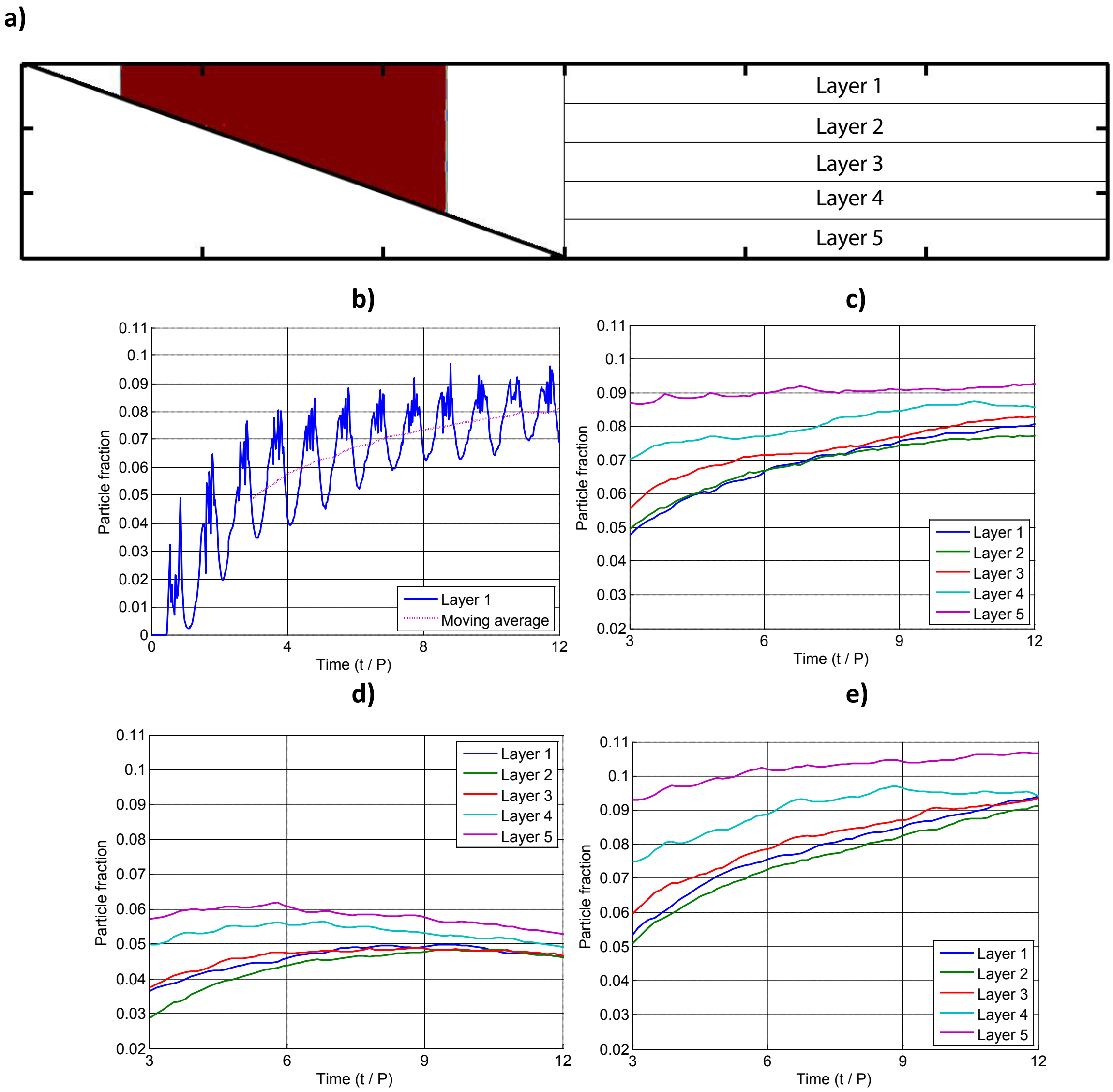

Figure 25 a) Sampling locations of the horizontal layers. b) Time series of the fraction of the remaining particle number in Layer 1. Both the raw data and the moving averaged data are plotted for Case 3a. c)-e) Time series of the moving averaged particle fractions in the different layers: c) Case 3a; d) Case 3b; e) Case 4.

The variations among the three cases shown in Figure 25c-e are worth noting. Compared with Case 3a, Case 4 shows a relatively higher fraction of the particles in the uniform depth region as a result of a stronger flow; whereas the result from Case 3b shows a relatively lower particle fraction in the domain because of the sedimentation resulting from the relatively larger relaxation time of the particles. In addition, a clearly higher growth rate of the particle fraction in all the layers at the earlier stage can be observed for Case 4 in comparison with the other two cases (see Figure 25c-e), suggesting that the particle dispersion is more intense for the case with the higher Grashof number. These results are all expected and the general behaviour of the particle motion observed here is consistent with that reported in the literature (i.e. [12, 61]).

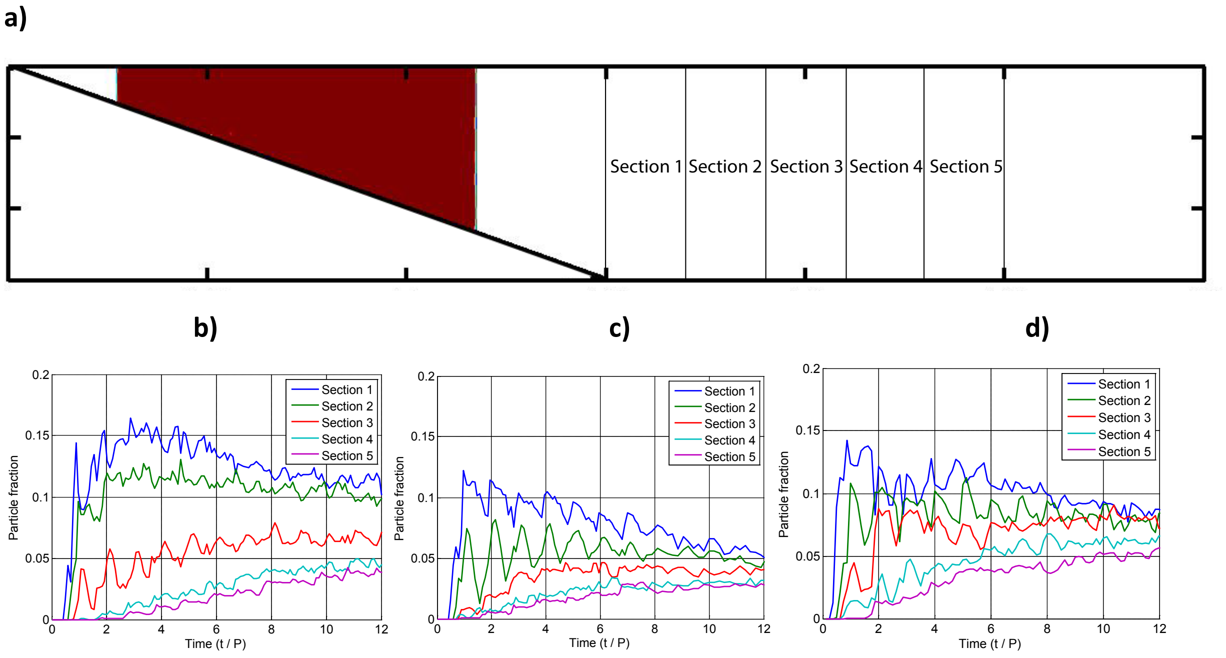

Figure 26 a) Sampling location of the vertical sections. b)-d) Time series of the particle fractions in the different sections: b) Case 3a; c) Case 3b; d) Case 4.

Figure 26b-d shows the time series of the particle fraction in each vertical section for the three cases considered here. It is worth noting that the data plotted here is the raw data without moving averaging. It is expected that the particles will sequentially enter each section from Section 1 to Section 5 for all the cases, which is confirmed in this figure. Although the time evolutions of the particle fraction are fluctuating under the effects of both the large-scale circulation induced by the cycling temperature at the water surface and the occurrence of the instability during cooling, the relative distributions of the particles in each section can be identified from the figures for each case. The observation in Figure 26 suggests that initially the fraction of the particles increases sequentially from Section 1 to 5. As time increases, the differences in the particle fraction among the different sections reduce, which means that the distribution of the particles becomes more uniform.

It is also seen in Figure 26b-d that, with the higher Grashof number (Case 4) which enhances the horizontal convection, and the larger relaxation time (Case 3b), which enhances the particle deposition, the variations of the particle concentrations among the different sections become less significant with increasing time. With increased deposition the overall fraction of the particles remaining in the deep region also reduces, as shown by Case 3b compared with Case 3a. This is consistent with the particle distribution across the different horizontal layers discussed above.

4.4.3 Effect of the Grashof number on particle transport

The results shown above have demonstrated that both the fluid flow and the particle properties have significant impact on the particle transport. In this section the impact of the fluid flow only on particle transport is further examined. The reasons for focusing on the impact of the fluid flow only are two-fold: firstly, the impact of the fluid flow as an external effect on particle motion is of the most concern in environmental engineering since it is an input variable to the system. Secondly, for the investigated cases the flow determines the overall particle motion including their deposition and dispersion, whereas the particle properties primarily affect the particle suspension. Here we consider the cases with different Grashof numbers but with the particle relaxation time fixed at 3.63×10^{-9} (refer to Cases 1-3a and 4-6 listed in Table 5).

4.4.3.1 Particle deposition behaviour with varying Grashof numbers

The residence time of the particles is evaluated in this section. Particle deposition is important in determining the fate of the particles and consequently the quality of the stored water. In the numerical simulation, the particles are only removed from the computational domain following deposition, which can be indicated by the time series of the ratio of the remaining particle number to the initially injected particle number in the whole computational domain – referred to as the residual particle fraction as shown in Figure 27. A clear tendency shown in Figure 27 is that the number of the residual particles in the flow domain decreases with time in all the cases. The figure also shows that the deposition rate of the particles decreases with the increasing Grashof number. This is the result of the relatively stronger flow at the higher Grashof numbers, which incurs a larger drag force to carry particles around. This observation is generally consistent with the literature (e.g. [12, 61, 77]).

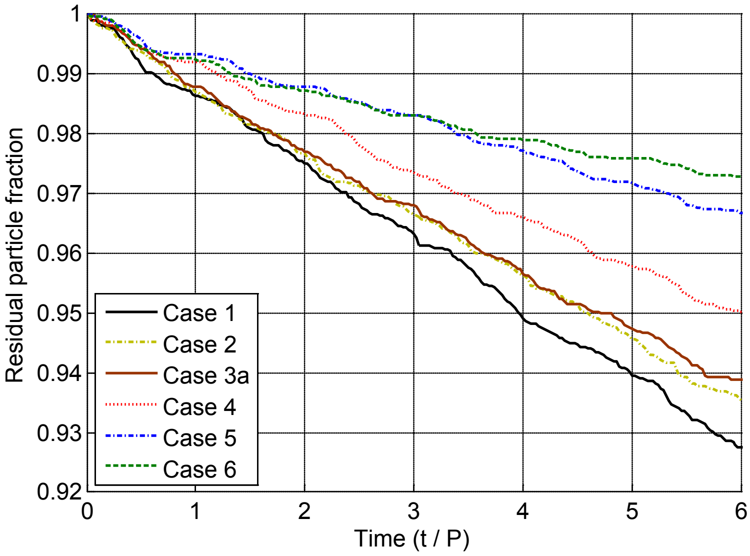

Figure 27 Time series of the residual particle fraction in the whole computational domain.

An exponential decay function in the following form can be fitted to each of the curves shown in Figure 27:

$$f(t) = \eta_0 e^{-\frac{t}{\varphi}} \tag{29}$$

where $f(t)$ is the residual particle fraction within the flow domain, η_0 is the initial particle fraction, which is 1 for all the cases, and φ is referred to as the mean residence time of the particles. Whilst other functions such as a linear function may also be used to fit each of the curves in Figure 27, the exponential function is chosen here since it has been tested to provide the best quality of curve fitting in terms of the adjusted R-square (0.97 for the linear curve fitting vs. 0.99 for the exponential curve fitting, as obtained for Case 1). The adjusted R-square values of the exponential curve fitting are shown in Table 6 below.

Table 6 Quality of the exponential curve fitting for the time series shown in Figure 27

Case numbers	1	2	3a	4	5	6
Adjusted R^2	0.99	0.99	0.99	0.99	0.99	0.99

The mean residence times normalised by the period P of the thermal forcing cycle obtained for all the cases are shown in Figure 28. The results clearly show that the mean residence time increases with the increasing Grashof number. An empirical correlation quantifying the effect of the Grashof number on the normalised mean residence time of particles is given as follows (with the adjusted R-square of 0.99):

$$t_{all} = 85.27e^{6.3\times10^{-6}\,Gr} \tag{30}$$

The above correlation indicates that the increase of the drag force on particles as a result of the more intensive fluid flow at the high Grashof numbers undermines the effect of gravitational settling on particle motion. In that sense, the particle deposition behaviour becomes less significant at the higher Grashof numbers; therefore, the deposition of the particles reduces with the increasing Grashof number. A similar scenario is also discussed in [79].

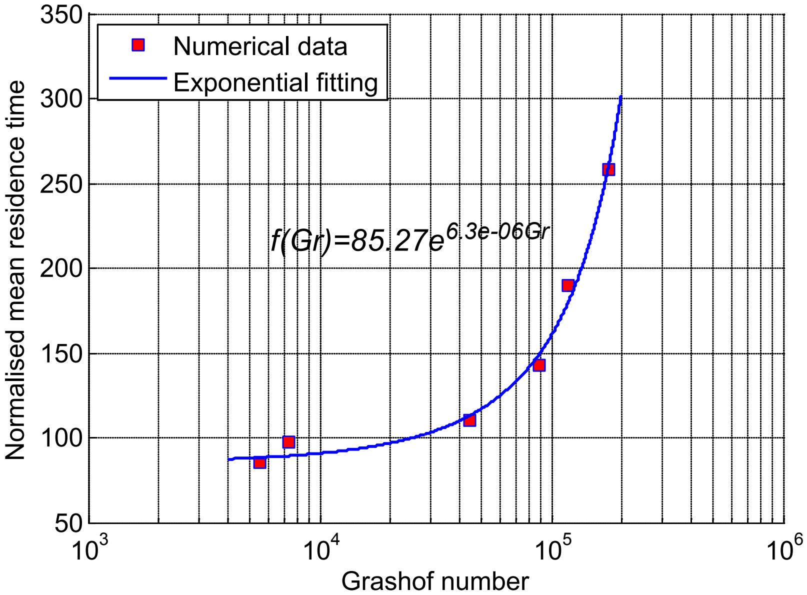

Figure 28 Normalised mean residence time of particles in the whole domain vs. the Grashof number.

4.4.3.2 Dependence of particle dispersion on the Grashof number

The dispersion of particles across the reservoir, which mainly depends on the horizontal velocity of the particles, is also of interest from the water quality point of view. Here we focus mainly on the dispersion of particles in the entire tip region of the reservoir model. The ratio of the remaining particle number across the entire tip region to the initial injected particle number in the entire computational domain is calculated to indicate the behaviour of particle dispersion from the shallow to the deep region. Accordingly, the residence time of the particles in the tip region can be derived.

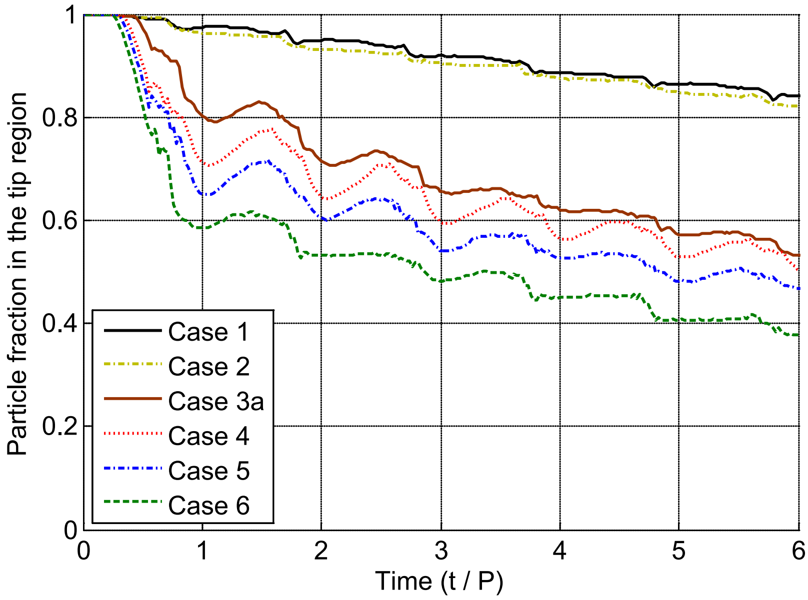

Figure 29 Time series of the ratio of the remaining particle number within the tip region to the initial injected particle number in the entire computational domain.

The time series of the particle fraction in the tip region for all the cases are plotted in Figure 29. As expected the particle fraction in the tip region decreases with increasing time as a result of particle dispersion. It is interesting to note that the particle fraction fluctuates with time. This is caused by the reversing circulations in the reservoir induced by the cyclic thermal forcing at the water surface. The oscillation is dying out after a few cycles because of the tendency of having a uniform particle distribution as described in Section 4.4.1 above. Among all the cases shown in Figure 29, the particle fraction decreases more sharply and oscillates more strongly for the cases with the higher Grashof numbers (i.e. Cases 3-6) than that with the lower Grashof numbers (i.e. Cases 1 and 2). This is a result of the more intensive fluid flow at the higher Grashof numbers, which enhances the particles' suspension capacity.

Table 7 Quality of the exponential curve fitting for the time series shown in Figure 29

Case numbers	1	2	3a	4	5	6
Adjusted R^2	0.99	0.99	0.93	0.83	0.80	0.83

The mean residence times of the particles in the tip region are derived based on the time series plotted in Figure 29. The curve fitting of each case follows the same process as that described in Section 4.4.3.1 using an exponential function. The quality of the exponential curve fitting is indicated by the adjusted R-square values shown in Table 7. The calculated mean residence time of the particles are plotted in Figure 30.

Similarly, an empirical correlation characterising the dependence of the normalised particle residence time in the entire tip region on the Grashof number is obtained as follows (with an adjusted R-square of 0.99):

$$t_{tip} = 2419\, Gr^{-\frac{1}{2}} \tag{31}$$

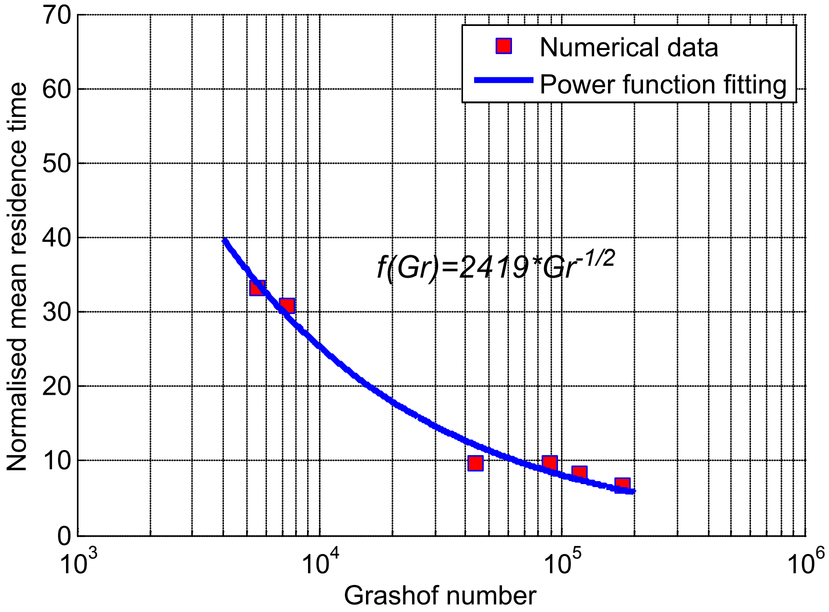

Figure 30 Normalised mean residence time of particles in the entire tip region vs. the Grashof number.

The above correlation shows that the residence time of the particles in the tip region decreases and thus the dispersion of the particles increases with the increasing Grashof number.

4.5 Discussion

The results from the above-described cases under the diurnal thermal forcing can be summarised as follows: firstly, the particle deposition rate becomes significant with decreasing Grashof number; secondly, the particle dispersion reduces with decreasing

Grashof number. Provided that the other parameters are all fixed in a natural water body, the Grashof number is determined by the variation between the maximum and minimum temperatures within a diurnal thermal forcing cycle. In that sense, a monthly mean Grashof number may be obtained from the monthly averaged variation of diurnal temperature.

The natural convection flow induced in the near-shore region by the fluctuating surface temperature is one of the important transport mechanisms among those, for example, rainfall, influent, and surface wind etc. operating in reservoirs. Although particle transport under natural convection may not be as significant as the other mechanisms, it plays an important role under calm conditions when there is little effect of the other transport mechanisms (e.g. in a drought when inflows are minimal and during a less windy period). An example can be found with algal blooming which occurred in Lake Burragorang (near Warragamba dam), New South Wales, Australia between 2007 and 2008 (reported in e.g. [82]). According to [83], an algal bloom occurs under the effect of several external conditions, including excessive nutrients (e.g. phosphate compounds) accumulating in the sediments as the bacteria's food storage and a stable living environment without intensive flows. The first of these factors is related to the deposition of particles carrying the nutrients, and the second to the decreased horizontal transport. Further, algal blooms tend to occur from near shore regions.

In periods of low wind, it may be expected that the transport mechanism described above will be a significant contributor to the dispersion and deposition of particles (and thus nutrients) in natural water bodies. Further, as has been observed in the investigation described above, the region in the vicinity of the tip end is essentially stagnant for a significantly long period.

A significant rainfall deficiency occurred during the summer of 2007 across New South Wales, Australia, which caused a severe drought [84]. In addition, the estimated strength of the wind force indicated by the speed of wind during the summer of 2007 – 2008 was significantly lower than other years in the nearby regions of Lake Burragorang. The recorded averaged wind speed data over the summer periods at two weather stations located within 10 km from Warragamba Dam are shown in Figure 31, confirming that the wind effect for the summer of 2007-2008 was significantly weaker than in other years.

Further, Figure 32 plots the averaged variation of the daily temperature over the same summer periods of 2004-2009 based on the data recorded at the same weather stations.

Clearly the average daily temperature variation over the five consecutive months during the summer period of 2007 – 2008 is also significantly lower than that in the other years.

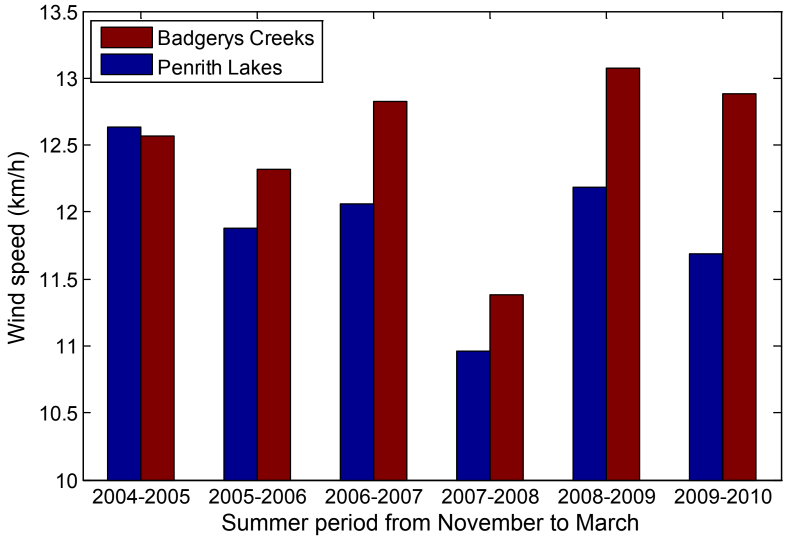

Figure 31 Average wind speed during summer from 2004 to 2009 obtained at the stations in Badgerys Creek (Station No #067108) and Penrith Lakes (Station No #067113). Source: Bureau of Meteorology, Australia.

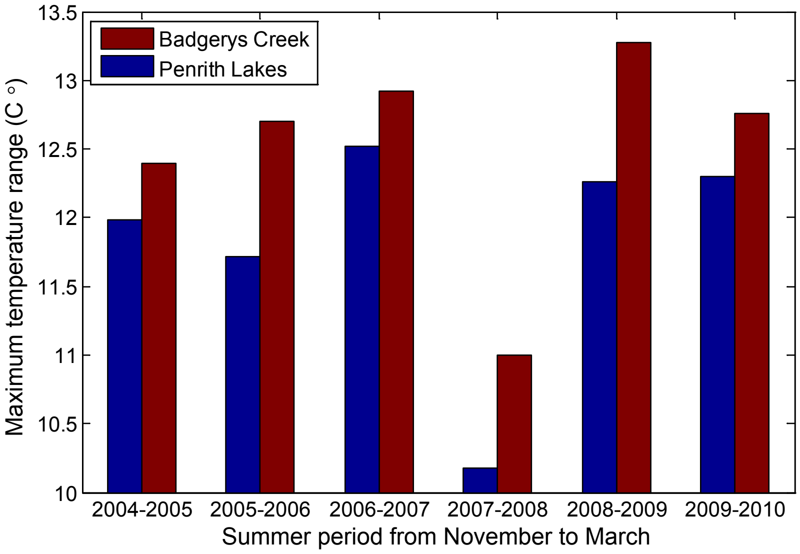

Figure 32 Averaged variation of the daily temperature over the summer periods over the summers from 2004 to 2009 obtained at the stations in Badgerys Creek (Station No #067108) and Penrith Lakes (Station No #067113). Source: Bureau of Meteorology, Australia.

Both of the wind and temperature data presented above suggest that the transport mechanism associated with the diurnal thermal forcing described above may be significant in an average sense over the summer of 2007-2008, and that the resultant transport rate is relatively low. Therefore, the increased sedimentation and the significantly weak flow expected over that period, coupled with the absence of motion in the very near-shore region may have provided an ideal condition for the algal bloom in Lake Burragorang over the summer of 2007-2008.

4.6 Summary

The numerical study described in this chapter has investigated the particle transport in a reservoir model under the effect of diurnal thermal forcing applied at the water surface. The temporal evolution of the general behaviour of the fluid flow and particle motion is described, followed by a quantitative comparison of particle flux, distribution and residence time under various conditions. Whilst the properties of particles are found to be important in determining the particle deposition, the effect of the induced flow is significant to both the deposition and dispersion of particles. The particle motion over a wide range of Grashof numbers has been quantified based on the present numerical model. It is found that when the Grashof number is reduced, the particle deposition is enhanced and the particle dispersion is reduced. These findings are consistent with the occurrence of an algal bloom in Lake Burragorang during the summer of 2007-2008.

The study confirms the important transport mechanism by natural convection which contributes to the deposition and dispersion of particles in reservoirs. That the result is consistent with the occurrence of an algal bloom in a real reservoir suggests that the understanding of how particle behaves under this mechanism is essential in terms of the management of water quality.

5. Preliminary investigation of a particle collision model

5.1 Introduction

In this chapter, the numerical model described in the previous chapter is extended with the inclusion of a particle collision model. A preliminary investigation is carried out to study the effect of particle collision on particle motion. The particle transport problem considered here is the same as that described in Chapter 4 except for the inclusion of the particle collision model.

Since particle collision may occur in natural reservoirs, it is meaningful to consider the particle collision behaviour in numerical models in order to fully understand the particle transport mechanism in real life. Numerical particle collision models have been extensively examined previously. As reviewed in [85], particle collision models that characterise the inter-particle behaviour have been developed based on various scenarios. However, only a few collision models have been substantially validated because of the difficulties with validation. Among the wide range of collision models, the validated model reported by O'Rourke [27] which has been discussed in Chapter 1, has gained popularity and is thus adopted in this chapter.

Similar to the previous numerical simulations with periodic thermal forcing applied at the water surface, an extended numerical model with many more particles is investigated here using the commercial CFD code ANSYS FLUENT 13 coupled with the previously described DPM and with the inclusion of the particle collision model (see Chapter 1 for details regarding the DPM and the particle collision model). The purpose of this study is to preliminarily quantify the effect of particle collision on particle size and mass distributions.

The contents of this chapter are organised as follows:

In Section 5.2, the specific details concerning the present numerical model are described based on the general reservoir model described in Chapter 2.

In Section 5.3, grid and time-step dependency tests are carried out.

In Section 5.4, the results obtained with the inclusion of the particle collision model are presented to demonstrate the effects of particle collision on particle size and mass distributions in the flow domain. The numerical data are presented in terms of the spectrum of the particle sizes and the deposition and dispersion behaviour of particles in various regions of the model.

The major findings of this study are briefly summarised in Section 5.5.

5.2 Numerical model formulation

Model formulation for fluid flow

The basic fluid flow model considered here is the two-dimensional reservoir model described in Chapter 2 (see Figure 4). All the configurations of the model, including the dimensions, the velocity boundary conditions, and the thermal boundary conditions are the same as those discussed in Chapter 4.

Model formulation for particle motion

Since this preliminary investigation is based on the scenario discussed in Chapter 4, particles are injected at the same locations and time as those for the previous model examined in Chapter 4. In the DPM a particle collision model is included in the simulation.

The boundary conditions for the DPM are also identical to those used in Chapter 4, i.e. the 'reflect' wall boundary condition for particles is assumed at the water surface and all the other walls of the model have the 'trap' wall boundary condition.

In this study, the general normalisation of parameters follows those mentioned in Chapter 2. An additional parameter of interest relevant to the particle collision model is the particle surface tension (σ), which characterises the particle coalescence behaviour when particles are involved in collision. Here the particle surface tension is normalised by $\sim m_p\, g/d_p$.

In the present numerical simulations, the Grashof number and Prandtl number are set to $Gr = 4.43 \times 10^4$ and $Pr = 6.82$, respectively. The geometric parameters (i.e. A and S) are fixed at 0.05 and 0.1, respectively. The normalised thermal forcing period is $P^* = 0.54$.

The normalised particle relaxation time is 3.63×10^{-9}, corresponding to a particle diameter of 10 μm and a particle density of $1.0 \times 10^{3}\ \mathrm{kg/m^{3}}$ (very close to the density of water). The volume fraction of the particles at the time of injection varies from 6.98×10^{-4} to 6.98×10^{-2}.

5.3 Grid and time-step dependency tests

With the inclusion of the particle collision model, it is deemed necessary to carry out grid and time-step dependency tests specifically for the current model. The meshes and corresponding time-steps used for the tests here are the same as those adopted in Section 3.3.1, which are 1722×102 mesh with a dimensionless time-step 7.29×10^{-7}, 861×51 mesh with a time-step 1.46×10^{-6}, and 430×26 mesh with a time-step 2.91×10^{-6}, respectively. The size of the mesh and the corresponding time-step are chosen so that the Courant-Friedrichs-Lewy (CFL) number [70] remains roughly the same for all of the three meshes. Similarly, the grid and time-step dependency tests are carried out using a case under constant temperature cooling at the water surface at a much higher Grashof number (i.e. $Gr = 10^{6}$) rather than a diurnal case. The Prandtl number is set at $Pr = 7$ for the test case. The particles with a maximum volume fraction of 1.40×10^{-4} are injected into the water body underneath the surface (at $y^{*} = -0.02$) along the region with the sloped bottom.

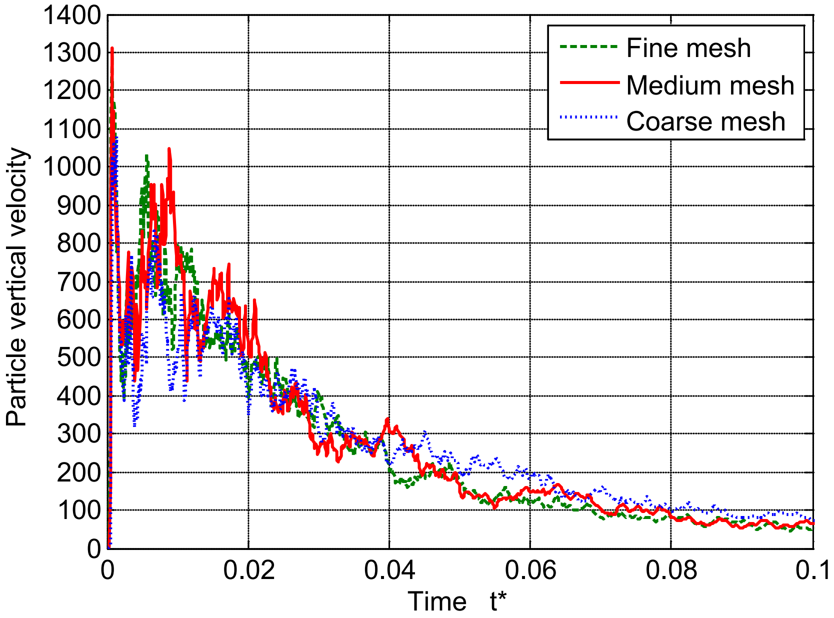

Figure 33 Time histories of the averaged particle vertical velocity obtained with the three different meshes.

The mesh and time-step dependency is examined based on quantitative data extracted from particle motions across the entire flow domain. The averaged vertical velocity of all suspending particles in the flow domain, which is believed to have a great influence on particle collision behaviour that occurs in local water columns, is calculated. The results obtained with the three different meshes are shown in Figure 33. Since in the test case a constant temperature is applied at the water surface and all other boundaries are adiabatic, the difference between the surface temperature and average temperature of the water body diminishes with time. As a consequence, the convective flow becomes weaker and eventually dies out, so does the particle motion.

Table 8 Comparison of the time lapses obtained from different meshes

Mesh resolution	1722×102	861×51	430×26
Peak time	0.0006	0.0007	0.0013
Settling time	0.0686	0.0704	0.0802
Time lapse	0.0680	0.0697	0.0789

Based on the behaviour of the particle velocity shown in Figure 33, the time lapses are determined for the three different meshes following a similar process as that described in Chapter 3. Here, the time lapse is between the time when the particle velocity peaks (referred to as 'Peak time') and the time when the particle velocity drops to a low value of 100 (this value is arbitrary; the corresponding time is referred to as 'Settling time'). The results are compared in Table 8, which demonstrates the convergence of the numerical results as the mesh and time-step are refined. As can be seen in Table 8, there is a significant improvement in the numerical accuracy when the medium mesh is employed in comparison with the coarse mesh. However, the variation of the numerical results between the medium and fine meshes is minimal. Therefore, for a compromise between the numerical accuracy and the computational time, the medium grid (861×51) and the corresponding time-step (1.46×10^{-6}) are chosen for the subsequent calculations. The choice of the mesh and time-step here is consistent with that for the case without the particle collision model.

5.4 Results

With the above formulated and tested model, different cases with different particle numbers and with and without the particle collision model are simulated (all the cases are listed in Table 9). For all these cases the Grashof number is fixed at $Gr = 4.43 \times 10^4$ and the Prandtl number is fixed at $Pr = 6.82$.

Table 9 Detail of the cases

Number of the case	Maximum volume fraction	Particle surface tension	Particle collision model
Case 1	6.98×10^{-4}	1.04×10^{5}	Yes
Case 2	6.98×10^{-2}	1.04×10^{5}	Yes
Case 3	6.98×10^{-4}	N/A	No
Case 4	6.98×10^{-2}	N/A	No

In what follows, firstly the time series of the spectrum of particle sizes are illustrated for the different cases. Subsequently, the influence of both the particle quantity and collision model is discussed. In all the plots shown in this section, the time $t = 0$ corresponds to the time when the particles are injected into the domain, and the time is normalised by the period P of the cyclic thermal forcing.

5.4.1 Spectrum of particle sizes

With the inclusion of the particle collision model in the numerical simulations, there is a possibility that the particles may coalesce after colliding with each other. As a consequence, the size of the particles remaining in the domain may vary over time. The instantaneous spectrum of particle sizes is thus worth examining as it shows the size distribution of the particles and is indicative of the overall particle collision behaviour.

A time series of the spectrum of particle sizes is illustrated in a 3D bar-chart in Figure 34. As can be seen in this figure, the suspending particles are classified into several diameter groups according to the consequent size of the particles after collision (see the labels of Diameters 1-6 in Figure 34. Here, Diameter 1 means single particles without coalescence; Diameter 2 means two coalesced particles after collision; and so on). The maximum particle size is thus indicative of the maximum bandwidth of the spectrum of the particle sizes.

Generally, it is evident in Figure 34 that the proportion of the remaining particles staying in their original diameter is monotonically decreasing; whereas the proportion of the other bigger particles is in turn growing. The above trend is expected as two or more particles tend to coalesce together as the result of particle collision.

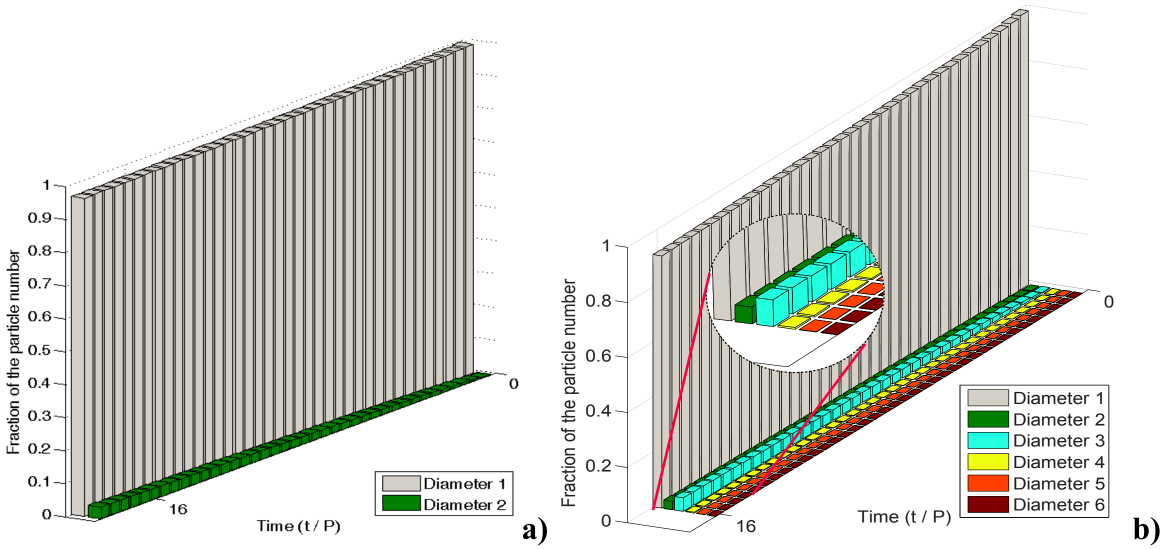

Figure 34 Time series of the spectrum of particle sizes for the particles remaining in the entire domain for a) Case 1; b) Case 2. Diameters 1-6 indicate the different sizes of the particles which are 1-6 time(s) of the original size.

Furthermore, the maximum bandwidth of the spectrum of the particle sizes for Case 1 is much smaller than that for Case 2, which is clear from the comparison between Figure 34a and Figure 34b. In Case 1 (refer to Figure 34a), particles larger than Diameter 2 are not present in the flow domain over the calculated time period, whereas in Case 2 (refer to Figure 34b), particles up to Diameter 6 are present although the number of the larger particles with Diameters 4-6 is very small. The variation between Cases 1 and 2 may be attributed to the difference in the particle concentration. In the former case (Case 1), the particle concentration is very low, which limits the possibility of particle collision. It is also interesting to note that, in Case 2 with much higher particle concentration at the time of the injection, more particles with Diameter 3 have formed after several thermal forcing cycles than the particles with other diameters (except for the particles staying in the original diameter). Two factors determine the distribution of the particle sizes following collision: one is the collision efficiency and the other is the coalescence efficiency. Since there are more particles at the time of the injection in Case 2 than in Case 1, the collision efficiency for Case 2 is much higher. Furthermore, the coalescence efficiency is generally higher for the particles with larger diameters than smaller ones (provided that the collision efficiency is sufficiently high to enable collision), and thus the particles with Diameter 2 may have a greater opportunity to coalesce with single particles to form the larger particles with Diameter 3 (as is shown in Figure 34b for Case 2). The same analogy, however, would not apply to the particles with Diameter 3 since their concentration and in turn the collision efficiency would be much lower than those with Diameter 2 for the present case. Further, larger particles have a higher tendency to settle than smaller particles.

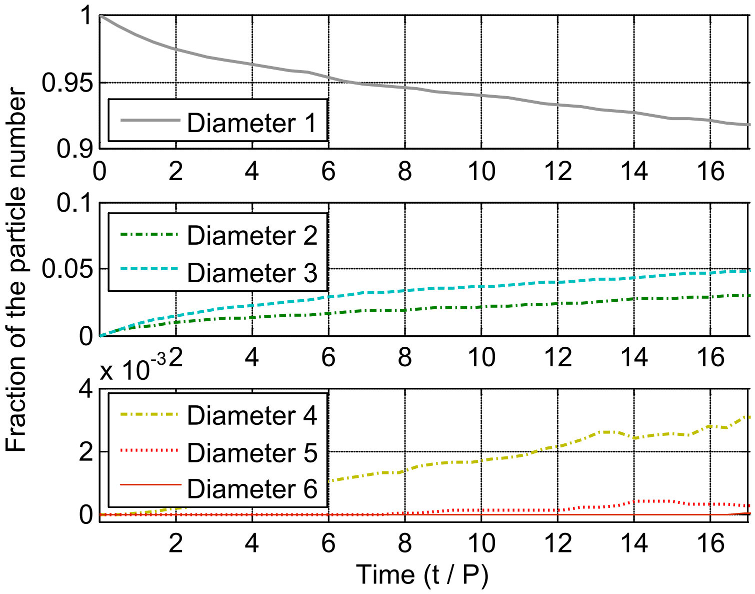

Figure 35 Time series of the fractions of the number of particles in Diameters 1-6 in the entire domain for Case 2.

In Figure 35, the time evolution of different particle sizes in Case 2 is illustrated. The following observations can be made in this figure: Firstly, the number of particles with the original size (Diameter 1) continuously decreases over time, as noted above. Secondly, the cluster of particles with Diameter 2 and 3 begin to form almost immediately after the particle injection, which is expected since the volume fraction of the particles is at its maximum at the time of the injection. Thirdly, as mentioned above, the fraction of the particle number with Diameter 3 increases more rapidly than that with Diameter 2 from very early on. The relatively smaller fraction of the particle number with Diameter 2 is attributed to the formation of the larger particles with Diameter 3. This confirms that particle collision efficiency is high when the volume fraction of particles is at its maximum.

Finally, it is worth noting that an oscillatory pattern is observed from the fraction of the particle numbers with Diameters 4 and 5. The cause of the fluctuating behaviour may be due to the relatively faster deposition rate for the larger particles, which removes the larger particles quickly from the flow. Given the above-described observation, it is expected that in Case 2 the fraction of the overall particle number remaining in the domain decreases sharply, which will be detailed in later sections.

5.4.2 Effect of particle collision on particle transport

5.4.2.1 Remaining particle fraction in the entire flow domain

The ratio of the remaining particle quantity across the entire flow domain over the total particle quantity at the time of the injection indicates the concentration of the particles in the water body, which is of concern from the perspectives of environmental engineering applications. Here, the ratios of the remaining particle number/mass to the total injected particle number/mass (referred to as the fractions of the residual particle number/mass hereinafter) are calculated and discussed. The results are shown in Figure 36 and Figure 37 respectively.

It is seen in Figure 36 that the fraction of the residual particle number is decreasing as expected for all the cases listed in Table 9. The descending trend illustrated in the figure is similar to that presented in Figure 27 in Chapter 4.

It is also clear in In Figure 36 that the results obtained with the non-collision particle transport model (Cases 3 and 4) are identical despite the different particle numbers at the time of injection. This result is expected as the fluid flow structures for all the cases are the same owing to the same numerical parameters adopted in the fluid flow model. Interestingly, the result obtained from Case 1 with the inclusion of the particle collision model is in line with Cases 3 and 4, which means the influence of the particle collision model on particle transport is insignificant in this case. This is not surprising as the particle concentration is very low in Case 1 and thus the collision efficiency is also very low. However, the result from Case 2, unlike the results of the other cases, shows a significantly lower fraction of the residual particle number at all the time. This is due to the higher concentration of particles, which results in higher collision and coalescence efficiencies, and is consistent with the above observation of the particle size distribution.

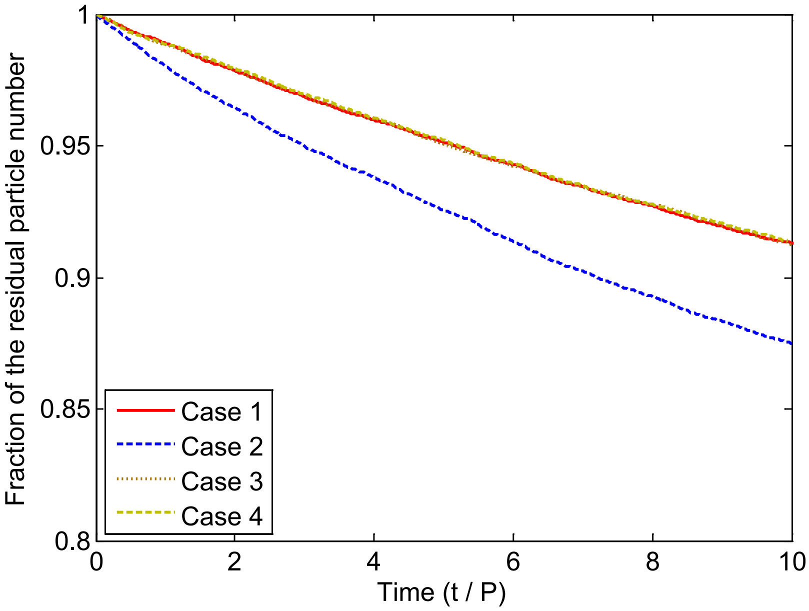

Figure 36 Time series of the fraction of the residual particle number in the entire domain.

For comparison purpose, Figure 37 shows the time series of the fraction of the residual particle mass for all the cases. As can be seen in this figure, the four curves for the different cases are very similar to each other, suggesting that the overall deposition rate of the particles in terms of the particle mass is not significantly affected by particle collision within the present range of particle concentrations (at least up to the number of the calculated thermal cycles). However, the minor variation of the result from Case 2 compared with the other three cases is noteworthy. Case 2 has a slightly faster deposition rate, resulting in a lower fraction of the residual particle mass, as shown in Figure 37. The variation seems to be amplifying with time. This may be due to the formation of larger particles, which are more prone to sedimentation.

It has been demonstrated in Figure 36 that the particle collision possibility increases when more particles are present at the time of the injection, which contributes to the relatively higher coalescence efficiency. In contrast, it has been demonstrated in Figure 37 that the particle deposition rate in terms of the particle mass is similar in the four different cases, despite the variations of the particle number at the time of the injection and whether or not the particle collision model is included. Therefore, the present results indicate that the particle collision model mainly affects the particle size distribution, but does not substantially change the quantity of the particle mass in the flow domain.

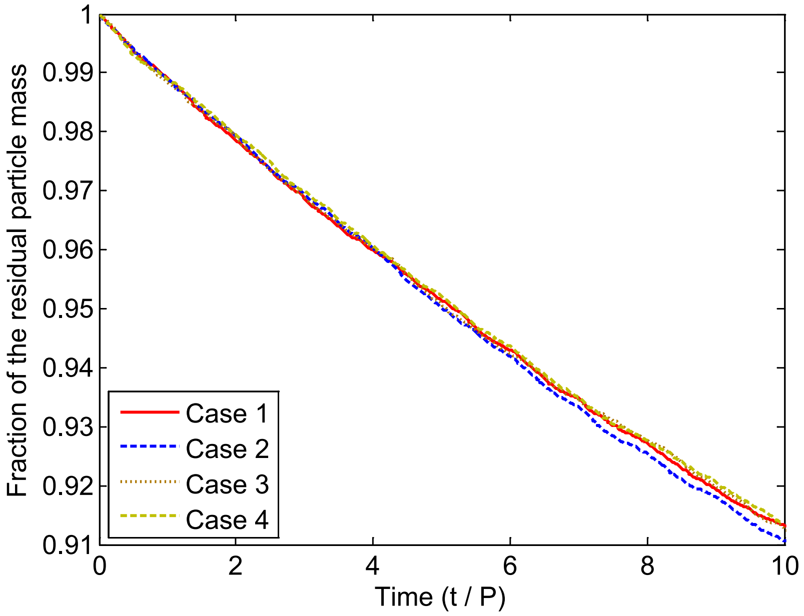

Figure 37 Time series of the fraction of the residual particle mass in the entire domain.

5.4.2.2 Particle fraction in the tip regions

The particle collision model may also affect the spatial distribution of the remaining particles in the water body. A particular parameter of interest is the particle concentration in the tip region, which is indicative of the particle dispersion rate (refer to the results reported in Chapter 4). In this section, the fraction of the remaining particle number/mass in the tip region (i.e. the sloped bottom region) is examined.

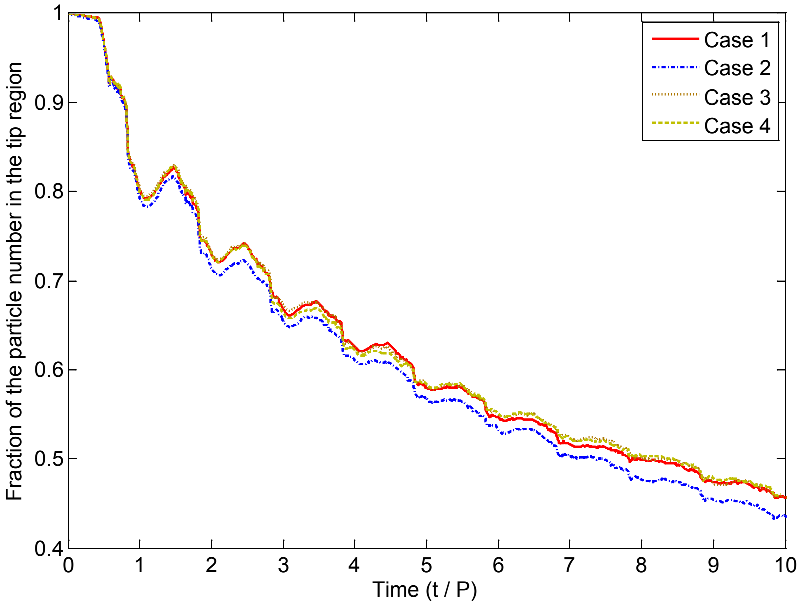

Figure 38 Time series of the fraction of the remaining particle number in the tip region.

In Figure 38, the time series of the fraction of the remaining particle number in the tip region are plotted for all the cases. Clearly the fraction of the remaining particles reduces over time. As seen in this figure, the particle dispersion behaviour in Cases 1, 3 and 4 is very similar under the effect of the same fluid flow regardless of the variation of the number of the total injected particles. The only minor variation is that the result from Case 2 with more particles at the time of the injection and with the inclusion of the collision model demonstrates a slightly lower particle fraction than the other cases. The observation here is consistent with that discussed in Section 5.4.2.1.

Figure 39 shows the time series of the fraction of the remaining particle mass in the tip region obtained for all the four cases, which are almost identical. The results in figures 38 and 39 again confirm that the particle collision mainly affects the particle size distribution (and thus the number of particles) but not the mass distribution over the present range of flow and particle parameters.

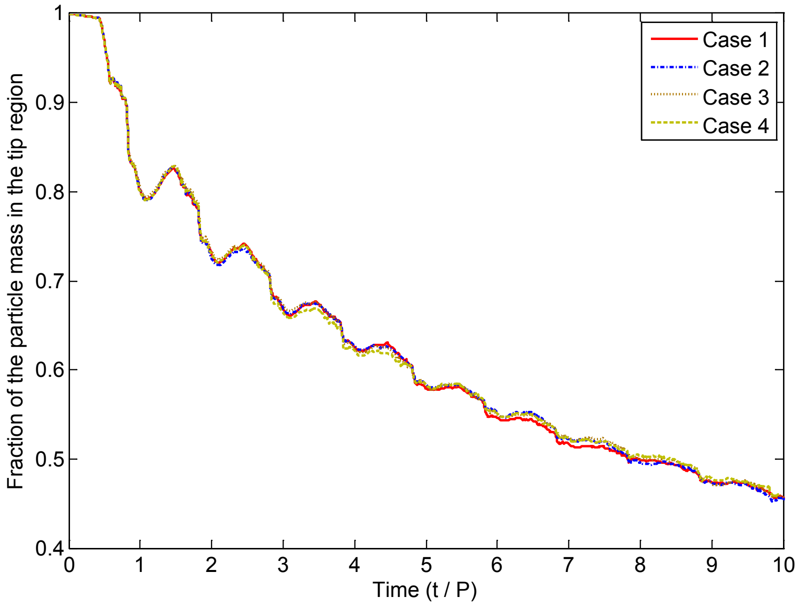

Figure 39 Time series of the fraction of the remaining particle mass in the tip region.

The major findings from the present collision model can be summarised as follows. First, the effect of the collision model on the particle motion can be neglected if the injected number of particles is relatively small (e.g. Case 1); whereas the influence of the particle collision model becomes significant when the injected particle number increases. Second, whilst the particle collision model may have a significant effect on the particle size distribution, depending on the initial particle concentration, its impact on the particle mass distribution is insignificant.

5.5 Conclusions

A preliminary analysis of the particle collision behaviour for particle transport in reservoirs subject to diurnal thermal forcing has been carried out using a CFD code coupled with the DPM with the inclusion of the particle collision model. First, the particle size distribution for the cases with the different number of particles and with the inclusion of the collision model is discussed based on the spectra of particle diameters. The results confirm the importance of the volume fraction of the particles at the time of the injection in determining the particle coalescence efficiency in the numerical model, and in turn determining the particle size distribution. Second, the effect of the particle collision on the particle deposition and dispersion behaviour is analysed in terms of particle number and particle mass in different regions of the water body. The comparison between the different cases reveals the significance of the particle collision model to the particle deposition and dispersion behaviour.

The present study has demonstrated that the particle collision behaviour may affect the fraction of the remaining particle number in the domain, provided that the particle number at the time of the injection is sufficiently high. However, the particle collision behaviour does not have significant influence on the distribution of the particle mass. Therefore, the influence of particle collision in the reservoir model under natural convection is minimal from the environmental engineering point of view, in which the mass distribution of nutrients or pollutants is of the major concern.

The limitations of the particle collision model adopted in this preliminary study are worth noting. Firstly, the model does not account for the possible break-up behaviour of the particles that may occur in real life situations, which are dependent on either the shear induced by fluid flows, or the inter-particle impact generated by particle collision. Secondly, the formation of the bigger particles may require a two-way coupling approach for the flow and particle interaction since the particles may be large enough to influence the fluid flow. However, the present study involves only one-way coupling, assuming that the motion of the particles does not affect the flow irrespective of the size of the particles.

6. Summary and future work

6.1 Summary

This thesis aims to investigate the influence of the transient flow within a reservoir model in response to periodic thermal forcing at the water surface on the transport of particles within the water body, which is important for water quality management. For this purpose, numerical simulations based on the CFD solver – ANSYS FLUENT 13 coupled with a built-in DPM have been carried out.

Firstly, the results from a numerical simulation of the TLC particle transport in the reservoir are compared with the results from the previously reported concurrent PIT/PIV experiment which validates the numerical model. Using the validated model an extended investigation has quantified the dependence of the flow response and its stability properties on the Grashof number. Secondly, a numerical study has been carried out to investigate the particle deposition and dispersion behaviour in the reservoir. The study has confirmed the important role of natural convection in transporting pollutant or nutrient in reservoirs and quantified the dependence of the particle deposition and dispersion on cyclic thermal forcing. Finally, following the above-described scenario, an extended particle transport model with the inclusion of particle collision has been investigated. The importance of particle collision for the particle deposition and dispersion in reservoirs has been identified from the preliminary investigation of the particle collision model.

6.1.1 Numerical modelling of the PIT/PIV experiment with TLC particles

In the numerical modelling of the concurrent PIT/PIV experiment, the temperature and velocity field of the thermal flow are visualised and measured using the particle information.

For validating the numerical model, the results obtained with the particle temperature and velocity fields have been compared with the experiment both qualitatively and quantitatively. The comparison shows consistent results between the present numerical simulation and the experiment reported in [6].

With the validated model, further results regarding the dependence of the flow and its stability properties on the Grashof number have been obtained by extending the Grashof number of the model to a wider range. Firstly, the onset time of the flow instability over each thermal forcing cycle has been obtained quantitatively, and the correlation of the onset time of the instability with the Grashof number has been determined as:

$$t_b = 1.91\, Gr^{-0.17}$$

Secondly, the time duration with the presence of a distinct cellular flow structure associated with the instability has been examined. The correlation of the time duration of the instability with the Grashof number has been obtained as:

$$t_{dt} = 216\, Gr^{-0.77}$$

Finally, the time lag between the flow response and the switch of the thermal forcing between heating and cooling has been quantified. The correlation of the time lag with the Grashof number has been obtained as:

$$t_{lag} = 0.37\, Gr^{-0.12}$$

6.1.2 Transport of pollutant particles in a reservoir due to diurnal temperature variation

A numerical study has been carried out to examine the particle transport in the reservoir in a pseudo real-life scenario, in which solid pollutant or nutrient particles of spherical shape are injected from the sidearm of the reservoir. In this study, the temporal evolution of the fluid flow and particle motion has been discussed, followed by a quantitative description of the particle flux, the particle fraction, and the residence time of the particles in various regions of the reservoir. Whilst the properties of the particles are found to be important in determining particle deposition, the effect of the thermally induced flow is significant to both the deposition and dispersion of the particles. If the Grashof number is reduced, the particle deposition is enhanced and the particle dispersion is also reduced. The above-described correlations are recapped below.

An empirical correlation quantifying the effect of the Grashof number on the normalised mean residence time of the particles in the whole domain is given as follows:

$$t_{all} = 85.27e^{6.3\times10^{-6}\,Gr}$$

This correlation indicates that the increase of the drag force on particles as a result of the more intensive fluid flow at the higher Grashof numbers undermines the effect of gravitational settling on particle motion. In that sense, the deposition of the particles reduces with the increasing Grashof number.

Similarly, an empirical correlation characterising the dependence of the normalised particle residence time in the entire tip region on the Grashof number is obtained as follows:

$$t_{tip} = 2419\ Gr^{-\frac{1}{2}}$$

The above correlation shows that with the increasing Grashof number the residence time of the particles in the tip region decreases and thus the dispersion of the particles increases.

The above findings have confirmed the important transport mechanism under natural convection which contributes to the deposition and dispersion of particles in reservoirs. The outcome of the study suggests that the understanding of how particle behaves under this mechanism is important for water quality management.

6.1.3 Preliminary investigation of a particle collision model

The numerical model discussed in Chapter 4 has been extended to examine the particle motion with the inclusion of a particle collision model. The influence of the particle collision behaviour on the particle size distribution as well as particle motion within the water body has been preliminarily investigated.

It is found that particle collision may affect the remaining particle number and the particle size distribution in the flow domain as a result of coalescence of the particles, provided that the particle number at the time of the injection is sufficiently high for particle collision to take place. However, the particle collision and the consequent coalescence of particles do not have significant influence on the particle mass distribution. Therefore, the potential impact of the particle collision behaviour on the water quality in reservoirs under natural convection is insignificant.

6.2 Future work

Although the particle transport model in reservoirs subject to periodic thermal forcing has been well validated by the corresponding experiment and the results derived from it have been analysed and discussed in this thesis, only a significantly simplified model has been investigated and the case study reported in Chapter 4 is merely concerned with the pseudo real-life scenario. The real-life situation concerning particle transport is far more complex than what is considered here, and is subject to numerous other transport mechanisms. In addition to natural convection induced by thermal forcing at the water surface which has been specifically investigated in the present thesis, other transport mechanisms such as wind stress, influent flow, evaporation and rainfall etc. need to be considered in order to develop a more accurate particle transport model relevant to field situations. Moreover, particle re-suspension in natural water bodies is another common phenomenon that is worth considering. Therefore, the following investigations may be undertaken to further improve the present particle transport model:

The study described in Chapter 4 involves a diurnal temperature variation at the water surface in the simple form of a standard sinusoidal function of time. Future investigation may involve the incorporation of more realistic in-situ temperature data as input variables into the numerical model. In addition, the unstable flow induced by solar radiation re-emitted as a heat flux from the bottom of reservoirs is another important thermal-driven transport mechanism that may occur in field situations when the water depth is less than the penetration depth of solar radiation during day-time heating, e.g. in certain areas of the tip region of reservoirs. Therefore, the in-situ data regarding intensities of solar radiation may need to be monitored and included for further consideration. By doing so, the numerical results will be more relevant to the real-life scenario.

Further, based on the in-situ meteorological data, other transport mechanisms such as wind shear on the water surface that may significantly alter the fluid flow pattern in natural water bodies and in turn affect the particle transport, may be incorporated into the present numerical model. It is also necessary to extend the present two-dimensional model to a full three-dimensional one, which may incorporate realistic geographic details of real reservoirs.

Finally, based on the particle transport model described in Chapters 4 and 5, further improvement to the numerical model may include particle re-suspension and breakup mechanisms. Particles settled at the bottom of the reservoir may be taken up by the flow and redistributed elsewhere. The particle re-suspension effect may offset the effect of the particle deposition, and thus may contribute significantly to the overall distribution of pollutants or nutrients in natural water bodies. Similarly, the breakup of large particles may reverse the effect of coalescence of particles, and thus change the deposition and dispersion behaviour of the particles.

References

1. S. Monismith, J. Imberger and M. L. Morison, *Convective motions in the sidearm of a small reservoir.* Journal of Limnology and Oceangraphy, 1990. **35**(8): p. 1676-1702.
2. D.E. Farrow and J.C. Patterson, *On the response of a reservoir sidearm to diurnal heating and cooling.* Journal of Fluid Mechanics, 1993. **246**: p. 143-161.
3. C. Lei and J.C. Patterson, *Natural convection in a reservoir sidearm subject to solar radiation: a two-dimentional simulation.* Numerical Heat Transfer, Part A: Applications, 2002. **42**(1-2): p. 13-32.
4. C. Lei and J.C. Patterson, *A direct three-dimensional simulation of radiation-induced natural convection in a shallow wedge.* International Journal of Heat and Mass Transfer, 2003. **46**(7): p. 1183-1197.
5. T.P. Bednarz, C. Lei, and J.C. Patterson, *An experimental study of unsteady natural convection in a reservoir model cooled from the water surface.* Experimental Thermal and Fluid Science, 2008. **32**(3): p. 844-856.
6. T.P. Bednarz, C. Lei, and J.C. Patterson, *An experimental study of unsteady natural convection in a reservoir model subject to periodic thermal forcing using combined PIV and PIT techniques.* Experiments in Fluids, 2009. **47**(1): p. 107-117.
7. Y. Mao, C. Lei, and J.C. Patterson, *Unsteady near-shore natural convection induced by surface cooling.* Journal of Fluid Mechanics, 2010. **642**: p. 213-233.
8. B.L.B. Wiman, M.H. Unsworth, S.E. Lindberg, B. Bergkvist, R. Jaenicke, and H.-C. Hansson, *Perspectives on aerosol deposition to natural surfaces: interactions between aerosol residence times, removal processes, the biosphere and global environmental change.* Journal of Aerosol Science, 1990. **21**(3): p. 313-338.
9. M. Pilou, S. Tsangaris, P. Neofytou, C. Housiadas, and Y. Drossinos, *Inertial Particle Deposition in a 90 degrees Laminar Flow Bend: An Eulerian Fluid Particle Approach.* Aerosol Science and Technology, 2011. **45**(11): p. 1376-1387.
10. E. Wolanski, K.E. Fabricius, T.F. Cooper, and C. Humphrey, *Wet season fine sediment dynamics on the inner shelf of the Great Barrier Reef.* Estuarine, Coastal and Shelf Science, 2008. **77**(4): p. 755-762.
11. A. Guha, *Transport and Deposition of Particles in Turbulent and Laminar Flow.* Annual Review of Fluid Mechanics, 2008. **40**(1): p. 311-341.
12. M.K. Akbar, M. Rahman, and S.M. Ghiaasiaan, *Particle transport in a small square enclosure in laminar natural convection.* Journal of Aerosol Science, 2009. **40**(9): p. 747-761.

13. C. Lei and J.C. Patterson, *Unsteady natural convection in a triangular enclosure induced by absorption of radiation.* Journal of Fluid Mechanics, 2002. **460**: p. 181-209.
14. C. Lei and J.C. Patterson, *Natural convection induced by diurnal heating and cooling in a reservoir with slowly varying topography.* JSME International Journal Series B Fluids and Thermal Engineering, 2006. **49**(3): p. 605-615.
15. T.P. Bednarz, C. Lei, and J.C. Patterson, *A numerical study of unsteady natural convection induced by iso-flux surface cooling in a reservoir model.* International Journal of Heat and Mass Transfer, 2009. **52**(1–2): p. 56-66.
16. T.P. Bednarz, C. Lei, and J.C. Patterson, *Unsteady natural convection induced by diurnal temperature changes in a reservoir with slowly varying bottom topography.* International Journal of Thermal Sciences, 2009. **48**(10): p. 1932-1942.
17. C. Lei and J.C. Patterson, *Natural convection in a reservoir sidearm subject to solar radiation: experimental observations.* Experiments in Fluids, 2002. **32**(5): p. 590-599.
18. Y. Mao, C. Lei, and J.C. Patterson, *Unsteady natural convection in a triangular enclosure induced by absorption of radiation - A revisit by improved scaling analysis.* Journal of Fluid Mechanics, 2009. **622**: p. 75-102.
19. C. Lei and J.C. Patterson, *A direct stability analysis of a radiation-induced natural convection boundary layer in a shallow wedge.* Journal of Fluid Mechanics, 2003. **480**: p. 161-184.
20. C. Lei and J.C. Patterson, *Unsteady natural convection in a triangular enclosure induced by surface cooling.* International Journal of Heat and Fluid Flow, 2005. **26**(2): p. 307-321.
21. C.N. Davies, *Definitive equations for the fluid resistance of spheres.* Proceedings of the Physical Society, 1945. **57**(4): p. 259.
22. R.M. Samelson, *Lectures on Geophysical Fluid Dynamics.* Eos, Transactions American Geophysical Union, 1998. **79**(45): p. 547-547.
23. S.A. Morsi and A.J. Alexander, *An investigation of particle trajectories in two-phase flow systems.* Journal of Fluid Mechanics, 1972. **55**(02): p. 193-208.
24. L. Talbot, R.K. Cheng, R.W. Schefer, and D.R. Willis, *Thermophoresis of particles in a heated boundary layer.* Journal of Fluid Mechanics, 1980. **101**(04): p. 737-758.
25. P.G. Saffman, *The lift on a small sphere in a slow shear flow.* Journal of Fluid Mechanics, 1965. **22**(02): p. 385-400.
26. A. Li and G. Ahmadi, *Dispersion and Deposition of Spherical Particles from Point Sources in a Turbulent Channel Flow.* Aerosol Science and Technology, 1992. **16**(4): p. 209-226.
27. P.J. O'Rourke, *Collective drop effects on vaporizing liquid sprays*, thesis, Princeton University, 1981.
28. J.F. Groeneweg, *The statistical description of a spray in terms of drop velocity, size, and position*, thesis, The University of Wisconsin - Madison, 1967.

29. *Collision frequency*, Date of access: 18/08/2013; Available from: http://chemwiki.ucdavis.edu/Physical_Chemistry/Kinetics/Rate_Laws/Gas_Phase_Kinetics/Collision_Theory/Collision_Frequency.
30. Q. Li, T. Cai, G. He, and C. Hu, *Droplet collision and coalescence model.* Applied Mathematics and Mechanics, 2006. **27**(1): p. 67-73.
31. J. Patterson and J. Imberger, *Unsteady natural convection in a rectangular cavity.* Journal of Fluid Mechanics, 1980. **100**(01): p. 65-86.
32. M.A. Teamah and W.M. El-Maghlany, *Numerical simulation of double-diffusive mixed convective flow in rectangular enclosure with insulated moving lid.* International Journal of Thermal Sciences, 2010. **49**(9): p. 1625-1638.
33. R.J. Adrian, *Particle-Imaging Techniques for Experimental Fluid Mechanics.* Annual Review of Fluid Mechanics, 1991. **23**(1): p. 261-304.
34. G.G. Joseph, R. Zenit, M.L. Hunt, and A.M. Rosenwinkel, *Particle–wall collisions in a viscous fluid.* Journal of Fluid Mechanics, 2001. **433**: p. 329-346.
35. A. Dehbi and S. Martin, *CFD simulation of particle deposition on an array of spheres using an Euler/Lagrange approach.* Nuclear Engineering and Design, 2011. **241**(8): p. 3121-3129.
36. M. Balthasar, F. Mauss, M. Pfitzner, and A. Mack, *Implementation and validation of a new soot model and application to aeroengine combustors.* Journal of Engineering for Gas Turbines and Power, 2002. **124**(1): p. 66-74.
37. M. Balthasar, A. Heyl, F. Mauß, F. Schmitt, and H. Bockhorn, *Flamelet modeling of soot formation in laminar ethyne/air-diffusion flames.* Symposium (International) on Combustion, 1996. **26**(2): p. 2369-2377.
38. D. Koolpiruck, S. Prakoonwit, and W. Balachandran. *Deposition of charged inhaled aerosols with transient airflow in sequential lung airway model.* in *Conference Record of the 2004 IEEE Industry Applications Conference*. 2004. WA, United States: 39th IAS Annual Meeting.
39. D.K. Walters and W.H. Luke, *Computational fluid dynamics simulations of particle deposition in large-scale, multigenerational lung models.* Journal of Biomechanical Engineering, 2010. **133**(1).
40. Q. Chen, *Comparison of different k-ε models for indoor air flow computations.* Numerical Heat Transfer, Part B: Fundamentals, 1995. **28**(3): p. 353-369.
41. J.D. Posner, C.R. Buchanan, and D. Dunn-Rankin, *Measurement and prediction of indoor air flow in a model room.* Energy and Buildings, 2003. **35**(5): p. 515-526.
42. N. Zhang, Z.C. Zheng, L. Glasgow, and B. Braley, *Simulation of particle deposition at the bottom surface in a room-scale chamber with particle injection.* Advanced Powder Technology, 2010. **21**(3): p. 256-267.
43. G.M. Faeth, *Evaporation and combustion of sprays.* Progress in Energy and Combustion Science, 1983. **9**(1–2): p. 1-76.
44. W. Yan, Z. Luo, and A. Guo, *Coupling of CFD with PBM for a pilot-plant tubular loop polymerization reactor.* Chemical Engineering Science, 2011. **66**(21): p. 5148-5163.

45. B.H. Xu and A.B. Yu, *Numerical simulation of the gas-solid flow in a fluidized bed by combining discrete particle method with computational fluid dynamics.* Chemical Engineering Science, 1997. **52**(16): p. 2785-2809.

46. S. Kondaraju, E.K. Jin, and J.S. Lee, *Direct numerical simulation of thermal conductivity of nanofluids: The effect of temperature two-way coupling and coagulation of particles.* International Journal of Heat and Mass Transfer, 2010. **53**(5): p. 862-869.

47. A. Dehbi, *Turbulent particle dispersion in arbitrary wall-bounded geometries: A coupled CFD-Langevin-equation based approach.* International Journal of Multiphase Flow, 2008. **34**(9): p. 819-828.

48. S.E. Pratsinis and K.-S. Kim, *Particle coagulation, diffusion and thermophoresis in laminar tube flows.* Journal of Aerosol Science, 1989. **20**(1): p. 101-111.

49. R. Tsai and L.J. Liang, *Correlation for thermophoretic deposition of aerosol particles onto cold plates.* Journal of Aerosol Science, 2001. **32**(4): p. 473-487.

50. J. Srebric, V. Vukovic, G. He, and X. Yang, *CFD boundary conditions for contaminant dispersion, heat transfer and airflow simulations around human occupants in indoor environments.* Building and Environment, 2008. **43**(3): p. 294-303.

51. A.M. Kamp, A.K. Chesters, C. Colin, and J. Fabre, *Bubble coalescence in turbulent flows: A mechanistic model for turbulence-induced coalescene applied to microgravity bubbly pipe flow.* International Journal of Multiphase Flow, 2001. **27**(8): p. 1363-1396.

52. V.V. Buwa and V.V. Ranade, *Dynamics of gas–liquid flow in a rectangular bubble column: experiments and single/multi-group CFD simulations.* Chemical Engineering Science, 2002. **57**(22–23): p. 4715-4736.

53. P.T.L. Koh and M.P. Schwarz, *CFD modelling of bubble–particle collision rates and efficiencies in a flotation cell.* Minerals Engineering, 2003. **16**(11): p. 1055-1059.

54. M.T. Dhotre, V.S. Vitankar, and J.B. Joshi, *CFD simulation of steady state heat transfer in bubble columns.* Chemical Engineering Journal, 2005. **108**(1–2): p. 117-125.

55. A.A. Kulkarni, K. Ekambara, and J.B. Joshi, *On the development of flow pattern in a bubble column reactor: Experiments and CFD.* Chemical Engineering Science, 2007. **62**(4): p. 1049-1072.

56. M.V. Tabib, S.A. Roy, and J.B. Joshi, *CFD simulation of bubble column—An analysis of interphase forces and turbulence models.* Chemical Engineering Journal, 2008. **139**(3): p. 589-614.

57. M.R. Bhole, J.B. Joshi, and D. Ramkrishna, *CFD simulation of bubble columns incorporating population balance modeling.* Chemical Engineering Science, 2008. **63**(8): p. 2267-2282.

58. P. Nerisson, O. Simonin, L. Ricciardi, A. Douce, and J. Fazileabasse, *Improved CFD transport and boundary conditions models for low-inertia particles.* Computers & Fluids, 2011. **40**(1): p. 79-91.

59. D.Y.H. Pui, F. Romay-Novas, and B.Y.H. Liu, *Experimental study of particle deposition in bends of circular cross section.* Aerosol Science and Technology, 1987. **7**(3): p. 301-315.
60. B.Y.H. Liu and J.K. Agarwal, *Experimental observation of aerosol deposition in turbulent flow.* Journal of Aerosol Science, 1974. **5**(2): p. 145-155.
61. J. Pallares and F.X. Grau, *Particle dispersion in a turbulent natural convection channel flow.* Journal of Aerosol Science, 2012. **43**(1): p. 45-56.
62. S.K. Friedlander and H.F. Johnstone, *Deposition of Suspended Particles from Turbulent Gas Streams.* Industrial & Engineering Chemistry, 1957. **49**(7): p. 1151-1156.
63. C.J. Geankoplis, *Transport processes and separation process principles*, United States Upper Saddle River, NJ : Prentice Hall Professional Technical Reference, 2003.
64. T.R. Anthony and M.R. Flynn, *CFD model for a 3-D inhaling mannequin: Verification and validation.* Annals of Occupational Hygiene, 2006. **50**(2): p. 157-173.
65. D. Mackay and M. Diamond, *Application of the QWASI (Quantitative Water Air Sediment Interaction) fugacity model to the dynamics of organic and inorganic chemicals in lakes.* Chemosphere, 1989. **18**(7–8): p. 1343-1365.
66. D.D. Gray and A. Giorgini, *The validity of the boussinesq approximation for liquids and gases.* International Journal of Heat and Mass Transfer, 1976. **19**(5): p. 545-551.
67. T. Aspelmeier, G. Giese, and A. Zippelius, *Cooling dynamics of a dilute gas of inelastic rods: A many particle simulation.* Physical Review E, 1998. **57**(1): p. 857-865.
68. W. Du, X. Bao, J. Xu, and W. Wei, *Computational fluid dynamics (CFD) modeling of spouted bed: Influence of frictional stress, maximum packing limit and coefficient of restitution of particles.* Chemical Engineering Science, 2006. **61**(14): p. 4558-4570.
69. G.M. Horsch and H.G. Stefan, *Convective circulation in littoral water due to surface cooling.* Journal of Limnology and Oceangraphy, 1988. **33**(5): p. 1068-1083.
70. T. Poinsot and S.M. Candel, *The influence of differencing and CFL number on implicit time-dependent non-linear calculations.* Journal of Computational Physics, 1986. **62**(2): p. 282-296.
71. J. Westerweel, *Statistics of PIV images*, in *Digital particle image velocimetry : theory and application*, 1993, Delft University Press: Delft, Netherlands.
72. G.H. Yeoh and J. Tu, *Gas-Particle Flows*, in *Computational techniques for multiphase flows*, 2009, Elsevier.
73. *TLC product for use in research and testing applications*, Date of access: 03/11/2013; Available from: http://hallcrest.com/downloads/RT001%20R&T%20Prods%20Info%20Package.pdf.
74. *Using TLC slurries*, Date of access: 11/03/2013; Available from: http://www.thermometersite.com/using_tlc_slurries.pdf.
75. T.A. Kowalewski, *Particle image velocimetry and thermometry for two-phase flow problems.* Annals of the New York Academy of Sciences, 2002. **972**(1): p. 213-222.

76. C. Tropea, A.L. Yarin, and J.F. Foss, *Material Properties: Measurement and Data*, in *Springer handbook of experimental fluid mechanics*, 2007, Springer: Berlin.

77. H. Ounis, G. Ahmadi, and J.B. McLaughlin, *Dispersion and deposition of Brownian particles from point sources in a simulated turbulent channel flow.* Journal of Colloid And Interface Science, 1991. **147**(1): p. 233-250.

78. *Linear Regression*. Matlab 2013a Documentation, 2013.

79. R. Puragliesi, A. Dehbi, E. Leriche, A. Soldati, and M.O. Deville, *DNS of buoyancy-driven flows and Lagrangian particle tracking in a square cavity at high Rayleigh numbers.* International Journal of Heat and Fluid Flow, 2011. **32**(5): p. 915-931.

80. N. Filippovic, M. Kojic, and A. Tsuda, *Modelling thrombosis using dissipative particle dynamics method.* Philosophical Transactions of The Royal Society, 2008. **366**(1879): p. 3265-3279.

81. S. Chen, C. Lei, and J.C. Patterson, *Numerical modeling of a concurrent PIT/PIV experiment with TLC particles in a reservoir model subject to periodic thermal forcing,* Numerical Heat Transfer, Part A: Applications, (2013), in press.

82. R. Kristiana, L.C. Vilhena, G. Begg, J.P. Antenucci, and J. Imberger, *The management of Lake Burragorang in a changing climate: The application of the Index of Sustainable Functionality.* Lake and Reservoir Management, 2011. **27**(1): p. 70-86.

83. 2009 *What causes algal blooms*, Department of Primary Industries [Australian government's report], Date of access: 02/08/2013; Available from: http://www.water.nsw.gov.au/Water-Management/Water-quality/Algal-information/What-causes-algal-blooms/What-causes-algal-blooms/default.aspx.

84. 2007 *Drought Statement - Issued 2nd November 2007*, Bureau of Meteorology, Australia [Australian government's report], Date of access: 18/04/2013; Available from: http://www.bom.gov.au/climate/drought/archive/20071102.shtml.

85. C.J. Meyer and D.A. Deglon, *Particle collision modeling – A review.* Minerals Engineering, 2011. **24**(8): p. 719-730.